Master thesis - Electrical Engineering

Characterization of Printed Transmission Lines at High Frequencies

Using quasi-analytical expressions

Sven van Berkel 4020480

Delft University of Technology

April 23, 2015

Master-track Telecommunications,
Faculty of Electrical Engineering,
Mathematics and Computer Science

Challenge the future

Characterization of Printed Transmission Lines at High Frequencies (April 23, 2015)

Preface

In this contribution, a quasi-analytical model is proposed allowing for fast characterization of a wide variety of printed transmission lines in terms of characteristic impedance, effective dielectric constant and losses. These losses are composed out of conductor losses, dielectric losses and radiation losses due to space and surface wave excitation. For printed transmission lines these latter losses are of particular importance when the transverse dimensions of the transmission lines become significant in terms of wavelength. The quasi-analytical model proposed in this thesis is implemented in a software tool, which is now rendered freely accessible, and capable of accurately analyzing the most widely used transmission lines. The software-tool can be downloaded at http://terahertz.tudelft.nl.

This thesis is submitted in partial fulfillment of the requirements for the degree of Master of Science in Electrical Engineering at Delft University of Technology.

Sven van Berkel
Delft, April 2015

Acknowledgments

First of all I would like to thank Prof. dr. Andrea Neto for giving me the opportunity for doing my master thesis at the Tera-Hertz Sensing Group. I am really looking forward working with you in the next couple of years.

Secondly, I express my sincere gratitude towards dr. Nuria Llombart, who patiently guided me on a daily basis. I couldn't wish for a better supervisor; your efforts in the past year in supervising me were inexhaustible.

Furthermore I thank all my colleagues of the Tera-Hertz Sensing Group for making this such a nice working place. Special thanks to Alessandro who gave me a head-start in the implementation of this quasi-analytical model in MATLAB and also to Daniele and Waqas, who never minded putting their own work aside to help me by giving me clear explanations on complex subjects.

I also would like to thank my dear friends from JC Kabel, providing me with some occasional distraction in the Lorre, so that I always had a healthy stash of Lorre-coins. Also you succeeded in making the last couple of years the best I've ever had. To that extent I also would like to thank my roommates and I apologize for practically living on the university last month.

Finally, I would like to dedicate this thesis to my parents who always supported me and gave me the opportunity to study.

Thanks to you all!

Characterization of Printed Transmission Lines at High Frequencies

Using quasi-analytical expressions

This thesis is submitted in partial fulfillment of the requirements for the degree of

MASTER OF SCIENCE

in

ELECTRICAL ENGINEERING

by

Sven van Berkel
born in Leiden, The Netherlands

The work presented in this thesis was performed at:

Tera-Hertz Sensing Group
Department of Microelectronics
Faculty of Electrical Engineering, Mathematics and Computer Science
Delft University of Technology

DELFT UNIVERSITY OF TECHNOLOGY
DEPARTMENT OF ELECTRICAL ENGINEERING

The undersigned hereby certify that they have read and recommend to the Faculty of Electrical Engineering, Mathematics and Computer Science for acceptance a thesis entitled **“ Characterization of Printed Transmission Lines at High Frequencies ”** by **Sven van Berkel** in partial fulfillment of the requirements for the degree of **Master of Science**.

Dated: May 1, 2015

Chairman: ______________________________

prof. dr. Andrea Neto

Advisor: ______________________________

dr. Nuria Llombart Juan

Committee Members: ______________________________

dr. Bert Kooij

____

dr. Marco Spirito

Contents

List of Figures

Chapter 1

Introduction

1.1 Background

Transmission lines are of a great importance in high frequency system design and is often one of the first components in the front-end of an antenna system. Poorly designed transmission lines will result in a loss of power and can cause high reflections in the system. A system designer would like to accurately predict the behavior of such transmission line. Printed Circuit Board (PCB) is commonly used for fabricating transmission lines thanks to its low-cost and easy fabrication. These transmission lines are referred to as printed transmission lines. However, transmission lines fabricated with current printed circuit board technologies are limited in its dimensions. Typical critical transverse dimensions are 100 μm in width and 127 μm in substrate height.

The main parameters of printed transmission lines, such as the propagation constant, attenuation constant and characteristic impedance, can generally be approximated resorting to two methods [1]. Firstly one could use full-wave simulations. These full-wave simulations are based on the Integral Equation method (e.g. Galerkin's method) [2–6], or Finite Difference (FD) [7] methods. These methods are generally very time-consuming and also require expensive licenses. Secondly, below 50 GHz, one can resort to quasi-static formulations [1, 8–10]. These formulations often make assumptions on the field distributions in the transmission line. For example the wave propagation of a microstrip configuration is sometimes assumed to be Transverse Electromagnetic; the characteristics of the configuration are then extracted from the electrostatic capacitance and inductance of the structure.

However, referring to the minimum feasible dimensions of the printed transmission lines, determined by the technology, the transverse dimensions of the transmission lines can become significant in terms of the wavelength ($\sim \lambda/20$ in line width and $\sim \lambda/4$ in substrate height) when the frequency increases ($f > 50GHz$). When the transverse dimensions become significant in terms of wavelength, dynamic phenomena in the line become non-negligible and can have a significant influence on the main parameters of the transmission line. Also, the excitation of leaky higher order modes causes radiation into space- and surface waves which launch power within the dielectric slabs [11, 12]. In fact, multiple modes can propagate simultaneously in the transmission line [13]. These phenomena could be avoided resorting to micro-metric integrated technology. However, one would like to still use low-cost printed circuit board technology while minimizing the effects of these higher order modes. For example, a coplanar wave guide (CPW), with a 100 μm minimum feasible dimension in width and spacing, will radiate while excited in its differential propagation mode at higher frequencies ($f \geq 50$ GHz). It is desired to study the significance of this radiation.

Quasi-static analysis does not suffice for predicting suchlike effects; one would like to know the dispersion characteristics of a transmission line rather than the capacitance, resistance or inductance as in quasi-static analysis. In fact, there are no (quasi-)analytical tools for estimating radiation losses into space- and surface-waves. Equivalent formulas exist for coplanar transmission line surface-wave losses [11, 14]. However, these formulas are not applicable for more complex structures dealing with multiple stratifications. Also the effect of the utilization of superconductive materials on the propagation constant and characteristic impedance cannot be easily estimated. A designer willing to carry out a detailed analysis of printed transmission lines will be obliged to resort to the use of full-wave simulations, which are very time-consuming. Accordingly, a fast quasi-analytical model is presented in this thesis in order to be able to characterize such structures, taking account of dynamic phenomena such as radiation or surface-wave excitation.

1.2 Solution proposed in this thesis

This work proposes a quasi-analytical software tool for characterizing printed transmission lines at high frequencies. The approach is called **quasi**-analytical, because the model performs numerical integrations and derivations. The quasi-analytical model makes use of the transmission line formalism [15]- [16]. The spectral Green's functions used in this formalism represent the solution to the integral equation of a magnetic or electric line current in the presence of stratified media. Therefore this formalism can then be used for a wide range of printed transmission lines having different number of conductors and dielectric stratifications such as a microstrip, stripline and a coplanar waveguide as in Figure 1.1. The model assumes that the transmission lines are infinitely long, the conductors infinitesimal in thickness and a homogeneity in the transverse plane. Making use of the Transmission Line Spectral Green's functions (TLGF), an integral equation can be constructed for both strip-type as slot-type structures from where the currents along the transmission line can be resolved. Analyzing the dominant current contribution, in its spectral form, will allow for a characterization in terms of propagation constant, characteristic impedance and losses associated to this specific mode. A study of the location of the propagating modes in the longitudinal spectral plane can give information regarding its nature; e.g. whether it is radiative or whether it is exciting a surface-wave. Accordingly, a suitable integration path in the transverse spectral plane needs to be chosen.

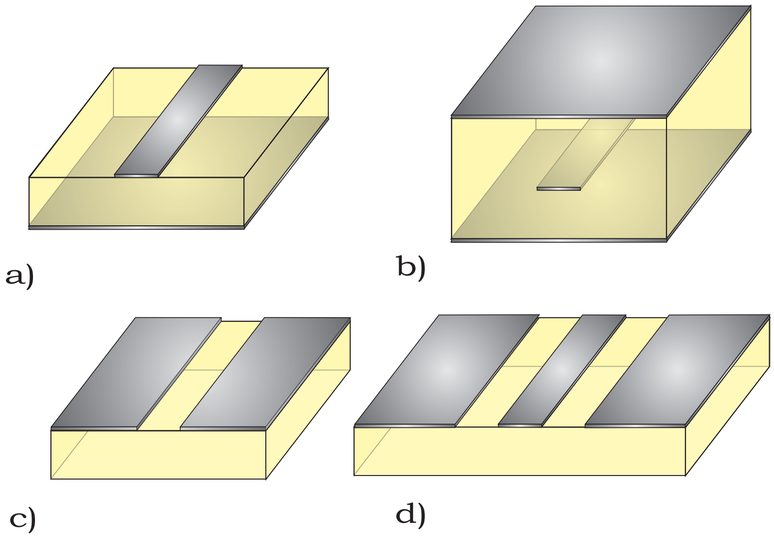

Figure 1.1: Examples of printed transmission lines. a) Microstrip, b) Stripline, c) Slotline, d) Coplanar Waveguide (CPW);

1.3 Outline of the thesis

The outline of this thesis is as follows. The thesis is divided in 3 main chapters. In chapter 2 we will cover some basic theory needed for characterizing printed transmission lines. The Transmission Line Spectral Green's function formalism is introduced from where we discuss the singularities that can be found in these Green's functions. These singularities are associated to space-waves, leaky-waves and surfaces-waves which are intrinsic to the stratification. In chapter 3, the quasi-analytical model used for transmission line characterization will be discussed. First the integral equations are formulated from where the dispersion equation is defined. Solving the dispersion equation will give us the propagating modes along the transmission lines and forms the basis of this quasi-analytical model. Next we will show that solving this dispersion is non-trivial as it depends on the integration path in the spectral domain; whether or not it encloses or crosses any singularities in the Green's functions. We will explain, by means of the current spectrum, how to do this integration in order to make sure that the propagating modes, found as a solution of the dispersion equation, are actually physically valid. Subsequently we will explain the procedure for calculating the characteristic impedance of the transmission line. Finally, the implementation of ohmic losses and superconductive materials in the quasi-analytical model are discussed. In chapter 4 will validate the proposed quasi-analytical model by several examples. In this chapter we will define a surface-wave loss approximation, stating that dielectric slabs with an electrical height larger than half a wavelength should be modeled as an infinite dielectric. This approximation will be the result of a comparison between the losses due to surface-wave excitation and direct radiation into an infinite medium.

Chapter 2

Spectral Green's functions

In this chapter, the two-dimensional (2D) spectral Green's functions are introduced. These Green's functions form a dyadic to calculate the electric or magnetic field due to an elementary source. The Green's functions follow from a transversalization of Maxwell's Equations. The total fields in layered media of printed transmission lines are decoupled in transverse electric- ($TE-$) and transverse magnetic- ($TM-$) waves. These waves are expressed in terms of voltages and currents in an equivalent transmission line representation of the stratification. Within the spectral Green's functions, singularities can be observed in the complex plane. The singularities of the Green's functions can represent space-waves, surface-waves and leaky-waves which are supported by the structure. Finally we will show that the field distributions in a structure with stratified media, excited by an elementary source, are mostly defined by the singularities found in the 2D transmission line Green's functions representing the stratified media.

2.1 Electric field due to an elementary source

Electromagnetic wave problems are conventionally solved by solving the Maxwell equations Eq. (2.1):

$$\begin{aligned}
\nabla \times \underline{\boldsymbol{e}} &= -\mu \frac{\partial \underline{\boldsymbol{h}}}{\partial t} - \underline{\boldsymbol{m}}_0 && (2.1)\\
\nabla \times \underline{\boldsymbol{h}} &= \varepsilon \frac{\partial \underline{\boldsymbol{e}}}{\partial t} + \underline{\boldsymbol{j}}_0 && (2.2)\\
\nabla \cdot \underline{\boldsymbol{e}} &= \frac{\rho}{\varepsilon} && (2.3)\\
\nabla \cdot \underline{\boldsymbol{h}} &= 0 && (2.4)
\end{aligned}$$

Solving the Maxwell equations essentially means that, given the known sources $\underline{\boldsymbol{m}}_0$ and $\underline{\boldsymbol{j}}_0$, the electric and magnetic fields are calculated for every point in space. However, solving the Maxwell equations can be non-trivial, especially for media with arbitrary stratifications. This problem can be avoided by using Green's functions. A Green's function $\underline{\tilde{\boldsymbol{g}}}(\underline{\boldsymbol{r}},\underline{\boldsymbol{r}}')$ forms the solution to the Maxwell equations; it is the electric ($\underline{\boldsymbol{e}}$) or magnetic ($\underline{\boldsymbol{h}}$) field, denoted by $\underline{\boldsymbol{f}}$, in $\underline{\boldsymbol{r}}$ radiated by an elementary equivalent current source $\delta(\underline{\boldsymbol{r}}-\underline{\boldsymbol{r}}')\hat{\boldsymbol{p}}$ located in $\underline{\boldsymbol{r}}'$. Therefore, Green's functions can be used as a dyadic to solve the Maxwell equations for arbitrary current sources by means of a convolution integral between the Green's function and the impressed currents:

$$\underline{\boldsymbol{f}}(\underline{\boldsymbol{r}},\underline{\boldsymbol{r}}') = \iiint_V \underline{\underline{\tilde{\boldsymbol{g}}}}(\underline{\boldsymbol{r}},\underline{\boldsymbol{r}}') * \underline{\boldsymbol{c}}(\underline{\boldsymbol{r}}')d\underline{\boldsymbol{r}}' \qquad (2.5)$$

where $\underline{\boldsymbol{f}}(\underline{\boldsymbol{r}},\underline{\boldsymbol{r}}')$ is the electric ($\underline{\boldsymbol{e}}$) or magnetic ($\underline{\boldsymbol{h}}$) field due to an electric ($\underline{\boldsymbol{j}}_0$) or magnetic ($\underline{\boldsymbol{m}}_0$) current source $\underline{\boldsymbol{c}}(\underline{\boldsymbol{r}}')$. The Green's functions for an elementary dipole in free-space can be analytically derived from electric and magnetic vector potentials. For printed transmission lines we are, of course, not interested in free-space solutions since the strips (or slots) are printed on dielectrics such as silicon. Expressing the Green's functions in its spectral form with respect to its transverse components is required; this will allow for solving more complex problems using an equivalent transmission line representation.

2.2 Spectral Green's functions

Translating the Green's functions to the spectral domain allows us for using an equivalent transmission line representation on the arbitrary stratification of plane-stratified media [17]. Subsequently we will show that the singularities in the Transmission Line Spectral Green's functions (TLGF) are the dominant points contributing to the fields $\underline{\boldsymbol{f}}(\underline{\boldsymbol{r}},\underline{\boldsymbol{r}}')$. The Fourier transform of the spatial Green's functions $\underline{\underline{\tilde{\boldsymbol{g}}}}(\underline{\boldsymbol{r}},\underline{\boldsymbol{r}}')$ is defined as Eq. (2.6).

$$\underline{\underline{\tilde{\boldsymbol{g}}}}(\underline{\boldsymbol{r}},\underline{\boldsymbol{r}}') \xrightarrow{\mathcal{F}} \underline{\underline{\tilde{\boldsymbol{G}}}}(k_x,k_y,z,z') = \int_{-\infty}^{\infty}\int_{-\infty}^{\infty} \underline{\underline{\tilde{\boldsymbol{g}}}}(\underline{\boldsymbol{r}},\underline{\boldsymbol{r}}')e^{jk_xx}e^{jk_yy}dxdy \tag{2.6}$$

After representing the Green's function and current sources in the spectral domain, the convolution from Eq. (2.5) can then be expressed as a multiplication in the spectral domain. The fields $\underline{\boldsymbol{f}}(\underline{\boldsymbol{r}},\underline{\boldsymbol{r}}')$ can then be expressed as an inverse Fourier transform of this spectral multiplication as is shown in Eq. (2.7).

$$\underline{\boldsymbol{f}}(\underline{\boldsymbol{r}},\underline{\boldsymbol{r}}') = \left(\frac{1}{2\pi}\right)^2 \int_{-\infty}^{\infty}\int_{-\infty}^{\infty} \underline{\underline{\tilde{\boldsymbol{G}}}}(k_x,k_y,z,z')\cdot\underline{\boldsymbol{C}}(k_x,k_y)e^{-jk_xx}e^{-jk_yy}dk_xdk_y \tag{2.7}$$

where

$$\underline{\boldsymbol{c}}(\underline{\boldsymbol{r}}') \xrightarrow{\mathcal{F}} \underline{\boldsymbol{C}}(k_x,k_y) \tag{2.8}$$

Having the Green's functions in its spectral form, analytic solutions can be derived for plane-stratified media problems as such we will be dealing with printed transmission lines.

2.2.1 Spectral transmission line representation of stratified media

When printed transmission lines are assumed to be homogeneous in the $(\hat{\boldsymbol{x}},\hat{\boldsymbol{y}})$-plane, the transmission line can be modeled as plane stratified media. It is well known how to construct the spectral Green's functions of such plane stratified media [17]. In the software-tool, four possible stratifications are considered:

1. An infinite top medium
2. A finite upper slab
3. A finite lower slab
4. An infinite bottom medium

With this choice of stratification, most commonly used printed transmission lines can be modeled. Visualizing these stratifications congruent to the equivalent transmission line representation gives us Figure 2.1. Both top and bottom media are infinite, the equivalent transmission lines of these media can therefore be characterized as loads, Z_{L-top} and $Z_{L-bottom}$, connected to the finite transmission lines representing the upper and lower slabs with characteristic

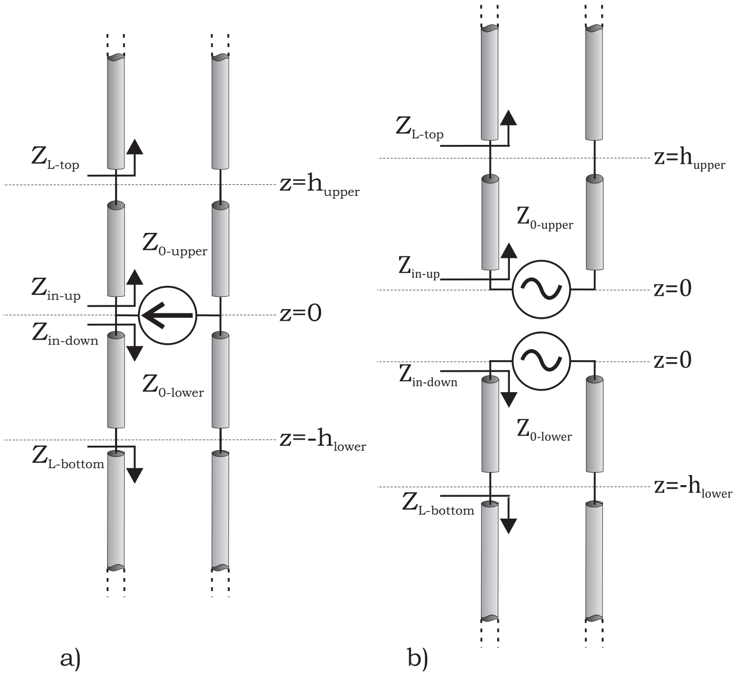

Figure 2.1: General equivalent transmission line models for a) strip-type transmission lines and b) slot-type transmission lines.

impedances $Z_{0-upper}$ and $Z_{0-lower}$. The transmission-line model is entirely decoupled in TM- and TE-modes, where the loads, Z_L, and characteristic impedances Z_0 can be characterized by (2.9).

$$Z^{TM} = \zeta\frac{k}{k_z} \tag{2.9)a}$$

$$Z^{TE} = \zeta\frac{k_z}{k} \tag{2.9)b}$$

where ζ is the wave-impedance $\zeta_0/\sqrt{\varepsilon_r}$. The current- and voltage- sources in Figure 2.1 are normalized to 1 A and 1 V respectively. Therefore, by using the input impedances for the upper (Z_{in-up}) and lower ($Z_{in-down}$) half of the structure, the TLGF can be expressed in terms of the voltage $v_{TM/TE}$ or the current $i_{TM/TE}$ at $z = 0$ for an electric- or magnetic source at $z' = 0$ respectively according to (2.10) [18].

$$\tilde{G}^{EJ}_{xx}(k_x,k_y) = -\frac{v^J_{TM}k_x^2 + v^J_{TE}k_y^2}{k_\rho^2} \tag{2.10)a}$$

$$\tilde{G}^{HM}_{xx}(k_x,k_y) = -\frac{i^M_{TE}k_x^2 + i^M_{TM}k_y^2}{k_\rho^2} \tag{2.10)b}$$

where $k_\rho^2 = k_x^2 + k_y^2$. As will be shown at the construction of the integral equations in chapter 3, only the xx-component of the dyadic Green's functions are necessary for the characterization of printed transmission lines. For a magnetic source, in Figure 2.1b, the upper and lower half-space are entirely separated by a ground-plane, leading to a summation of two independent Green's functions as in Eq. (2.11).

$$\tilde{G}^{HM-tot}_{xx}(k_x,k_y) = \tilde{G}^{HM-up}_{xx}(k_x,k_y) + \tilde{G}^{HM-down}_{xx}(k_x,k_y) \tag{2.11}$$

The used formalism for the Green's function will allow for easy implementation and analysis of some interesting characteristics of printed transmission lines; such as radiation into space- and surface-waves, dielectric losses, conductor losses in any ground planes and superconductivity. This will be discussed later on. A more extensive explanation and derivation of the spectral Green's functions which are used for the printed transmission lines in the software-tool can be found in Appendix C.

2.2.2 Singularities

In the previous subsection we arrived at an expression of the electric- or magnetic fields due to an elementary current source formulated in terms of anti-Fourier transforms (2.7). The Fourier transform of the current source, $\underline{C}(k_x,k_y)$, does not contain any singularities. Therefore, the field distribution is dominated by the contributions due to the singularities in the Green's functions (2.10). These singularities can be poles, associated to intrinsic leaky- or surface-waves modes or branch-points and -cuts associated to any infinite media. We will investigate the singularities in the Green's function due to an electric source oriented along $\hat{\boldsymbol{x}}$, i.e. the singularities in $\tilde{G}^{EJ}_{xx}(k_x,k_y)$ in Eq. (2.10)a. The procedure will be similar for the Green's functions due to a magnetic source and will not be performed here.

Performing a change to a polar coordinate system, without showing the algebraic steps, for the integral Eq. (2.7) and the Green's functions Eq. (2.10) we obtain Eq. (2.12) and Eq. (2.13) [19]. In this change of coordinate system we used $k_x = k_\rho \cos(\alpha)$ and $k_y = k_\rho \sin(\alpha)$.

$$\underline{f} = \left(\frac{1}{2\pi}\right)^2 \int_0^{2\pi} \int_{-\infty}^{\infty} \underline{\underline{\tilde{G}}}(k_\rho,\alpha,z,z') \cdot \underline{C}(k_\rho,\alpha) e^{-j\underline{k}_\rho \cdot \underline{\rho}} k_\rho dk_\rho d\alpha \tag{2.12}$$

$$\tilde{G}^{EJ}_{xx}(k_\rho,\alpha) = -v^J_{TM}(k_\rho)\cos^2(\alpha) - V^J_{TE}(k_\rho)\sin^2(\alpha) \qquad (2.13)\text{a}$$

$$\tilde{G}^{HM}_{xx}(k_\rho,\alpha) = -i^M_{TE}(k_\rho)\cos^2(\alpha) - V^M_{TM}(k_\rho)\sin^2(\alpha) \qquad (2.13)\text{b}$$

It can be demonstrated that $\underline{f}$ does not depend on α since the integral in α (2.12) can be closed assuming a far observation distance and a asymptotic evaluation of the slow-varying contributions of the integrand [19]. As is explained, the current source in Figure 2.1a is normalized to 1 A. Therefore, $v_{TM/TE}$ at $z = 0$ can be expressed in terms of the input impedances for the upper (Z_{in-up}) and lower ($Z_{in-down}$) half of the structure as is described in Eq. (2.14).

$$v_{TM/TE} = \frac{Z_{in-up}Z_{in-down}}{Z_{in-up}+Z_{in-down}} \tag{2.14}$$

From Eq. (2.14) it is clear that both the TM- and TE-waves supported by the structure can be found by solving Eq. (2.15)

$$Z_{in-up}+Z_{in-down} = 0 \tag{2.15}$$

Solving the equality in Eq. (2.15), results in a location of the singularity k_ρ in the spectrum. Evaluating the integral (2.12) in k_ρ by calculating the residues as is described in Appendix A of [19], the electric field contributions due to a TM-wave were calculated as being (2.16) while the electric field contribution due to a TE-wave can be expressed as (2.17).

$$E_\rho(\rho,z) \approx \mathrm{Res}[v_{TM}(k_\rho,z,z')]C_x(k_\rho,\phi)\frac{C\cos(\phi)\,e^{-jk_\rho\rho}}{\sqrt{\rho}} \tag{2.16)a}$$

$$E_z(\rho,z) \approx -\frac{\zeta k_\rho}{k}\mathrm{Res}[i_{TM}(k_\rho,z,z')]C_x(k_\rho,\phi)\frac{C\cos(\phi)\,e^{-jk_\rho\rho}}{\sqrt{\rho}} \tag{2.16)b}$$

$$E_\phi(\rho,z) \approx -\mathrm{Res}[v_{TE}(k_\rho,z,z')]C_x(k_\rho,\phi)\frac{C\sin(\phi)\,e^{-jk_\rho\rho}}{\sqrt{\rho}} \tag{2.17}$$

where, $C_x(k_\rho,\phi)$ is assumed to be a PWS current distribution (2.18). In (2.18), l and w_s are the length and width of the PWS current respectively and k_{eq} is the effective propagation constant of the current.

$$C_x(k_\rho,\phi) = \frac{2k_{eq}\left(\cos\left(\frac{k_x l}{2}\right) - \cos\left(\frac{k_{eq} l}{2}\right)\right)}{(k_{eq}^2 - k_x^2)\sin\left(\frac{k_{eq} l}{2}\right)}\mathrm{sinc}\left(\frac{k_y w_s}{2}\right) \tag{2.18}$$

C is resulting from an asymptotic behavior evaluation for large observation distances (2.19)

$$C = j\sqrt{\frac{k_\rho}{2\pi}}e^{j\frac{\pi}{4}} \tag{2.19}$$

Similar steps can be done for a magnetic current source. The electric field components can then be summarized in an informative figure as in Figure 2.2 and 2.3. We can see the orientation and field components of the TM- and TE-surface-waves for a magnetic or electric current respectively. TM-surface-wave will only have an electric field in the radial- and z-direction while the TE-surface-wave will only have an electric field component in the azimuthal direction. Also the $\cos(\phi)$ distribution from Eq. (2.16) and Eq. (2.17) can be seen. From the $1/\sqrt{\rho}$-spreading of the fields it is clear that we are dealing with cylindrical waves.

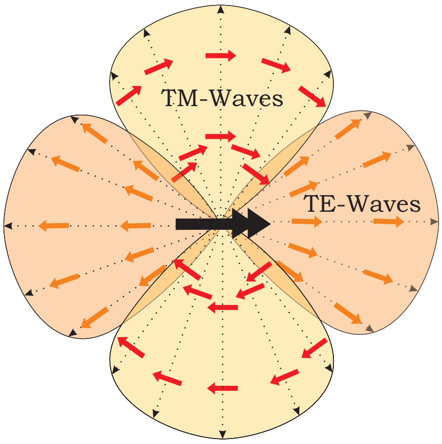

Figure 2.2: TM- and TE- surface-wave propagation direction and field components for a magnetic current (slot-type transmission line)

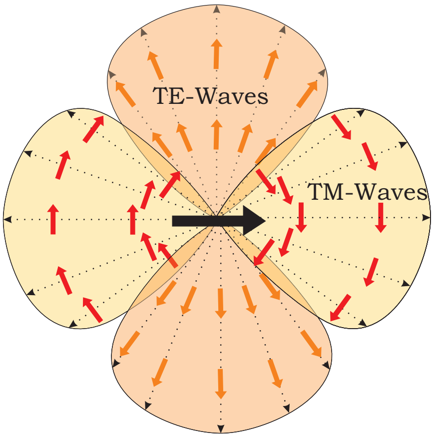

Figure 2.3: TM- and TE- surface-wave propagation direction and field components for an electric current (strip-type transmission line)

2.3 Surface-and leaky-waves

In this section, the field components resulting from the singularities found from the Green's functions will be investigated. In the case that k_ρ is completely real (for lossless stratification), the pole represents a surface-wave. When k_ρ will have an imaginary part, the wave will leak power into an infinite medium and therefore represents a leaky-wave. In this section we will explain some basic characteristics regarding surface- and leaky-waves.

Two situations will be studied:

1. A surface-wave pole due to an electric current source in the presence of a grounded dielectric slab
2. A leaky-wave pole due to an electric current source in a grounded air-gap, but in the presence of a high dense infinite medium

In both situations, a CST simulation will be performed where the propagation direction and field components of the wave, as visualized in Figure 2.3, will be verified.

2.3.1 Surface-waves due to an elementary source

In this subsection, we will start with a concise description of the characteristics of a surface-wave after which the surface-waves in a grounded dielectric slab excited by an elementary source is investigated. In this investigation, the field components of the first TM-surface-wave will be verified by evaluating the integral (2.7) by means of the residual contributions from Eq. (2.16).

Surface-wave characteristics

Any dielectric slab with non-zero thickness and a relative permittivity greater than unity supports at least one propagating surface-wave mode without a cut-off frequency [20]. Surface-waves can be described as waves propagating in the transverse direction without attenuation; the waves are guided inside the stratifications of the structure. Because the surface-waves travel without attenuation, the transverse propagation constant, $k_{\rho,SFW}$, will be strictly real (2.20). Note that we are assuming a lossless dielectric slab, in the case of dielectric losses $k_{\rho,SFW}$ will have an imaginary part.

$$k_{\rho,SFW} = \beta_{\rho,SFW} \tag{2.20}$$

Since the surface-waves are bound and do not leak, we can consider the wave as a couple of plane waves bouncing within the stratification with an angle, θ_{SFW}, greater than the critical angle, $\theta_c = \sin^{-1}\left(\frac{1}{\sqrt{\varepsilon_r}}\right)$, where ε_r is the relative permittivity of the dielectric. This is shown in

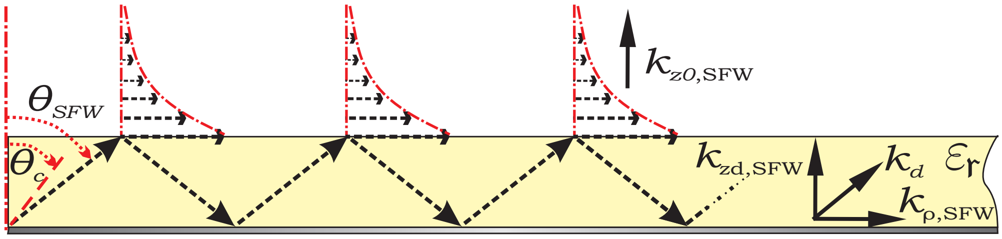

Figure 2.4: Surface-wave propagation mechanism in a dielectric slab with an infinite medium of air.

Figure 2.4. Because $\theta_{SFW} > \theta_c$, the angle of transmission, θ_t will be imaginary; there will be no transmitted propagating wave. With this information and referring to Snell's law (2.21),

$$\begin{aligned} \sqrt{\varepsilon_r}\sin(\theta_{SFW}) &= \sin(\theta_t) \\ \sqrt{\varepsilon_{r,SFW}} &= \sin(\theta_t) > 1 \end{aligned} \tag{2.21}$$

we can deduct that the propagation constant will be between k_0 and k_d, where $k_d = k_0\sqrt{\varepsilon_r}$. Surface-waves are referred to as slow-waves because $k_{\rho,SFW} > k_0$ and therefore $v_{SFW} < v_0$.

In Figure 2.4, electric field lines are drawn outside the dielectric slab. However there is no propagation in $\hat{z}$-direction outgoing from the dielectric slab; the propagation constant $k_{z0,SFW}$ outside the slab is purely imaginary and verifying the radiation condition Eq. (2.22).

$$k_{z0,SFW} = \sqrt{k_0^2 - k_{\rho,SFW}^2} = -j\alpha_{z0,SFW} \tag{2.22}$$

Whether a surface-wave is excited in a printed transmission line and what conditions are related to this excitation will be discussed in chapter 3. Now we will verify the field distributions associated to a surface-wave.

Electric current-source in the presence of a grounded dielectric slab

The stratification under investigation is shown in Figure 2.5 with $H = 500\mu$m and $\varepsilon_r = 11.9$. The structure is excited with an elementary electric source oriented along $\hat{x}$ with dimensions $\Delta_x = \Delta_y = \lambda_f/20$, where λ_f is the free-space wavelength at 85 GHz. The first two surface-waves appearing in this structure are the TM_0-surface-wave with a cutoff frequency of $k_c = 0$ and the TE_1-surface-wave with a cutoff frequency of $k_c = \frac{\pi}{2H}$. Note that these surface-waves are singularities in the Green's functions as is explained in subsection 2.2.2. These two surface-waves are of interest when applying a frequency sweep of

$$25\text{ GHz} < f < 85\text{ GHz}$$

resulting in an electrical height of the slab of

$$0.14\lambda_d < H < 0.49\lambda_d$$

where λ_d is the wavelength inside the dielectric. The TM_0- and TE_1-surface-waves are shown in Figure 2.6.

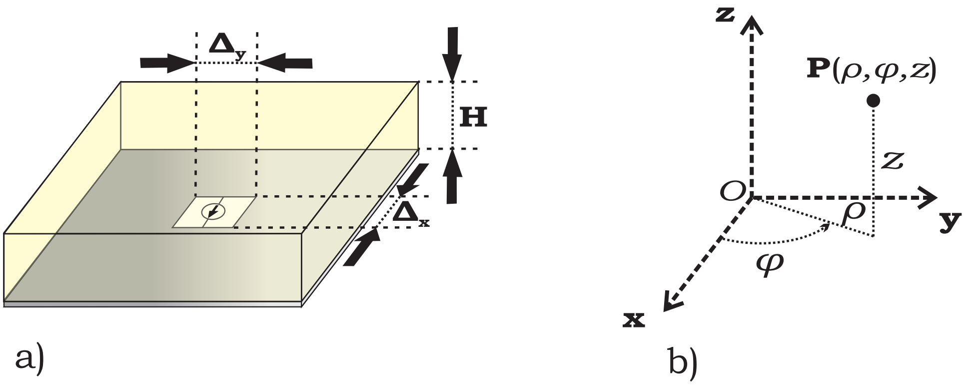

Figure 2.5: a) Grounded dielectric slab with $H = 500\mu$m, $\varepsilon_r = 11.9$, $\Delta_x = \Delta_y = \lambda_f/20$, where λ_f is the wavelength at 85 GHz. b) Cartesian and cylindrical reference system.

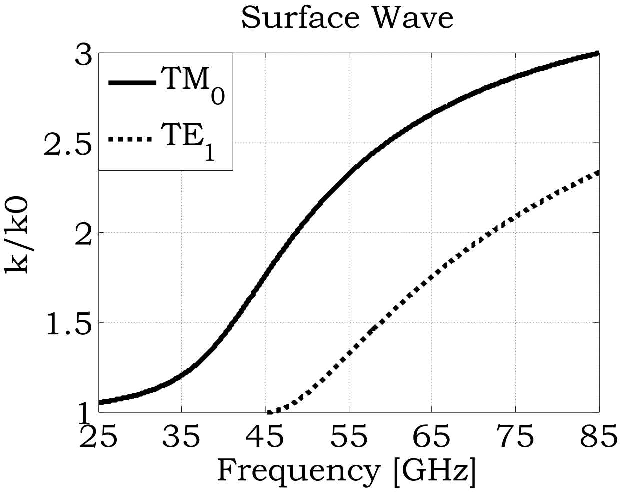

Figure 2.6: TM_0- and TE_1-surface-waves for the structure in Figure 2.5a.

According to Eq. (2.16), the TM_0-surface-wave will have an electric field in radial- and z-direction while the TE_1-surface-wave will have an electric field in the azimuthal direction. In Figure 2.7a we can see the (x,y)-plane of $|E_{tot}| = \sqrt{|E_\rho|^2 + |E_z|^2 + |E_\phi|^2}$ at 45 GHz inside the dielectric slab, extracted from a CST simulation. From the distinct $\cos(\phi)/\sqrt{\rho}$ distribution of the electric field and referring to Figure 2.3, it is clear that indeed only the TM_0-surface-wave is present in the stratification. Looking at the (x,y)-plane at 45 GHz, we can see an electric field outside the dielectric slab, in the air. However, as is explained, this is not a propagating wave in the air as the surface-wave angle is above the critical angle. In Figure 2.6 we see that at 80 GHz both the TM_0- as the TE_1-surface-wave are above cut-off frequency. This is confirmed when looking at the (x,z)-plane of $|E_{tot}|$ in Figure 2.7c, where the $\cos(\phi)/\sqrt{\rho}$ distribution has disappeared; interference can be seen between both surface-wave as they are propagating with different phase-velocities (see Figure 2.6).

We will go more in depth in the electric field distribution of a surface-wave in a grounded slab. The electric field distribution will be analyzed at 45 GHz, allowing to see only the TM_0-surface-wave. The total electric field as a function of height at $f = 45$ GHz and $\phi = 0$ is shown in Figure 2.8. ρ is chosen to be a few wavelengths from the source, eliminating any near-field contributions excited by the elementary current source. We can see that $|E_z|$ has a discontinuity at the interface between the slab and air ($z = 500\mu$m) while $|E_\rho|$ is continuous. This behavior verifies the boundary conditions between two dielectric media (2.23), where a discontinuity of the normal electric field is proportional to the ratio of the dielectric constants, $\varepsilon_2/\varepsilon_1$ $(= 1/\varepsilon_r)$:

$$\begin{aligned} \hat{z}_{12} \times (\underline{e}_2 - \underline{e}_1) &= 0 && \text{(2.23)a} \\ (\varepsilon_2 \underline{e}_2 - \varepsilon_1 \underline{e}_1) \cdot \hat{z}_{12} &= 0 && \text{(2.23)b} \end{aligned}$$

The fields calculated by CST can be verified by evaluating the integral Eq. (2.7) in terms of the residual field contributions from the poles found in the Green's functions (2.16) [19]. In (2.16), the residues are required to be calculated for v_{TM} and i_{TM} in the surface-wave poles $k_\rho = k_{TM_0}$. For this structure the residues for the fields inside the slab ($z < H$) are (2.24):

$$\mathrm{Res}[v_{TM}(k_\rho, z)]|_{k_\rho = k_{TM_0}} = \frac{Z_0 Z_s}{D'(k_\rho)} \frac{\sin(k_{zd,SFW} z)}{\sin(k_{zd,SFW} H)} \qquad \text{(2.24)a}$$

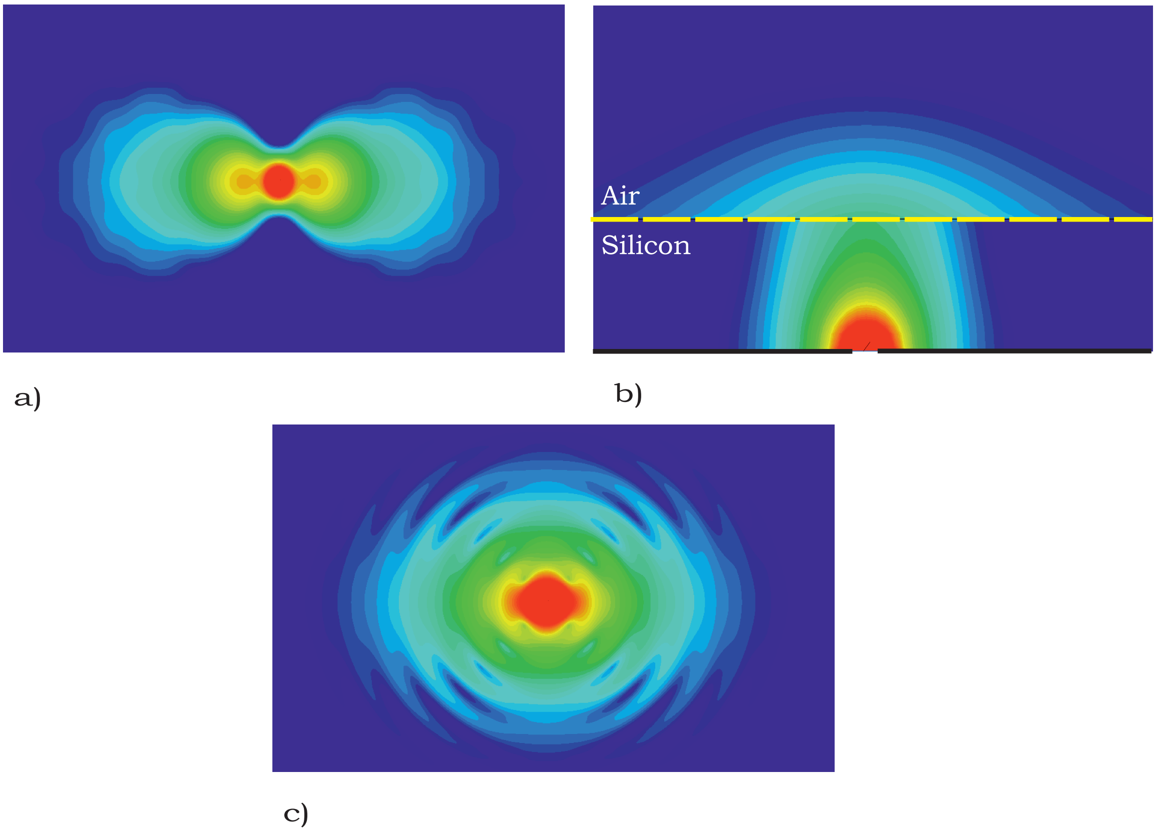

Figure 2.7: 2D-plane view of $|E_{tot}|$ for the structure in Figure 2.5a, extracted from CST MWS; a) (x,y)-plane inside the dielectric slab at 45 GHz, b) (x,z)-plane at 45 GHz and c) (x,y)-plane inside the dielectric slab at 80 GHz.

$$\mathrm{Res}[i_{TM}(k_\rho,z)]|_{k_\rho=k_{TM_0}} = \frac{Z_0 Z_s}{D'(k_\rho)}\frac{1}{Z_d}\frac{j\cos\left(k_{zd,SFW}z\right)}{\sin\left(k_{zd,SFW}H\right)} \tag{2.24)b}$$

And the residues for the fields inside the air $(z > H)$ are (2.25):

$$\begin{aligned}
\mathrm{Res}[v_{TM}(k_\rho,z)]|_{k_\rho=k_{TM_0}} &= \frac{Z_0 Z_s}{D'(k_\rho)} e^{jk_{z0,SFW}H} e^{-jk_{z0,SFW}z} && \text{(2.25)a}\\
\mathrm{Res}[i_{TM}(k_\rho,z)]|_{k_\rho=k_{TM_0}} &= \frac{Z_0 Z_s}{D'(k_\rho)}\frac{1}{Z_0} e^{jk_{z0,SFW}H} e^{-jk_{z0,SFW}z} && \text{(2.25)b}
\end{aligned}$$

In Eq. (2.24) and Eq. (2.25) we have

$$\begin{aligned}
k_{z0,SFW} &= -j\sqrt{-(k_0^2-k_\rho^2)} && \text{(2.26)a}\\
k_{zd,SFW} &= \sqrt{k_d^2-k_\rho^2} && \text{(2.26)b}\\
Z_0 &= \zeta_0\frac{k_{z0,SFW}}{k_0} && \text{(2.26)c}\\
Z_d &= \zeta_0\frac{k_{zd,SFW}}{k_d} && \text{(2.26)d}\\
Z_s &= jZ_d\tan\left(k_{zd,SFW}H\right) && \text{(2.26)e}\\
D(k_\rho) &= Z_0(k_\rho)+Z_s(k_\rho) && \text{(2.26)f}
\end{aligned}$$

Using this approach, the electric fields of the TM_0-surface-wave in Figure 2.8 can be verified and this is shown in Figure 2.9 and Figure 2.10 for the electric field in the dielectric slab and

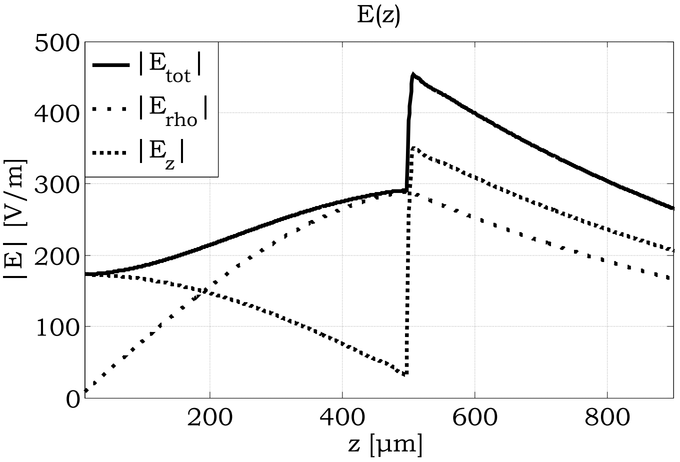

Figure 2.8: Total electric field as a function of height at $f = 45$ GHz and $\phi = 0$

air respectively. The fields obtained by calculating the residues are normalized to the amplitude of the electric fields from CST. We can see that, indeed, the singularity found from the Green's functions (k_{TM_0} in Figure 2.6) is responsible for the total electric field distribution. Also, the $\sin(k_{zd,SFW}z)$ and $\cos(k_{zd,SFW}z)$ distribution in the dielectric from Eq. (2.24) can be recognized in the field-distributions of $|E_\rho|$ and $|E_z|$ respectively. Finally, the exponential decaying, non propagating wave, in the air can be recognized; from the residues in Eq. (2.25) and Eq. (2.22) we have $e^{-jk_{z0,SFW}z} = e^{-\alpha_{z0,SFW}z}$.

With this we will conclude our concise description of surface-wave poles found in the Green's functions and the characterization of the fields associated to them. In chapter 3 we will investigate when such surface-wave is excited on a printed transmission line and in chapter 4 some examples will be given together with a surface-wave loss study.

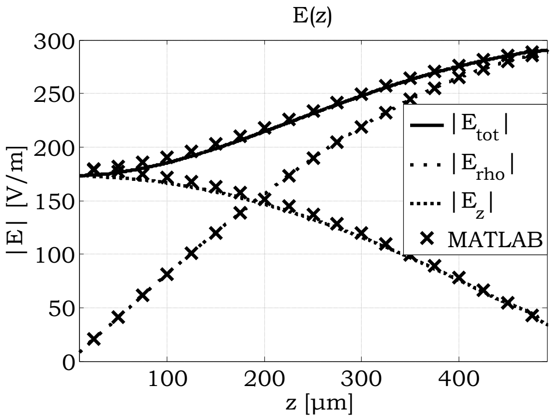

Figure 2.9: Total electric field in the dielectric slab as a function of height at $f = 45$ GHz and $\phi = 0$ verified with the Residue Theorem

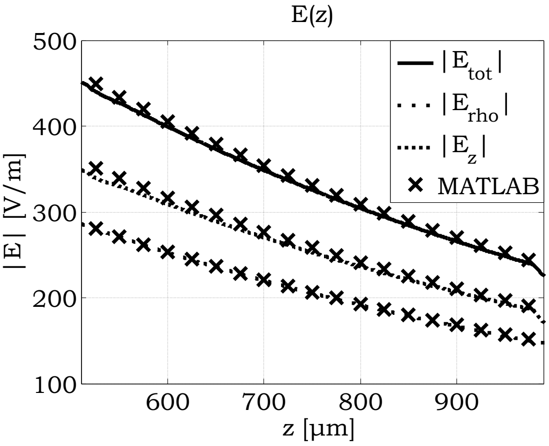

Figure 2.10: Total electric field in the air as a function of height at $f = 45$ GHz and $\phi = 0$ verified with the Residue Theorem

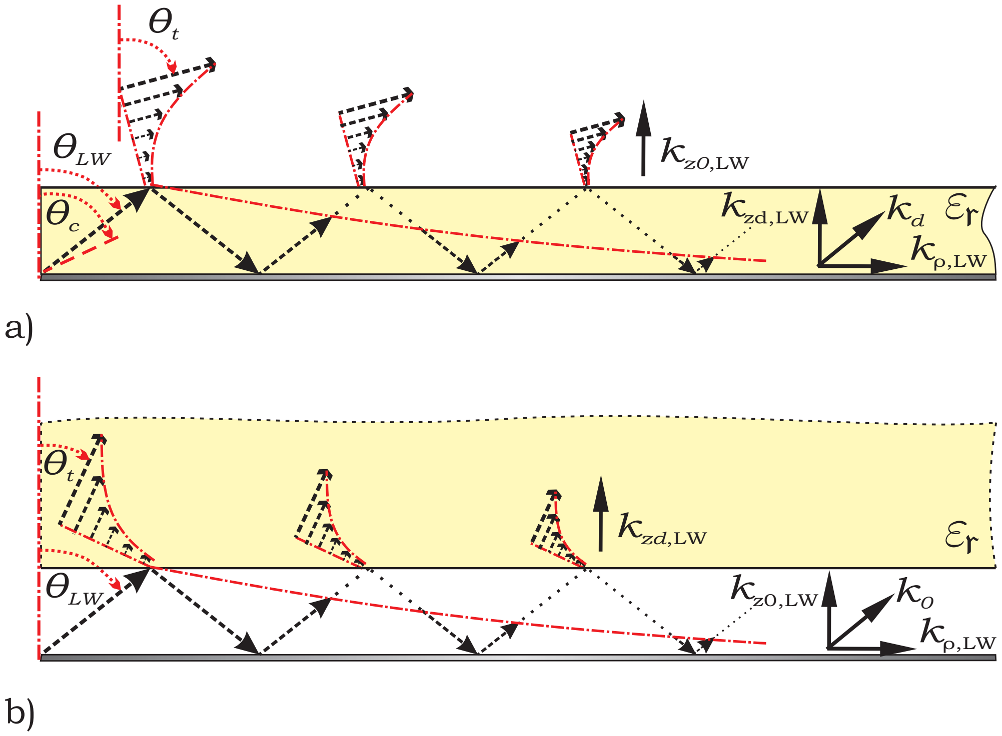

Figure 2.11: Leaky-wave propagation mechanism in a) a dielectric slab with an infinite medium of air b) a grounded air-gap in the presence of an infinite medium.

2.3.2 Leaky-waves due to an elementary source

In this subsection, we will start with a concise description of the characteristics of a leaky-wave after which the leaky-waves in a grounded air-gap, but in the presence of an infinite dielectric, excited by an elementary source is investigated. In this investigation, the field components of the first TM-surface-wave will be verified by evaluating the integral (2.7) by means of Eq. (2.16).

Leaky-wave characteristics

Leaky-waves can be described as waves propagating in the transverse direction, but in contrast to surface-waves, they propagate with attenuation; the waves are leaking into the infinite medium. Because the leaky-waves travel with attenuation, the transverse propagation constant, $k_{\rho,LW}$, will have an imaginary part (2.27).

$$k_{\rho,LW} = \beta_{\rho,LW} - j\alpha_{\rho,LW} \tag{2.27}$$

In Figure 2.11 we see two structures where a leaky-wave can exist. In a) we see a dielectric slab with an infinite medium of air while in b) we can see a grounded air-gap in the presence of an infinite medium. In Figure 2.11a, θ_{LW} is now smaller than the critical angle, $\theta_c = \sin^{-1}\left(\frac{1}{\sqrt{\varepsilon_r}}\right)$ whereas the structure in Figure 2.11b does not have a critical angle since $\theta_c = \sin^{-1}(\sqrt{\varepsilon_r})$ is completely imaginary. For the leaky-waves with a propagating mechanism as in Figure 2.11, we know that the angle of transmission θ_t is now real so that for subfigure a), Snell's law gives us:

$$\begin{aligned} \sqrt{\varepsilon_r}\sin(\theta_{LW}) &= \sin(\theta_t) \\ \sqrt{\varepsilon_{r,LW}} &= \sin(\theta_t) < 1 \end{aligned} \tag{2.28}$$

And for subfigure *b*), we know θ_{LW} is real so that Snell's law gives us:

$$\begin{aligned} \sin(\theta_{LW}) &= \sqrt{\varepsilon_r}\sin(\theta_t) \\ \sqrt{\varepsilon_{r,LW}} &< 1 \end{aligned} \tag{2.29}$$

The effective dielectric constant of the leaky-wave, $\varepsilon_{r,LW}$, will therefore be smaller than 1 (2.28). So in contrary to surface-waves, leaky-waves are referred to as fast-waves since $k_{\rho,LW} < k_0$ (2.30) and therefore $v_{LW} > v_0$.

$$k_{\rho,LW} = k_0\sqrt{\varepsilon_{r,SFW}} < k_0 \tag{2.30}$$

In Figure 2.11, the electric field lines are drawn outside the dielectric slab. In contrary to the surface-wave situation θ_t will be real; there will be propagation outside the dielectric slab with a propagation constant of Eq. (2.31).

$$k_{z,LW} = \sqrt{k_0^2 - k_{\rho,LW}^2} = \beta_{z,LW} + j\alpha_{z,LW} \tag{2.31}$$

The imaginary part of the wavenumber is positive; the fields are growing with z. The propagation constant is therefore not verifying the radiation condition. However, the pole is still physically valid because $Im[k_{\rho,LW}] < 0$. The exponential attenuation in ρ, $e^{-\alpha_{\rho,LW}\rho}$, is in fact larger than the growing in z, $e^{+\alpha_{z,LW}z}$.

Apart from the leaky-waves in Figure 2.11b with $k_{\rho,LW} < k_0$, another leaky-wave pole can be identified in the Green's function with $k_{\rho,LW} > k_0$. An example of such pole can be seen in Figure 2.13 which will be further investigated in the following subsection. This leaky-wave mode is not bouncing within the stratification (since $k_{\rho,LW} > k_0$), but propagating along the interface and directly radiating into the infinite dielectric.

Electric current-source in a grounded air-gap but the presence of a dielectric slab

The stratification under investigation is shown in Figure 2.12 with $H = 500\mu$m and $\varepsilon_r = 11.9$ for the infinite dielectric. The structure is excited with an elementary electric source with dimensions $\Delta_x = \Delta_y = \lambda_f/20$, where λ_f is the free-space wavelength at 85 GHz. The first leaky-wave appearing in this structure is a TM-leaky-wave. This leaky-wave is the only one of interest when applying a frequency sweep of

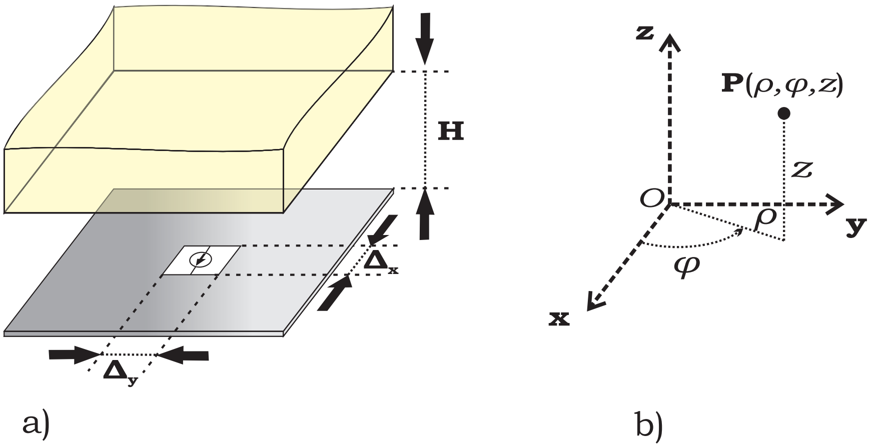

Figure 2.12: a) Grounded air-gap with $H = 500\mu$m below an infinite dielectric, $\varepsilon_r = 11.9$, $\Delta_x = \Delta_y = \lambda_f/20$, where λ_f is the wavelength at 85 GHz. b) Cartesian and cylindrical reference system.

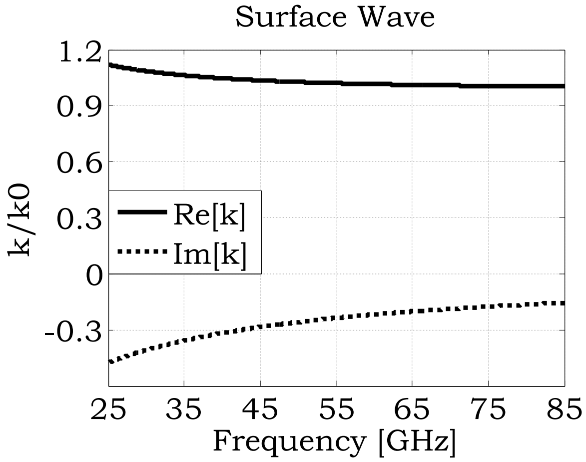

Figure 2.13: TM_0- surface-wave for the structure in Figure 2.12

$$25 \text{ GHz} < f < 85 \text{ GHz}$$

resulting in an electrical height of the air-gap of

$$0.042\lambda_0 < H < 0.14\lambda_0$$

where λ_0 is the wavelength inside the air-gap. The TM-leaky-wave for this frequency sweep is shown in Figure 2.13.

Equivalent to the TM_0-surface-wave in the previous subsection, the TM-leaky-wave will have an electric field in radial- and z-direction. In Figure 2.14a we can see the (x,y)-plane of $|E_{tot}| = \sqrt{|E_\rho|^2 + |E_z|^2 + |E_\phi|^2}$ at 45 GHz inside the dielectric slab, extracted from a CST simulation. Once again, the distinct $\cos(\phi)/\sqrt{\rho}$ distribution of the electric field can be seen, verifying that indeed only the TM-leaky-wave is present in the stratification. Looking at the (x,z)-plane at 45 GHz, we can now see clearly a propagating wave outside the air-gap, into the infinite medium; the leaky-wave is indeed leaking.

We will go more in depth in the electric field distribution of this leaky-wave and try to verify it analytically. The total electric field as a function of height at $f = 45$ GHz and $\phi = 0$ is shown

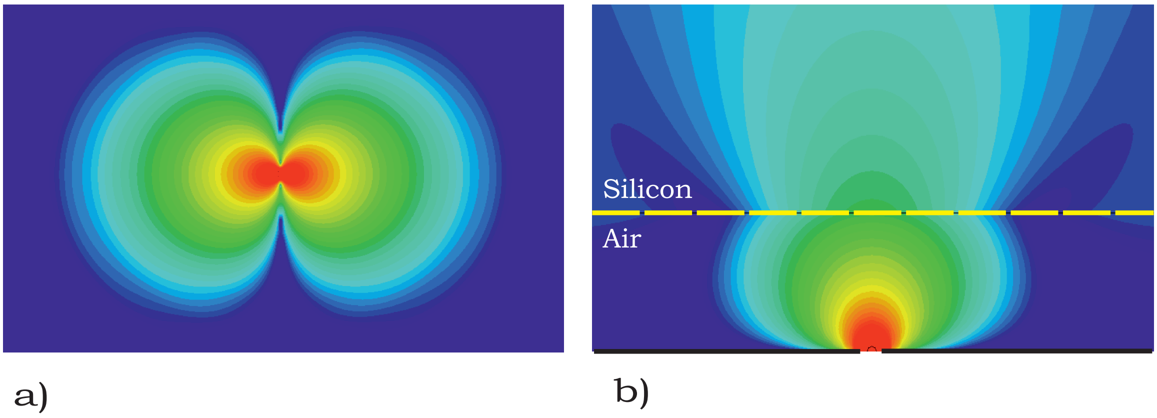

Figure 2.14: 2D-plane view of $|E_{tot}|$, extracted from CST MWS at 45 GHz for the structure in Figure 2.12a, a) inside the dielectric slab (x,y)-plane and b) in the air and infinite dielectric (y,z)-plane.

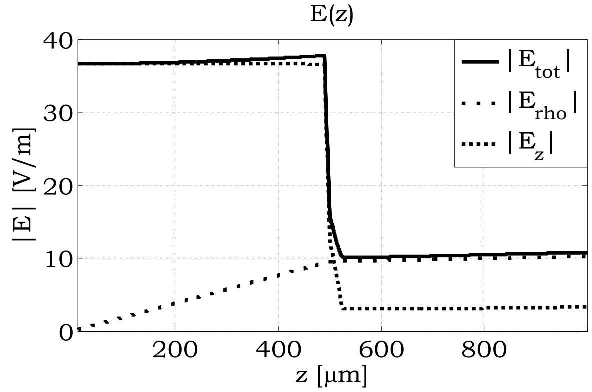

Figure 2.15: Total electric field as a function of height at $f = 45$ GHz and $\phi = 0$

in Figure 2.15. ρ is chosen to be a few wavelengths from the source, eliminating any near-field contributions excited by the elementary current source.

The fields calculated by CST can be verified using the exact same approach as was done with evaluating a surface-wave in a grounded dielectric slab. For this structure the residues for the fields inside the air-gap ($z < H$) are (2.32):

$$\begin{aligned}
\text{Res}[v_{TM}(k_\rho, z)]|_{k_\rho = k_{\rho,LW}} &= \frac{Z_d Z_{gap}}{D'(k_\rho)} \frac{\sin(k_{z0,LW} z)}{\sin(k_{z0,LW} H)} && \text{(2.32)a} \\
\text{Res}[i_{TM}(k_\rho, z)]|_{k_\rho = k_{\rho,LW}} &= \frac{Z_d Z_{gap}}{D'(k_\rho)} \frac{1}{Z_0} \frac{j\cos(k_{z0,LW} z)}{\sin(k_{z0,LW} H)} && \text{(2.32)b}
\end{aligned}$$

And the residues for the fields inside the infinite medium ($z > H$) are (2.33):

$$\begin{aligned}
\text{Res}[v_{TM}(k_\rho, z)]|_{k_\rho = k_{LW}} &= \frac{Z_d Z_{gap}}{D'(k_\rho)} e^{jk_{zd,LW} H} e^{-jk_{zd,LW} z} && \text{(2.33)a} \\
\text{Res}[i_{TM}(k_\rho, z)]|_{k_\rho = k_{LW}} &= \frac{Z_d Z_{gap}}{D'(k_\rho)} \frac{1}{Z_d} e^{jk_{zd,LW} H} e^{-jk_{zd,LW} z} && \text{(2.33)b}
\end{aligned}$$

In Eq. (2.32) and Eq. (2.33) we have Eq. (2.34):

$$\begin{aligned}
k_{z0,LW} &= \sqrt{k_0^2 - k_\rho^2} && \text{(2.34)a} \\
k_{zd,LW} &= +\sqrt{-(k_d^2 - k_\rho^2)} && \text{(2.34)b} \\
Z_0 &= \zeta_0 \frac{k_{z0,LW}}{k_0} && \text{(2.34)c} \\
Z_d &= \zeta_0 \frac{k_{zd,LW}}{k_d} && \text{(2.34)d} \\
Z_{gap} &= jZ_0 \tan(k_{z0} H) && \text{(2.34)e} \\
D(k_\rho) &= Z_s(k_\rho) + Z_{gap}(k_\rho) && \text{(2.34)f}
\end{aligned}$$

As before, the electric fields of the TM-leaky-wave in Figure 2.15 can be verified using these residues. This verification is shown in Figure 2.16 and Figure 2.17 for the electric field in the air-gap and infinite medium respectively. The fields obtained by calculating the residues are normalized to the amplitude of the electric fields from CST. Like we have seen in the case in the surface-wave, the pole found from the Green's functions (Figure 2.13) is responsible for the total electric field distribution.

With this, we will conclude our concise description of surface-wave poles and leaky-poles found in the Green's functions and the characterization of the fields associated to them. The relation between these propagating modes and the excitation of them when a strip or slot is in the presence in such stratification will be discussed in chapter 3 and chapter 4.

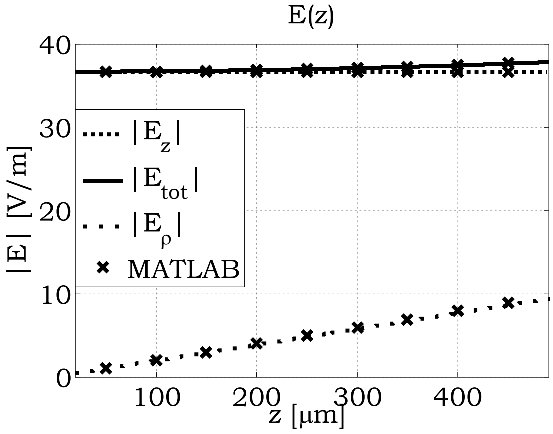

Figure 2.16: Total electric field in the air-gap as a function of height at $f = 45$ GHz and $\phi = 0$ verified with the Residue Theorem

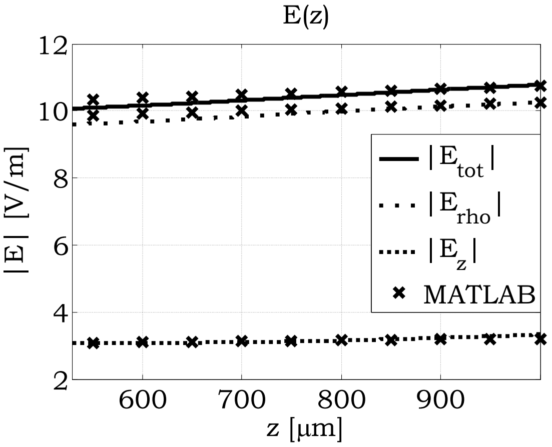

Figure 2.17: Total electric field in the dielectric medium as a function of height at $f = 45$ GHz and $\phi = 0$ verified with the Residue Theorem

Chapter 3

Quasi-analytical model for transmission line characterization

In this chapter, the quasi-analytical model is discussed which allows for a fast characterization of a wide variety of printed transmission lines in terms of propagation constant, characteristic impedance, effective dielectric constant and losses. These losses are composed out of conductor losses, dielectric losses and radiation losses into space- and surface-waves. For printed transmission lines these latter losses are of particular importance when the transverse dimensions of the transmission lines become significant in terms of wavelength. Transmission lines fabricated using current printed circuit board technologies are limited in its dimensions. Typical critical transverse dimensions are 100 μm in width and 127 μm in substrate height. When the transverse dimensions become significant in terms of wavelength ($\sim \lambda/20$ in line width and $\sim \lambda/4$ in substrate height), dynamic phenomena in the line become non-negligible and can have a significant influence on the main parameters of the transmission line. This quasi-analytical model allows for studying the effect of these dynamic phenomena on the main parameters of the transmission line.

The quasi-analytical model makes use of the transmission line formalism [15]- [16]. The Green's functions in this formalism are formulated according to the equivalent transmission line model as is explained in chapter 2. These Green's functions represent the solution to the integral equation of a magnetic or electric line current in the presence of stratified media. Therefore this representation can then be used for a wide range of printed transmission lines having different number of conductors and dielectric stratifications (e.g. a CPW in Figure 3.1). The transmission lines are assumed to be infinitely long along $\hat{x}$, the conductors infinitesimal in thickness and a homogeneity in the transverse $(\hat{x},\hat{y})$-plane.

In Section 3.1 we will start with a concise description of the construction of the integral equations (IE) used. Both the Electric Field Integral Equation (EFIE) and Continuity of Mag-

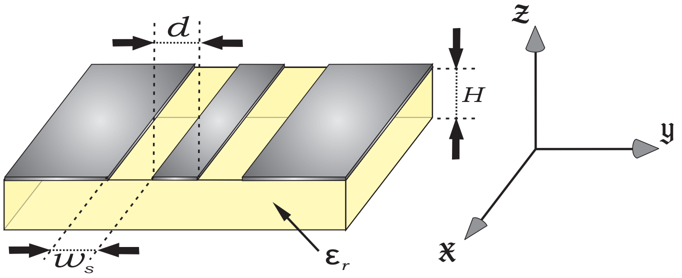

Figure 3.1: Example of a transmission line (Coplanar Waveguide) with its reference axis. w_s is the width of the slot (or strip for strip-type structure), d is the spacing between multiple lines, H and ε_r are respectively the height and the relative permittivity of the dielectric slab.

netic Field Integral Equation (CMFIE) will be combined into one expression. After rewriting the IE to the spectral domain and equating the integrands we will arrive at the transmission line formalism. This formalism is an expression for the longitudinal current running along the transmission line in the form of an inverse-Fourier transform. In Section 3.2 the singularities of the integrand of this inverse-Fourier transform, which is called the current spectrum, will be analyzed. Within this analysis a discussion regarding the physical meaning of the singularities will be conducted by relating the location of the singularities in the longitudinal spectral plane to the integration path in the transverse spectral plane. Subsequently, in Section 3.4, the model for obtaining the characteristic impedance of a specific propagating mode will be explained and related to the input impedance seen from the excitation port (in the model a Δ-gap excitation). Finally, in Section 3.5 and Section 3.6, the implementation of ohmic-, both conductor- and dielectric-, losses and superconductivity will be discussed respectively. Examples, validation and discussion of the model will be shown in chapter 4.

3.1 Construction of the Integral Equations (IE)

In this section the Integral Equations (IE) will be constructed. The IE will be imposed over the area of strip and slot where the fields over the width of these strips and slots will be averaged. After making an assumption regarding the transverse current distribution, the unknown in this system of equations will be the equivalent longitudinal current along the transmission line. This longitudinal current can be expressed in terms of an inverse-Fourier transform. Finding the singularities in the integrand of this inverse-Fourier transform, i.e. the current spectrum, forms the basis of characterizing the main propagating modes in the transmission line. For a more rigorous derivation of the IE, please refer to Appendix A. For the sake of simplicity, we will start with the derivation of the IE without taking into account any conductor losses; this will be done in Section 3.5 and more rigorously in Appendix B.

Two types of integral equations can be constructed; the Electric Field Integral Equation (EFIE) for strips in [15,21] and [22] or Continuity of Magnetic Field Integral Equation (CMFIE) in [16]. The EFIE can be expressed as Eq. (3.1),

$$\underline{\boldsymbol{e}}_{scatt}(x,y) = -\underline{\boldsymbol{m}}_{\Delta}(x,y) + \underline{\boldsymbol{e}}_{tot}(x,y) \tag{3.1}$$

In Eq. (3.1), $\underline{\boldsymbol{e}}_{scatt}$ and $\underline{\boldsymbol{m}}_{\Delta}$ are the tangential components of the scattered electric field and incident field respectively. The tangential total electric field $\underline{\boldsymbol{e}}_{tot}$ will only be non-zero when dealing with non-perfect conductors which will be discussed later on and can also be found in Appendix B. We will continue assuming we are dealing with Perfect Electric Conductors (PEC). For slot-type transmission lines, the CMFIE enforces the continuity of the magnetic field as in Eq. (3.2),

$$\underline{\boldsymbol{j}}_{\Delta} = \hat{\boldsymbol{z}} \times (\underline{\boldsymbol{h}}_{z>0} - \underline{\boldsymbol{h}}_{z<0}) \tag{3.2}$$

In Eq. (3.2), $\underline{\boldsymbol{j}}_{\Delta}$ is the excitation current and $\underline{\boldsymbol{h}}_{z>/<0}$ is the magnetic field above and below the transmission line. The incident field for the EFIE ($\underline{\boldsymbol{m}}_{\Delta}(x,y)$) and the excitation for the CMFIE ($\underline{\boldsymbol{j}}_{\Delta}(x,y)$) are modeled as a Δ-gap excitation ($\underline{\boldsymbol{s}}_{\Delta}(x,y)$) in the middle of the lines as is shown in Figure 3.2. For n coplanar lines, the excitation can be described as an excitation vector with elements as described in (3.3) for $i = 0 : n-1$. In (3.3), $d_y = d + w_s$ is the spacing between the centers of the coplanar lines.

$$s_{\Delta,i}(x,y) = s_{0,i} \cdot \mathrm{rect}\left(\frac{x}{\Delta}\right) \mathrm{rect}\left(\frac{y - id_y}{w_s}\right) \tag{3.3}$$

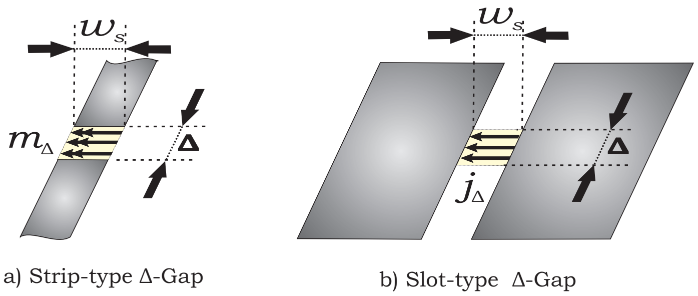

a) Strip-type Δ-Gap b) Slot-type Δ-Gap

Figure 3.2: Δ-Gap excitation $s_\Delta(x,y)$, a) for strip-type transmission lines: $m_\Delta(x,y)$ and b) slot-type transmission lines: $j_\Delta(x,y)$.

In (3.3), $s_{0,i}$ are the excitation coefficients to select any propagation modes. For example, in the developed software tool a maximum of two coplanar lines are possible. This leads to two possible propagating modes, common- and differential mode, having excitation coefficient vectors as in (3.4). The excitation vectors (3.3) for these modes in a coplanar waveguide (CPW) are visualized in Figure 3.3.

$$\underline{s}_0^{\text{common}} = \begin{bmatrix} 1 \\ 1 \end{bmatrix} \qquad \underline{s}_0^{\text{differential}} = \begin{bmatrix} 1 \\ -1 \end{bmatrix} \tag{3.4}$$

Combining the EFIE and CMFIE by following the steps in Appendix A will result in a spatial representation of the IE as in Eq. (3.5):

$$\frac{1}{w_s}\int_{w_s}\iint_S \tilde{\underline{g}}_{xx}(x-x',y-y')\underline{c}_{eq}(x',y')dx'dy'dy = \frac{1}{w_s}\int_{w_s}\underline{s}_\Delta(x,y)dy \tag{3.5}$$

where it can be seen that the integral equations are averaged over the width of the strip or slot. Also, the IE (3.5) is now in its scalar form where only the xx-component of the Green's function is required. In the formulation $\underline{c}_{eq}(x,y)$ are the equivalent magnetic or electric currents along the transmission line, which is the unknown in this system of equations. The current distribution along the line is assumed to be separable in space-dependency (3.6).

$$\underline{c}_{eq}(x,y) = \underline{c}(x)\cdot c_t(y) \tag{3.6}$$

In the case that the width of the line $w_s \ll \lambda$, the transverse dependence, $c_t(y)$ can be characterized by the quasi-static edge singularities (3.7).

$$c_t(y) = \frac{2}{w_s\pi}\frac{1}{\sqrt{1-(\frac{2y}{w_s})^2}} \tag{3.7}$$

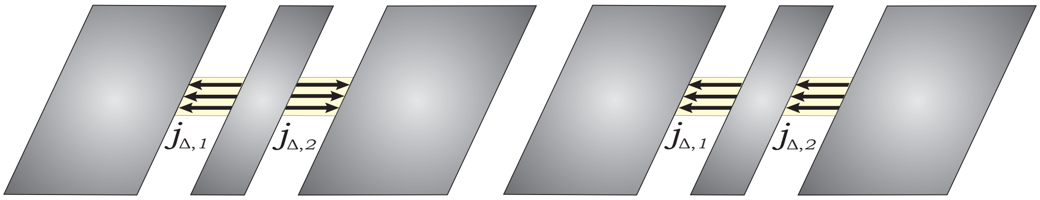

a) Differential excitation mode b) Common excitation mode

Figure 3.3: CPW excited by the Δ-Gap excitation vector in a) differential mode (3.4)a, b) in common mode (3.4)b.

After representing the pertinent integral equations (3.5) in the spectral domain and equating the integrands of the inverse Fourier transforms, the longitudinal electric or magnetic currents, $\underline{c}(x)$, along the transmission line can be expressed as an inverse Fourier transform in the longitudinal domain of the lines (3.8):

$$\underline{c}(x) = \frac{1}{2\pi}\int_{-\infty}^{\infty} \underline{\underline{D}}^{-1}(k_x)\cdot \underline{N}_0(k_x)e^{-jk_x x}dk_x \tag{3.8}$$

This expression includes multiple conductors. For the EFIE (CMFIE) the denominator $\underline{\underline{D}}(k_x)$ represents the average transverse electric (magnetic) field radiated by the equivalent currents on the strip (slot). It can, in turn, be expressed as a transverse spectral integration as in Eq. (3.9),

$$D_{n,i}(k_x) = \frac{1}{2\pi}\int_{-\infty}^{\infty} \tilde{G}_{xx}(k_x,k_y)C_t(k_y)\mathrm{sinc}\left(\frac{k_y w_s}{2}\right)e^{-jk_y(n-i)d_y}dk_y \tag{3.9}$$

with

$$\tilde{g}_{xx}(x,y) \xrightarrow{\mathcal{F}} \tilde{G}_{xx}(k_x,k_y) \tag{3.10}$$

$$c_t(y) = -\frac{2}{w_s\pi}\frac{1}{\sqrt{1-\left(\frac{2y}{w_s}\right)^2}} \xrightarrow{\mathcal{F}} C_t(k_y) = -J_0\left(\frac{k_y w_s}{2}\right) \tag{3.11}$$

$$n_{0,n}(x) = s_{0,n}\cdot \mathrm{rect}\left(\frac{x}{\Delta}\right) \xrightarrow{\mathcal{F}} N_{0,n}(k_x) = s_{0,n}\cdot \mathrm{sinc}\left(\frac{k_x\Delta}{2}\right) \tag{3.12}$$

In Eq. (3.9), $\tilde{G}_{xx}(k_x,k_y)$ is the spectral Green's function of the corresponding planar stratification in absence of the strip (slot) and $\underline{N}_0(k_x)$ is the Fourier transform of the longitudinal excitation law $\underline{n}_0(x) = \underline{s}_0\mathrm{rect}(\frac{x}{\Delta})$ from (3.3). The assumed edge singular distribution, $c_t(y)$ has an analytic Fourier Transform: $J_0(\frac{k_y w_s}{2})$. The averaging over the width of the strips (slots), leads to a sinc-function multiplication; $\mathrm{sinc}(\frac{k_y w_s}{2})$. The exponential term in the denominator accounts for the coupling between multiple lines. As an example, for a CPW, $\underline{\underline{D}}(k_x)$ will in that case be a 2×2-matrix where $D_{1,2}(k_x)$ and $D_{2,1}(k_x)$ describes the coupling between the lines.

The total current along the transmission line can be calculated by evaluating the inverse Fourier transform in Eq. (3.8) while the current contribution due to a specific propagation mode can be calculated by means of evaluating the residue in the singularity associated to this propagation mode. This procedure is explained in Section D.1. However, for the characterization of printed transmission lines we are not specifically interested in the distribution of the current running on the strip or slot, $\underline{c}(x)$. Instead, we are interested in the characteristics of the current associated to the main propagating mode. Characteristics such as the complex wavenumber and characteristic impedance can all be extracted from the singularities in the integrand of Eq. (3.8) and thus the spectral form of the longitudinal current $\underline{c}(x)$, which we will call the current spectrum (3.13).

$$\underline{C}(k_x) = \underline{\underline{D}}^{-1}(k_x)\cdot \underline{N}_0(k_x) \tag{3.13}$$

In the following section we will investigate the singularities in the current spectrum. We will show that care have to be taken in choosing the integration path in the transverse domain in (3.9) in order to acknowledge the found singularities as propagating modes to be actually physically valid.

3.2 Current spectrum

In the previous section the IE was constructed for both strip-type and slot-type printed transmission lines. Subsequently, it turned out that the longitudinal current along the line could be expressed as an inverse-Fourier transform of its current spectrum $\underline{C}(k_x)$.

$$\underline{C}(k_x) = \underline{\underline{D}}^{-1}(k_x) \cdot \underline{N}_0(k_x)$$

Referring to the discussion regarding the singularities in Eq. (2.7) (subsection 2.2.2), we already know that the dominant contributions to $\underline{c}(x)$ will be originating from the singularities in the integrand, i.e. the current spectrum $\underline{C}(k_x)$. Since $N_{0,n}(k_x)$ (3.12) does not contain any singularities, the inverse Fourier transform of Eq. (3.8), depends mostly on the polar singularities in $\underline{\underline{D}}^{-1}(k_x)$. In this section we will start by explaining the procedure for obtaining these singularities. Secondly, we will see that the location of the singularities in the longitudinal k_x domain is non-trivial as it depends on the transverse integration path in k_y (3.9). The impact of the integration path on the excitation of a microstrip is extensively studied by Mesa in [12, 15, 21, 23].

3.2.1 Dispersion equation

The inverse matrix $\underline{\underline{D}}^{-1}(k_x)$ can be represented as

$$\underline{\underline{D}}^{-1}(k_x) = \frac{\underline{\underline{A}}(k_x)}{|\underline{\underline{D}}(k_x)|} \tag{3.14}$$

where

$$\underline{\underline{A}}(k_x) \quad \text{is the adjugate of } \underline{\underline{D}}(k_x) \tag{3.15)a}$$

$$|\underline{\underline{D}}(k_x)| \quad \text{is the determinant of } \underline{\underline{D}}(k_x) \tag{3.15)b}$$

When this decomposition (3.14) is substituted in, (3.8) we obtain:

$$\underline{c}(x) = \frac{1}{2\pi} \int_{-\infty}^{\infty} \frac{\underline{\underline{A}}(k_x)}{|\underline{\underline{D}}(k_x)|} \cdot \underline{N}_0(k_x) e^{-jk_x x} dk_x \tag{3.16}$$

Finding the singularities, and thus the propagating modes, in a printed transmission line can be done by annulling the determinant of $\underline{\underline{D}}(k_x)$ Eq. (3.17)

$$|\underline{\underline{D}}(k_x)| = 0 \tag{3.17}$$

Eq. (3.17) is called the dispersion equation. However, solving the dispersion equation for coplanar lines will result in two possible solutions; differential and common propagating modes as is shown for a coupled microstrip in Figure 3.4. By means of the excitation coefficients in Eq. (3.4), one of the solutions of the dispersion equation, either associated to the differential or common mode excitation, will be canceled in the current spectrum (3.13). So rather than annulling the determinant of the denominator $|\underline{\underline{D}}(k_x)| = 0$, we will find the singularities in the current spectrum (3.18):

$$\underline{C}^{-1}(k_x) = 0 \tag{3.18}$$

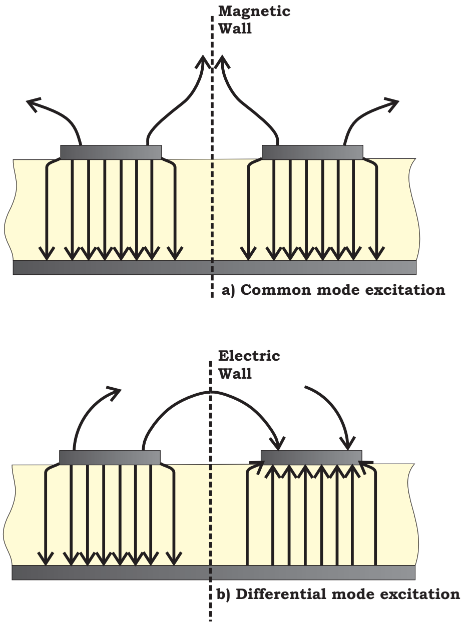

Figure 3.4: Electric field distribution for a) common mode excitation and b) differential mode excitation for a coupled microstrip.

The developed MATLAB-tool solves this dispersion equation by using a Taylor series expansion around an initial guess point, k_{init}, for the complex wavenumber of the main propagating mode. A sensible initial guess point can be the average propagation constant of two adjacent stratifications Eq. (3.19).

$$k_{init} = \sqrt{\frac{k_{up}^2 + k_{down}^2}{2}} \tag{3.19}$$

Performing a Taylor series expansion of (3.18) around the initial guess point of the complex wavenumber of the main propagating mode (3.19) results in the dispersion equation as is shown in Eq. (3.20).

$$\underline{C}^{-1}(\underline{k}_{init}) + [\underline{C}^{-1}(\underline{k}_{init})]'(\underline{k}_{mode} - \underline{k}_{init}) \approx 0 \tag{3.20}$$

Solving for $\underline{k}_{mode}$ results in the following approximation (3.21).

$$\begin{align} \underline{k}_{mode} &\approx \underline{k}_{init} - \underline{k}_{correction} \tag{3.21} \\ \underline{k}_{correction} &= \underline{C}^{-1}(\underline{k}_{init})([\underline{C}^{-1}(\underline{k}_{init})]')^{-1} \tag{3.22} \end{align}$$

The obtained approximation for $\underline{k}_{mode}$ can thereafter be used as a new $\underline{k}_{init}$ for another iteration towards the true value of $\underline{k}_{mode}$. The implementation of this convergence method is explained in Appendix E and is ensuring that, even with an inaccurate guess-point k_{init}, the obtained complex wavenumber is accurately approximated.

The location of the investigated spectral point in the complex spectral plane k_x, determines the mathematically correct integration path in the transverse domain (k_y). Care has to be taken in guaranteeing that the radiation condition is being satisfied. The procedure for finding the correct integration path can be explained by both studying the longitudinal spectral plane (k_x) and the transverse spectral plane (k_y) which will be done in the following subsections.

3.2.2 Longitudinal spectral plane

First we will investigate the singularities in the current spectrum (3.13); i.e. the longitudinal spectral plane. Apart from the poles associated to the propagating modes along the printed transmission line, the spectral plane will contain singularities in the form of branch-points and its associated branch-cuts. These branch-points and -cuts will for example appear when an infinite stratification is present. Crossing these branch-cuts leads to different Riemann sheets. Changing the integration path into the different Riemann sheets allows for finding not only bounded modes but also improper leaky modes. When the transmission lines are printed in between two infinite dielectrics, as in the case of circuits placed at the bottom of a dielectric lens, the main propagating mode could become leaky.

In order to comprehend the important regions in the spectral plane of printed transmission lines, three possible spectral planes are visualized in Figure 3.5, Figure 3.6 and Figure 3.7. In Figure 3.5 the spectral plane of a CPW printed in between two infinite dielectrics is depicted. In Figure 3.6 the plane of a CPW printed on a finite, but large, substrate is shown. Finally, in Figure 3.7, the spectral plane of a CPW printed in between two infinite dielectrics is shown, however, in contrast to Figure 3.5 there is an air-gap between the high dense infinite dielectric and the CPW. In all spectra, the integration path C_x, from $-\infty$ to ∞, allows for calculating the total current along the transmission line by means of evaluating the inverse Fourier transform in Eq. (3.8) along C_x. Note that this integration path encloses all the propagating modes and possible space-wave. It will therefore differ from the current calculated by the Residue Theorem (D.14) which is only associated to the current contribution due to the investigated spectral point.

We will start by discussing the nature of all the observed singularities in the shown current spectra. Also, different regions associated to different characteristic propagating modes can be observed. After discussing these different regions we will investigate the associated transverse integration paths where we take a leaky-mode of a slotline printed in between two infinite media as an example. For this structure an analytical solution exist for $D(k_x)$ [16]. Finally, this reasoning will be extrapolated for all other possible transverse integration paths.

Branch-points and its associated branch-cuts

Two branch points which can appear in the longitudinal domain are located at $k_x = \pm k_i$ for $i = 1,2$ [17]. k_1 and k_2 are introduced by the spectral domain Green's functions and are a consequence of the infinite top and bottom media. Starting at these branch points, branch cuts have to be defined allowing to enter the different Riemann-sheets. Two square-root type of branch cuts arise from $k_{z,i} = \sqrt{k_i^2 - k_\rho^2}$. This square-root will have two solutions as is defined in Eq. (3.23).

$$k_{z,i} = \sqrt{k_i^2 - k_\rho^2} = \begin{cases} k_{z,i} = -j\sqrt{-(k_i^2 - k_\rho^2)} & \text{Top Riemann-sheet} \\ k_{z,i} = +j\sqrt{-(k_i^2 - k_\rho^2)} & \text{Bottom Riemann-sheet} \end{cases} \tag{3.23}$$

The first solution, $k_{z,i} = -j\sqrt{-(k_i^2 - k_\rho^2)}$, will be located in the top Riemann-sheet and is verifying the radiation condition. Propagating modes found on this sheet are generally related to bounded, i.e. non-attenuative, modes. The second solution, $k_{z,i} = +j\sqrt{-(k_i^2 - k_\rho^2)}$, will be located on the bottom Riemann-sheet. The modes found on this sheet are complex improper; they do not verify the radiation condition. That they do not verify the radiation condition does not automatically mean that the modes are not physically valid. The CPW in Figure 3.5 will radiate in the denser medium with $Im(k_{z,i}) > 0$. However, since $Im[k_{mode}] < 0$ and the fact that the lines are in practice not infinitely long, the fields will not go to infinity when $z \to \infty$. Apart from the discussed square-root type of branch-cut, additional logarithmic-type of branch cuts appear as is visualized in the spectral planes. These logarithmic-type of branch-cuts are a consequence of the Hankel-function in the analytical form of $\underline{\underline{D}}(k_x)$ [16]; $H_0^{(2)}(\frac{w_s}{4}\sqrt{k_i^2 - k_x^2})$.

Another type of branch-point which can appear in the spectrum is depicted in Figure 3.6 and 3.7 by k_{SFW} and k_{LW} respectively. In Figure 3.6, k_{SFW} is associated to a surface-wave in the dielectric slab. Referring to subsection 2.3.1, we know that a surface-wave travel without attenuation. It does not leak into the infinite medium and therefore k_{SFW} is located on the real axis in the spectrum (for lossless dielectrics), and in the top Riemann-sheet with respect to the infinite medium k_1 (3.24). A possible mode exciting such surface-wave will be located on the bottom Riemann sheet with respect to k_{SFW}. Please note that these Riemann-sheets are additional to the Riemann-sheets of the infinite medium (3.23). In other words, a propagating mode exciting a surface-wave mode should be located on the top Riemann-sheet with respect to k_1 but on the bottom Riemann-sheet with respect to k_{SFW}.

$$k_{z,SFW} = -j\sqrt{-(k_1^2 - k_{SFW}^2)} \tag{3.24}$$

In Figure 3.7, k_{LW} is associated to a leaky-wave in the air-gap. Now referring to subsection 2.3.2, we know that a leaky-wave is radiating into the denser infinite medium and therefore located on the bottom Riemann-sheet with respect to this medium (3.25). The leaky wave branch-point k_{LW} will have an imaginary part (2.27) in contrary to the real-valued surface-wave branch-points . A propagating mode exciting a leaky-wave should be located on the bottom Riemann-sheet with respect to the infinite medium and on the bottom Riemann-sheet with respect to the leaky-wave pole.

$$k_{z,LW} = +j\sqrt{-(k_2^2 - k_{LW}^2)} \tag{3.25}$$

The surface-wave condition as is visualized in Figure 3.6 and Figure 3.7 will be discussed in Section 3.3. For now we can summarize that the first condition for a leaky- or surface-wave to be excited is when Eq. (3.26) is satisfied.

$$Re(k_{mode}) < Re(k_{LW/SFW}) \tag{3.26}$$

The second condition for a leaky- or surface-wave to be excited is as we discussed in this section; a propagating mode should be located on the bottom-Riemann-sheet with respect to a surface-wave-mode or a leaky-wave mode, i.e. below the branch-cuts in the spectra 3.6 and 3.7 associated to k_{SFW} and k_{LW}.

At this point we have discussed all the important singularities found in the longitudinal spectral plane. We have seen that propagating modes can have different characteristics in terms of leakage into infinite dielectric or into leaky- and surface-waves. These characteristics determine whether $Im(k_{z,1})$ and/or $Im(k_{z,2})$ should be greater or less than 0. With this in mind, different regions of the spectra in Figure 3.5-3.7 will be discussed now.

Mathematically correct regions of the spectrum

The spectral plane can now be divided in three different regions, each requiring different integration paths in order to ensure that the obtained solutions to the dispersion equation are physically valid. Depending on the fact whether or not the mode will radiate into the infinite medium,

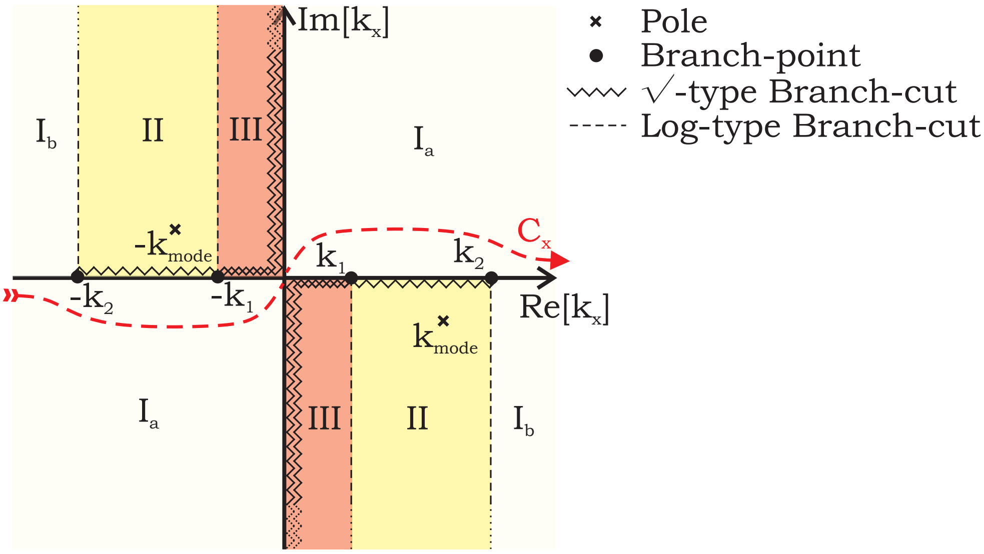

Figure 3.5: Longitudinal spectral plane (k_x) for a CPW printed between two infinite dielectrics.

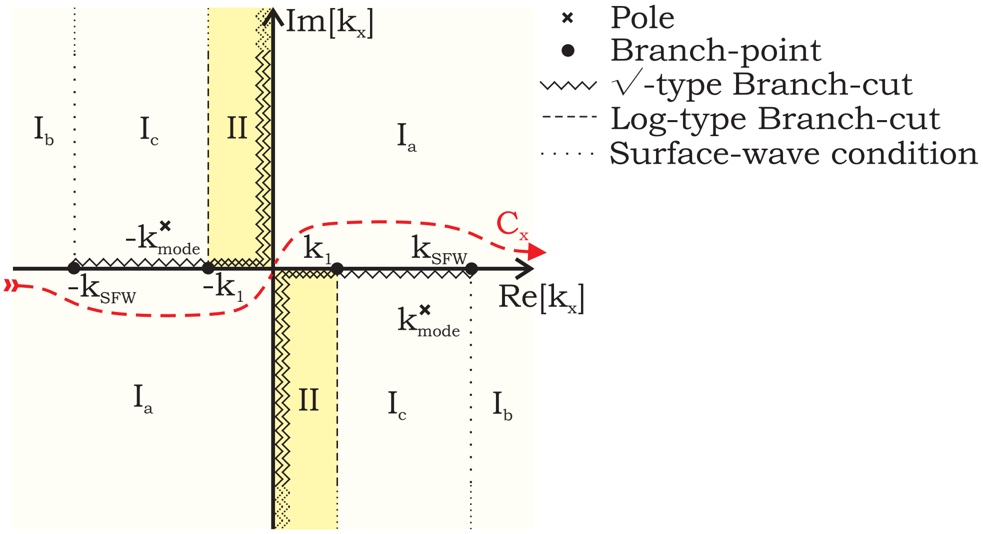

Figure 3.6: Longitudinal spectral plane (k_x) for a CPW printed onto a finite slab exciting a TM_0-surface wave.

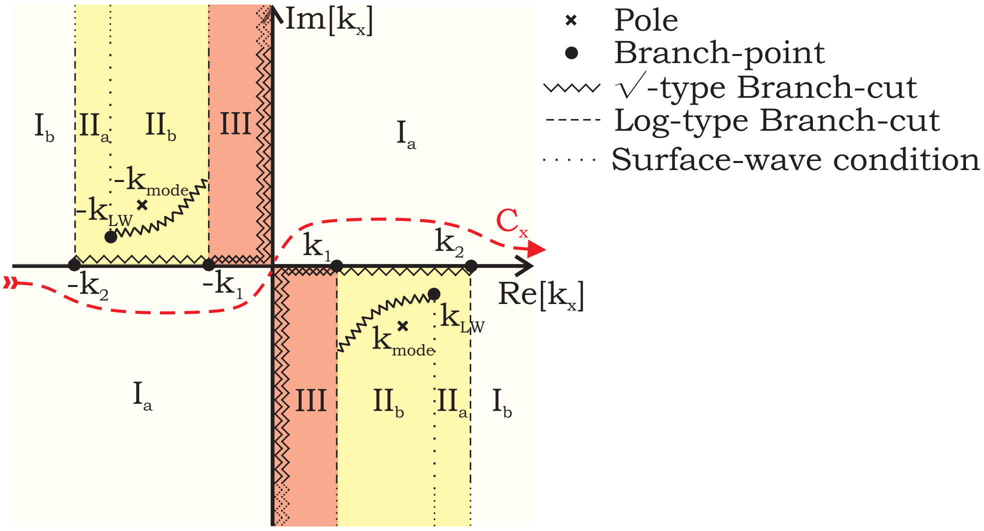

Figure 3.7: Longitudinal spectral plane (k_x) for a CPW close by a high dense infinite medium.

$Im(k_{z,1})$ and/or $Im(k_{z,2})$ should be greater or less than 0. From Eq. (3.23) we know that both solutions lie on a different Riemann-sheet. The three regions, as visualized in Figures 3.5-3.7, are:

- **Region I**: Top Riemann-sheet with respect to both infinite media $k_{z,1}$ and $k_{z,2}$; $Im(k_{z,1}) < 0$ and $Im(k_{z,2}) < 0$). The propagation modes found in this regions will not radiate into the infinite media. Region I is subdivided into three sub-regions.
  - *Region* I_a: According to our definition of the propagation constant, which is $k_{mode} = \beta - j\alpha$, it is not possible to find any propagating modes in this region. A mode found in Region I_a will actually grow in magnitude with x increasing which is not possible.
  - *Region* I_b: In this region, the bounded modes will be located. In the case that no other losses exist, i.e. conductor- and dielectric losses, the propagating mode will be located on the real axis.
  - *Region* I_c: Any modes found in region I_c are exciting a surface-wave. The surface-wave condition from Eq. (3.26) is fulfilled and the propagating mode is on the bottom Riemann-sheet with respect to the surface-wave branch-point. The wavenumber of the propagating mode must be complex as it is leaking into the surface-wave.

- **Region II**: Top Riemann-sheet for $k_{z,1}$ and bottom Riemann-sheet for $k_{z,2}$; $Im(k_{z,1}) < 0$ and $Im(k_{z,2}) > 0$. Radiation occurs into the denser infinite medium. The wavenumbers of these modes will therefore always have an (negative) imaginary part. This region can be subdivided into two sub-regions.
  - *Region* II_a: In this sub-region, the transmission line will directly radiate into the denser infinite medium.
  - *Region* II_b: A leaky-wave mode, such as the example in subsection 2.3.2 is excited. The surface-wave condition from Eq. (3.26) is fulfilled and the main propagating mode is located on the bottom Riemann-sheet with respect to the leaky-wave branch-point.

- **Region III**: Bottom Riemann-sheets for both $k_{z,1}$ and $k_{z,2}$; $Im(k_{z,1}) > 0$ and $Im(k_{z,2}) > 0$. Radiation occurs in both infinite media. Propagating modes located in this region are not only leaking into the denser dielectric but also in the less dense dielectric (e.g. space-wave excitation). Just as in region II_b, it is also possible that a leaky-wave modes is excited. For this reason, region III can also be divided into two sub-regions as is described for Region II. This is not depicted in Figure 3.7.

We now defined regions with the correct Riemann-sheets with respect to the infinite media and possible surface- and leaky-wave modes. Propagating modes found in the defined regions are physically valid. Propagating modes found on any other Riemann-sheets are improper and not physical. Therefore we have to make sure that, when looking for a solution of the dispersion equation, we search on the correct Riemann-sheet for the main propagating mode. In the following subsection we will explain the integration paths needed in the transverse domain (3.9) in order to enter these sheets correctly.

3.2.3 Transverse spectral plane

The three regions and its sub-regions we defined in the longitudinal spectral plane all require a different integration path in the transverse spectral plane in order to reach the correct Riemann-sheets. In Figure 3.8 an arbitrary transverse spectral plane is shown where $k_{t,i}$ are the branch-points of the infinite media according to Eq. (3.27).

$$k_{t,i} = \sqrt{k_i^2 - k_x^2} \tag{3.27}$$

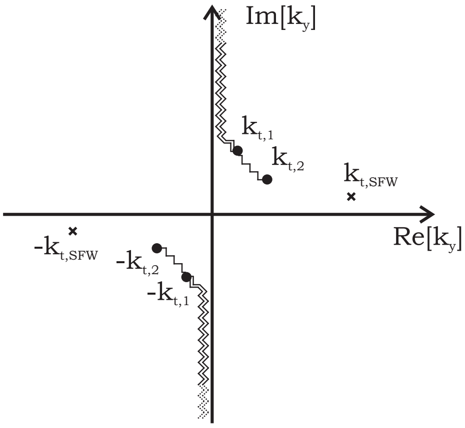

Figure 3.8: Generalized transverse spectral plane (k_y) with branch-points and -cuts associated to infinite media and a pole associated to an intrinsic surface-wave.

Equivalently, the location of $k_{t,SFW}$ can be calculated from (3.28):

$$k_{t,SFW} = \sqrt{k_{SFW}^2 - k_x^2} \tag{3.28}$$

The branch-cuts running from the branch-points associated to the infinite media are defined to run along the hyperbolas defined by (3.29). With this definition, the branch-cuts are defined on the boundary between the top- and bottom Riemann sheets with respect to the infinite media.

$$Im(k_z^2) = Re(k_z)Im(k_z) = 0 \tag{3.29}$$

Crossing these branch-cuts will therefore allow for entering the different Riemann-sheets associated to $Im(k_z) = \pm\alpha_z$. In this section we will discuss the integration path around or through the branch-points, -cuts and poles in Figure 3.8 in order to find the propagating modes in the different regions of the longitudinal spectral plane as is discussed in the previous section. We will start this discussion by investigating the integration path of a slotline printed in between two infinite media as an analytical solution of $D(k_x)$ exists [16].

Slotline printed in between two infinite dielectrics

The denominator $D(k_x)$ of a slotline printed in between two infinite dielectrics can be expressed as Eq. (3.30) [16].

$$D(k_x) = -\frac{1}{2\pi}\int_{\infty}^{\infty} G(k_x,k_y)J_0\left(\frac{w_s k_y}{2}\right)dk_y \tag{3.30}$$

Comparing (3.30) with our version of the denominator in (3.9), we can see that the fields are not averaged over the width of the strip and slot (but taken at the centers of the line $y = 0$) resulting in an absence of the *sinc*-function. Also, $D(k_x)$ is now a scalar, rather than a $N \times N$-matrix; no multiple conductors are taken into account resulting in an absence of the exponential in (3.9). The spectral integration in (3.30) is then performed by using the identity

$$\int_{-\infty}^{\infty} \frac{J_0(\frac{w_s k_y}{2})}{\sqrt{k_i^2 - k_x^2 - k_y^2}} dk_y = \pi J_0\left(\frac{w_s}{4}\sqrt{k_i^2 - k_x^2}\right)H_0^{(2)}\left(\frac{w_s}{4}\sqrt{k_i^2 - k_x^2}\right) \tag{3.31}$$

for $i = 1, 2$. Resulting in the analytical result for $D(k_x)$:

$$D(k_x) = \frac{1}{2k_0\zeta_0}\sum_{i=1}^{2}(k_i^2 - k_x^2)J_0\left(\frac{w_s}{4}\sqrt{k_i^2 - k_x^2}\right)H_0^{(2)}\left(\frac{w_s}{4}\sqrt{k_i^2 - k_x^2}\right) \tag{3.32}$$

for $i = 1,2$. The summation accounts for the infinite top and bottom media which are separated in the Green's functions. Having this said, we will investigate the integration path C_y and the restrictions on the signs of the square-roots in order to arrive at the analytical solution of $D(k_x)$ (3.33):

$$D(k_x) = \frac{1}{\pi}\int_{C_y}\frac{J_0(\frac{w_s k_y}{2})}{\sqrt{k^2 - k_x^2 - k_y^2}}dk_y = J_0\left(\frac{w_s}{4}\sqrt{k^2 - k_x^2}\right)H_0^{(2)}\left(\frac{w_s}{4}\sqrt{k^2 - k_x^2}\right) \tag{3.33}$$

First, let us assume that $|k_x|^2 < 2k_0$ and $w < \lambda_0/1000$. In this case the argument of the Bessel-function $|\frac{w_s}{4}\sqrt{k_i^2 - k_x^2}| < \frac{k_0 2\pi}{k_0 1000} = 0.006$ so that $J_0(\frac{w_s}{4}\sqrt{k_i^2 - k_x^2}) \approx 1$ and (3.33) results in:

$$D(k_x) = \frac{1}{\pi}\int_{C_y}\frac{J_0(\frac{w_s k_y}{2})}{\sqrt{k^2 - k_x^2 - k_y^2}}dk_y \approx H_0^{(2)}\left(\frac{w_s}{4}\sqrt{k^2 - k_x^2}\right) \tag{3.34}$$

The integration path C_y in Eq. (3.34) can be decomposed into three distinct contributions as is shown in Eq. (3.35). The first term integrates between the branch-points $\pm k_t$ (3.27) while the second and third contributions closes the integration to $-\infty$ and $+\infty$ respectively.

$$D(k_x) = \frac{1}{\pi}\int_{-k_t}^{k_t}\frac{1}{\sqrt{k_t^2 - k_y^2}}dk_y + \frac{1}{\pi}\int_{-\infty}^{-k_t}\frac{J_0(\frac{w_s k_y}{2})}{\sqrt{k_t^2 - k_y^2}}dk_y + \frac{1}{\pi}\int_{k_t}^{\infty}\frac{J_0(\frac{w_s k_y}{2})}{\sqrt{k_t^2 - k_y^2}}dk_y \approx H_0^{(2)}\left(\frac{w_s k_t}{4}\right) \tag{3.35}$$

Approximating the Hankel-function as $H_0^{(2)}(\frac{w_s k_t}{4}) = J_0(\frac{w_s k_t}{4}) - jY_0(\frac{w_s k_t}{4}) \approx 1 - jY_0(\frac{w_s k_t}{4})$ brings us to the following equalities:

$$\begin{aligned}
\frac{1}{\pi}\int_{-k_t}^{k_t}\frac{1}{\sqrt{k_t^2 - k_y^2}}dk_y &= 1 && \text{(3.36)a}\\
\frac{1}{\pi}\int_{-\infty}^{-k_t}\frac{J_0(\frac{w_s k_y}{2})}{\sqrt{k_t^2 - k_y^2}}dk_y + \frac{1}{\pi}\int_{k_t}^{\infty}\frac{J_0(\frac{w_s k_y}{2})}{\sqrt{k_t^2 - k_y^2}}dk_y &= -jY_0\left(\frac{w_s k_t}{4}\right) && \text{(3.36)b}
\end{aligned}$$

We want to extract the signs of the square-roots in order for these equalities to be true. With this knowledge we can then deduct on which Riemann-sheet we have to integrate for each integration contribution in Eq. (3.35). We will start by applying a change of integration parameters:

$$\begin{aligned}
&\sqrt{k_t^2 - k_y^2} = k_t\cos(\theta)\\
\rightarrow &k_t^2 - k_t^2\cos^2(\theta) = k_y^2\\
\rightarrow &k_t^2(1 - \cos^2(\theta)) = k_y^2\\
\rightarrow &k_t^2\sin^2(\theta) = k_y^2\\
\rightarrow &k_t\sin(\theta) = k_y
\end{aligned}$$

and

$$\frac{dk_y}{d\theta}d\theta = k_t\cos(\theta)\,d\theta$$

So that we can see that the equality in (3.36)a is indeed satisfied:

$$\frac{1}{\pi}\int_{-\pi/2}^{\pi/2}\frac{1}{k_t\cos(\theta)}k_t\cos(\theta)\,d\theta = 1 \tag{3.37}$$

Now the key thing to note here is the restriction on the sign of the square-roots in the change of parameters; $\sqrt{k_t^2-k_y^2} = k_t\cos(\theta)$ where $k_t = \sqrt{k^2-k_x^2}$. The integration range $-\frac{\pi}{2} \leq \theta \leq \frac{\pi}{2}$ is completely real, therefore $\cos(\theta)$ is strictly real and positive in this integration range. This change of variables is therefore only valid when the sign of the imaginary part on the right-hand side $Im[k_t]$ is equal to the sign of the imaginary part on the left-hand side $Im[\sqrt{k_t^2-k_y^2}]$. That is:

$$Im[k_z] = Im[\sqrt{k^2-k_x^2}] \tag{3.38}$$

Now, a physical propagating mode along the transmission line verifies $Re[k_x] > 0$ and $Im[k_x] < 0$, resulting in $\sqrt{k^2-k_x^2} = \pm(a+jb)$. Therefore also $k_z = \pm(c+jd)$. Since $Re[k_z] > 0$ (outgoing wave) we know that we should integrate in the bottom Riemann-sheet with respect to the infinite medium, i.e. $Im[k_z] > 0$.

Secondly, we would like to investigate the restrictions on the square-roots on the second equality, Eq. (3.36)b. Although we did not, yet, find an analytical derivation of this restriction, numerical evaluations of Y_0 and the integrals in Eq. (3.36)b show that in order for this equality to be true $Im[k_z] < 0$, i.e. we should integrate on the top Riemann-sheet.

So we can summarize that for $|k_y| < k_t$ we need to integrate on the bottom Riemann-sheet, while for $|k_y| > k_t$ we need to integrate on the top Riemann-sheet as is shown in Eq. (3.39).

$$D(k_x) = \begin{cases} \frac{1}{\pi}\int_{-\infty}^{-k_t}\frac{J_0(\frac{w_s k_y}{2})}{\sqrt{k_t^2-k_y^2}}dk_y & \text{Top Riemann-sheet; } Im[k_z] < 0 \\ +\frac{1}{\pi}\int_{-k_t}^{k_t}\frac{1}{\sqrt{k_t^2-k_y^2}}dk_y & \text{Bottom Riemann-sheet; } Im[k_z] > 0 \\ +\frac{1}{\pi}\int_{k_t}^{\infty}\frac{J_0(\frac{w_s k_y}{2})}{\sqrt{k_t^2-k_y^2}}dk_y & \text{Top Riemann-sheet; } Im[k_z] < 0 \end{cases} \tag{3.39}$$

This study shows how to cross the branch-cuts and on what Riemann-sheet to integrate. In the next subsection, we will extend this investigation on all other regions we defined in the complex spectral plane. First we will give an example to show that using the integration path in Eq. (3.39) gives a valid and physical solution. Also, it will be shown that when the integration in Eq. (3.36)b is performed on the bottom Riemann-sheet, rather than the top Riemann-sheet, the dispersion equation can not be solved.

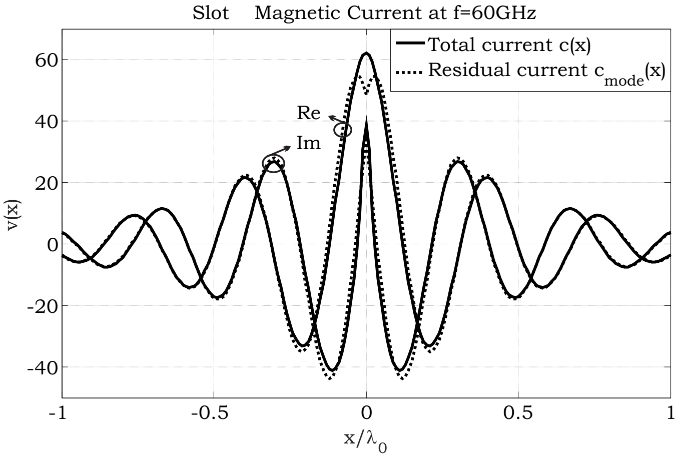

Figure 3.9: Magnetic current along the slot. Total current, $c(x)$, is calculated via Eq. (3.8). Residual current is the current contribution of the leaky-wave pole k_{mode}

In order to verify that the integration path in Eq. (3.39) is not only mathematically correct, but also results in a physical solution of the dispersion equation, we will calculate the magnetic current running along a slotline at $f = 60$ GHz, with $w_s = 180\mu$m ($\equiv 0.036\lambda_0$), $\varepsilon_r = 11.7$. This is shown in in Figure 3.9. The total current, $c(x)$, is calculated by performing the inverse Fourier transform (3.8) with the the integration path C_x from Figure 3.5. The residual current $c_{mode}(x)$ is the residual current distribution associated to the solution of the dispersion equation. The residual current can be calculated via Eq. (D.14), which is derived in Section D.1. It can be seen that the solution to the dispersion is indeed not only mathematically but also physically valid.

Secondly, in order to show that no (valid) solution exist when the integration in $|k_y| > k_t$ (first and third term in Eq. (3.39)) is performed on the bottom Riemann-sheet, we will show the magnetic current spectrum. For the mathematically valid integration path according to Eq. (3.39)

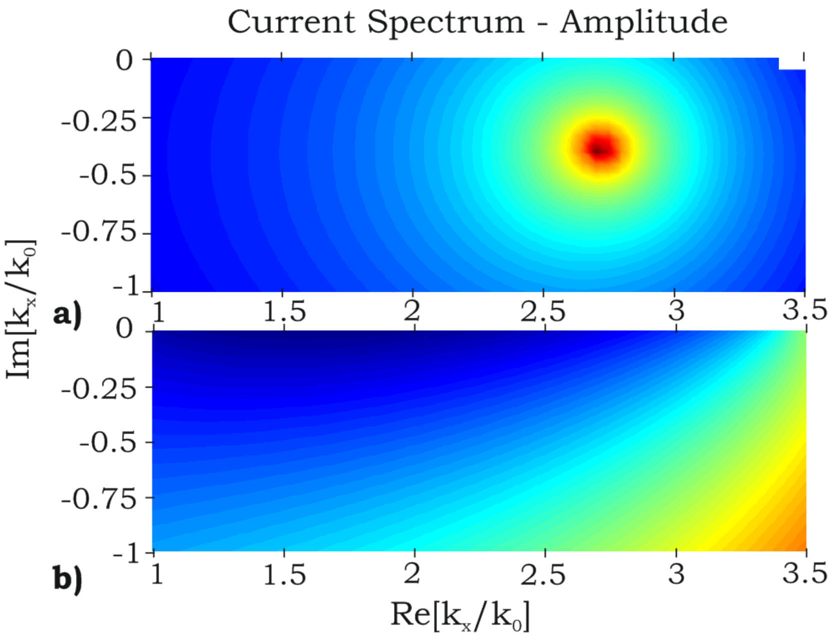

Figure 3.10: Magnetic current spectrum of a slotline at $f = 60$ GHz, with $w_s = 180\mu$m ($\equiv 0.036\lambda_0$), $\varepsilon_r = 11.7$; a) Transverse integration path according to Eq. (3.39), b) Transverse integration path entirely on the bottom Riemann sheet with respect to the infinite medium k.

(i.e. $|k_y| > k_t$ on top Riemann-sheet and $|k_y| < k_t$ on bottom Riemann-sheet), the magnetic current spectrum of this slotline can be seen in Figure 3.10a where the main propagating mode can be clearly distinguished. The residual current contribution of this observed pole is used for $c_{mode}(x)$ in Figure 3.9. When also the integration in $|k_y| > k_t$ is performed on the bottom Riemann-sheet we obtain the current spectrum in Figure 3.10b. No solution to the dispersion equation exist. In fact the current spectrum in increasing in magnitude with increasing $|k_x|$.

Transverse integration paths

Now we have shown how two enter the different Riemann-sheets in the transverse spectral domain in order to let $D(k_x)$ converge and actually results in a valid solution of the dispersion equation, we can summarize the integration paths required to be taken for the different regions in the longitudinal spectral plane (see Figure 3.5, Figure 3.6 and Figure 3.7).

When the mode is located in **Regions I**$_b$ or **I**$_c$, it will only verify the radiation condition when both $Im(k_{z,1}) < 0$ and $Im(k_{z,2}) < 0$. This means that with respect to both branch-points k_1 and k_2 one must stay on the top Riemann-sheets; see Figure 3.11a and b. Additionally, when a surface-wave mode is present, and also excited ($\beta_{mode} < \beta_{SFW}$ [11]), the surface-wave poles ($-k_{SFW}$ and k_{SFW}) have to be enclosed by the integration path (Figure 3.11b).

If the mode is located in **Region II**, $Im(k_{z,1}) < 0$ and $Im(k_{z,2}) > 0$. The bottom Riemann-sheet with respect to k_2 have to be entered by means of the transverse integration path shown in Figure 3.11c and d. Additionally, when a leaky-wave mode is present, and excited, the leaky-wave poles ($-k_{LW}$ and k_{LW}) have to be enclosed by the integration path (Figure 3.11d).

In the case that the mode is located in **Region III**, there is a mode which is also radiating in the less dense dielectric (i.e. usually a space-wave), $Im(k_{z,1}) < 0$ and $Im(k_{z,2}) < 0$. The transverse integration path enters the bottom Riemann-sheets with respect to both k_1 and k_2 as is shown in Figure 3.11e. Again, when a leaky-wave mode is present, and excited, the leaky-wave poles have to be enclosed by the integration path (Figure 3.11f).

Concluding from this study we can say that when analyzing a solution for k_{mode} from the dispersion equation, one has to make sure that the location of these solutions in the longitudinal spectral planes are corresponding with a transverse integration path in (3.9) which makes them physically and mathematically valid.

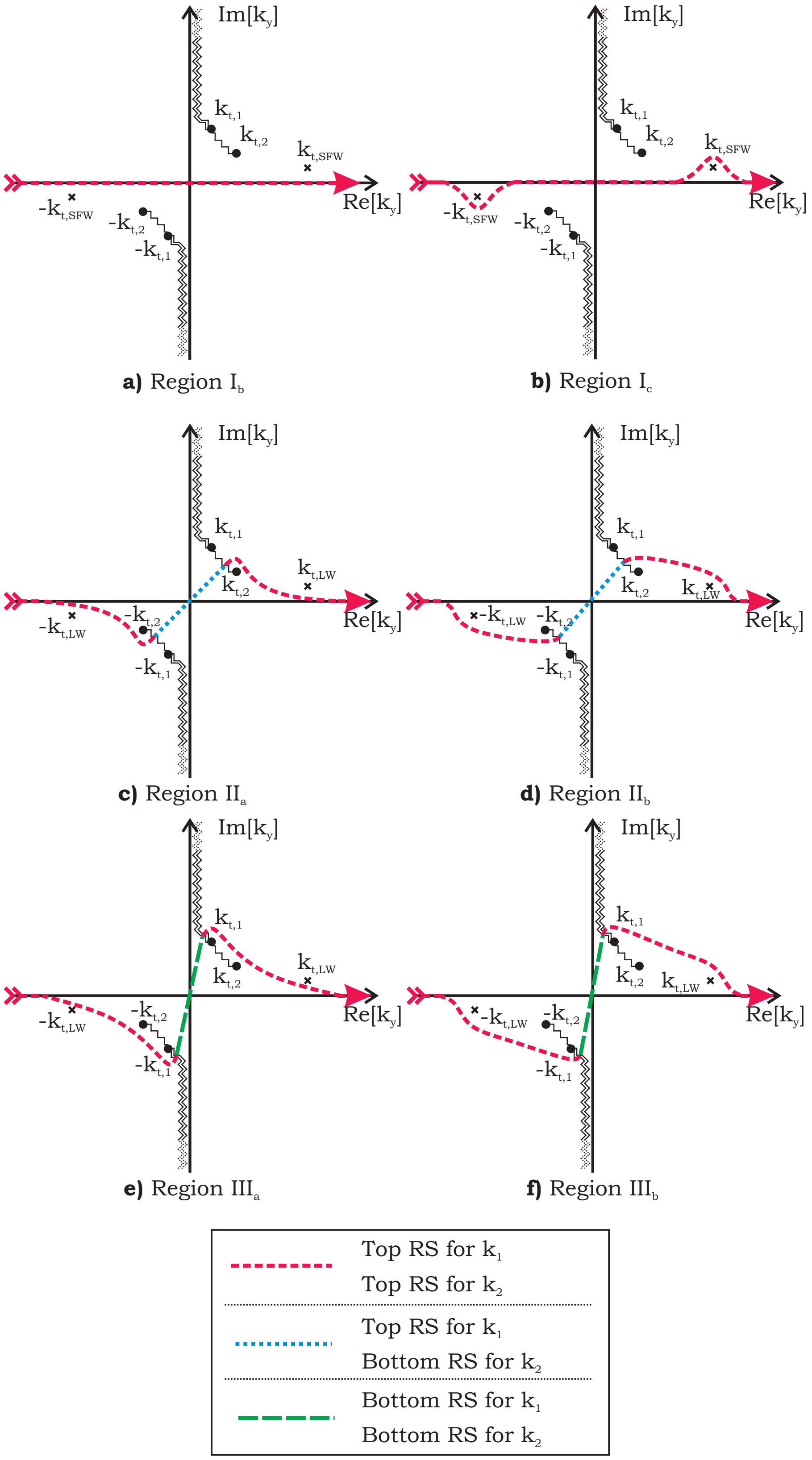

a) Region I_b **b)** Region I_c

c) Region II_a **d)** Region II_b

e) Region III_a **f)** Region III_b

Figure 3.11: Transverse spectral planes (k_y) and integration paths for the different regions in Figure 3.5, Figure 3.6 and Figure 3.7.

The explained integration paths shown in Figure 3.11a-f can be performed in a different, but equivalent manner. Looking at Figure 3.12a and referring to Cauchy's Integral Theorem we know that: $C_1 + C_2 + C_3 = 0 \rightarrow C_1 = -C_2 - C_3$. As a consequence of this equivalence, rather than integrating over C_1, we can integrate over the real axis on the top Riemann-sheet ($-C_3$) and subtract the integral between the branch-points (C_2). This is shown in Figure 3.12b. Subsequently, we have to integrate on the bottom Riemann-sheet between the branch-point. Enclosing either a surface-wave pole or leaky-wave pole as in Figure 3.11b,d,f can be done by adding the residual contributions of these poles. How this residual contribution is calculated is explained in Section D.2. So crossing the branch-cut with respect to k_2 as in Figure 3.11c,d is equivalent to integrating over the real axis, subtracting the contribution on the top Riemann-sheets between the branch-points and adding the contribution on the bottom Riemann-sheet of k_2 as is described in Eq. (3.40) and shown in Figure 3.12b.

$$\int_{II} \cdots dk_y = \int_{-\infty - top}^{\infty - top} \cdots dk_y + \int_{k_{t,2} - top}^{-k_{t,2} - top} \cdots dk_y + \int_{-k_{t,2} - bottom}^{k_{t,2} - bottom} \cdots dk_y \tag{3.40}$$

Similarly, crossing the branch-cuts with respect to both k_1 and k_2 as in Figure 3.11e,f is equivalent to the integration as is described in Eq. (3.41) and shown in Figure 3.12c.

$$\begin{aligned} \int_{III} \cdots dk_y = \int_{-\infty - top}^{\infty - top} \cdots dk_y + \int_{k_{t,1} - top}^{-k_{t,1} - top} \cdots dk_y + \int_{-k_{t,1} - bottom}^{k_{t,1} - bottom} \cdots dk_y \\ + \int_{k_{t,2} - top}^{-k_{t,2} - top} \cdots dk_y + \int_{-k_{t,2} - bottom}^{k_{t,2} - bottom} \cdots dk_y \end{aligned} \tag{3.41}$$

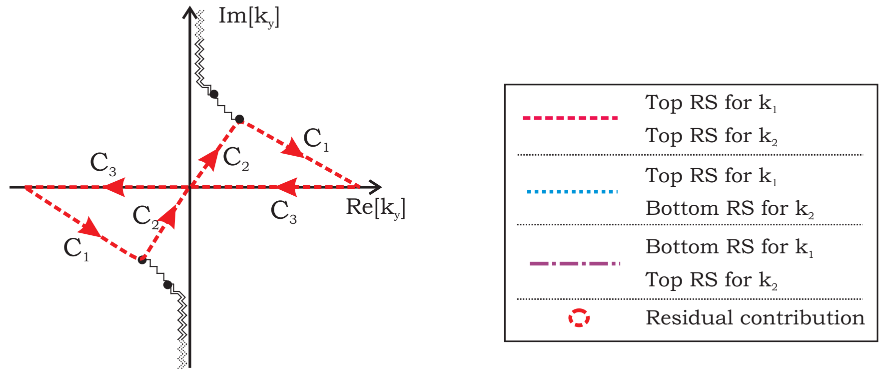

a) Cauchy's Integral Theorem on integration path

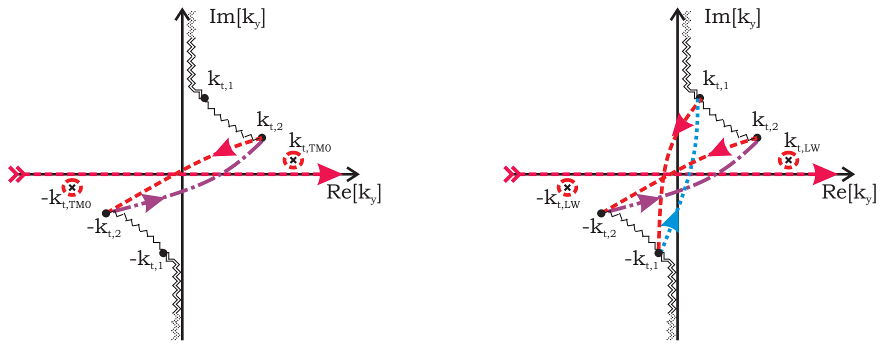

b) Equivalent integration path Region II **c)** Equivalent integration path Region III

Figure 3.12: a) Cauchy's Integral Theorem showing that $C_1 = -C_2 - C_3$; b) Equivalent integration path for Region II; c) Equivalent integration path for Region III.

3.3 Leaky- and surface-wave excitation in printed transmission lines

One of the significant advantages of using this quasi-analytical model is that losses due to radiation into space- and surface-waves can easily be investigated. When a stratification becomes large in terms of wavelength, these dynamic phenomena occur. When a transmission line is printed onto a dielectric slab, a surface-wave can be excited when the height of this dielectric slab exceeds an electrical length of approximately $\lambda_d/4$. Transmission lines fabricated with current printed circuit board technologies are limited in its dimension. Typical critical dimensions are 100 μm in width and 127 μm in height. For this reason, taking into account these surface-waves are of particular importance for printed transmission lines operating at high frequencies where the minimum dimensions of the transmission line are limited by the technology. Currently there are no (quasi-) analytical tool for estimating these radiation losses. There are some equivalent formulas for some basic coplanar transmission lines [11]. However, they do not account for transmission lines with arbitrary stratifications as in Figure 2.1.

The surface-wave and leaky-wave branch-points in the longitudinal spectral plane are intrinsic to the stratification in absence of the strip and slot as is discussed in Section 2.3. However, whether the dominant propagating mode along the transmission line is actually exciting these surface- and leaky-wave modes or not, will depend on the location of this dominant propagating mode with respect to the branch-point of the surface- or leaky-wave. We will refer to this as the surface-wave condition. This condition will be discussed in this section.

3.3.1 Surface-wave condition

The surface-wave condition is a condition for the main propagating mode along the transmission line to be exciting a surface-wave (leaky-wave). Radiation into a surface-wave (leaky-wave) happens with a specific angle of radiation, ψ. The surface-wave condition determines from what point this angle of radiation is non-imaginary. When ψ becomes real, the main propagating mode along the transmission line will be exciting the surface-wave (leaky-wave).

The propagation constant along the transmission line will be approximately the average of the propagation constant of the dielectrics above and below the transmission line; k_1 and k_2. This effective propagation constant will therefore be fast, seen from the dense dielectric point of view. Therefore, the propagating mode will leak into the denser dielectric. In Figure 3.13 we see the top view of coplanar stripes on top of a dielectric slab. The propagation constant of the surface-wave mode β_{SFW} is intrinsic to the stratification and does not depend on β_{mode}, or the presence of the strips. From Figure 3.13 we can see that the angle of radiation ψ is a function

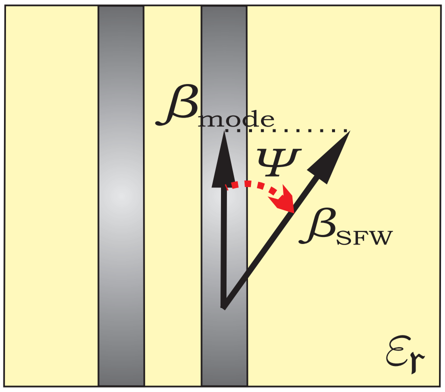

Figure 3.13: (x,y)-view of coplanar stripes on top of a dielectric slab, visualizing the surface-wave condition; ψ can only be real when $\beta_{mode} < \beta_{SFW}$. β_{SFW} is intrinsic to the stratification (2.20) and ψ is the angle of radiation.

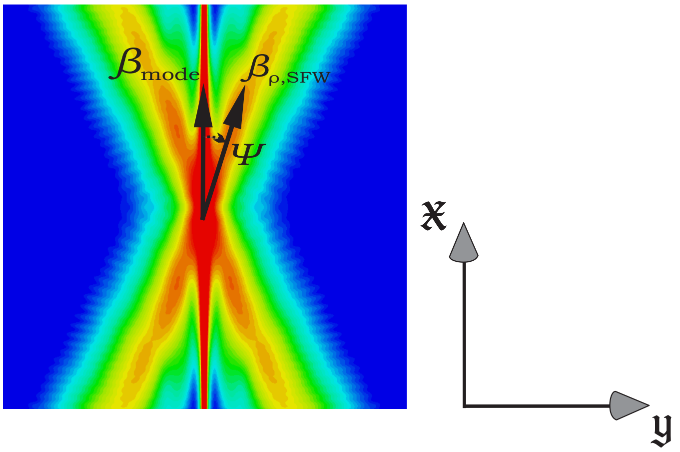

Figure 3.14: (x,y)-view of the power flow in the dielectric slab of a coplanar waveguide exciting a surface wave. β_{mode} is the propagation constant, $\beta_{\rho,SFW}$ is the surface-wave mode intrinsic to the stratification (2.20) and ψ is the angle of radiation into this surface-wave mode.

of the propagation constant of the propagating mode, β_{mode}, and the propagation constant of the intrinsic surface-wave mode β_{SFW}. The relation between these three components is as (3.42).

$$\cos(\psi) = \frac{\beta_{mode}}{\beta_{SFW}} \tag{3.42}$$

It can be seen that there can only be a real angle of radiation ψ when $\frac{\beta_{mode}}{\beta_{SFW}} < 1$. When this is not the case, ψ will be imaginary and no leakage into the surface-wave mode occur. From this equation, the condition for exciting a surface-wave can directly be seen [11]:

$$\beta_{mode} < \beta_{SFW} \tag{3.43}$$

This is the surface-wave condition as it is visualized in the spectral planes of Figure 3.6 and Figure 3.7. This condition is also true for exciting any leaky-waves. When this condition is fulfilled and k_{mode} is also on the correct Riemann-sheet with respect to $k_{LW/SFW}$, the surface- or leaky-wave is excited and $k_{LW/SFW}$ should be enclosed by the transverse integration path. A qualitative example is shown in Figure 3.14. In this figure, the absolute power flow can be seen in a dielectric slab beneath a coplanar waveguide. The propagating mode β_{mode} is smaller than β_{SFW} and therefore leaking into a surface-wave mode. An in magnitude decaying power flow can be seen along the coplanar line ($\hat{x}$) as well as the angle of radiation ψ into the surface-wave mode $\beta_{\rho,SWF}$.

3.3.2 Types of surface-waves

A printed transmission line can support three types of surface-waves.

- Transverse magnetic (TM) surface-waves
- Transverse electric (TE) surface-waves
- Transverse electromagnetic (TEM) surface-waves

A TEM-surface-wave is only supported by a parallel-plate-waveguide (PPW). In the developed software-too, we will therefore only find this mode in a grounded coplanar-waveguide. The tool is only able to account for the first surface-wave. A consequence is then, that dielectric slabs can be modeled until an electrical height of $\lambda_d/2$, where λ_d is the wavelength inside the dielectric. Larger slabs should be modeled as infinite dielectrics. The reasoning behind this choice is that, at this electrical height, the surface-wave losses are already comparable with the losses due to direct radiation into an infinite dielectric. This surface-wave loss approximation is explained and demonstrated in Section 4.4.

The first surface-waves appearing and accounted for in the software-tool, depending on the structure to analyze, are:

- **Strip** and **Coupled Stripes**: TE_0-surface-wave.
- **Microstrip** and **Coupled Microstrip**: TM_0-surface-wave (or otherwise TE_0-surface-wave when a higher dense dielectric slab is on top of the microstrips)
- **Stripline**: TM_0-surface-wave.
- **Slot** and **CPW**: TM_0-surface-wave.
- **Grounded CPW**: TEM-surface-wave and possibly a TM_0-surface-wave in the dielectric slab on top of the grounded CPW.

In Section 4.3 and Section 4.4 several examples will be given regarding the characterization of surface-wave and leaky-wave losses.

3.4 Impedance

An important aspect of antenna designers is to match the antennas to the transmission line in order to minimize any reflection losses. Therefore it is very useful to know the characteristic impedance of the transmission line. In this section, the model for calculating the characteristic impedance will be explained. We will see that the characteristic impedance in this quasi-analytical model is actually the impedance associated to the dominant propagating mode along the transmission line. This impedance is then basically equivalent to calculating the residue from the expression of the input-impedance seen from the Δ-Gap excitation. The goal of this section is to discuss our used definition of characteristic impedance and relate this to the input-impedance seen from the Δ-gap excitation. In Section 4.2 a comparison and validation of our definition will be given.

3.4.1 Input impedance

The transmission lines are excited with a delta-gap excitation as was shown in Figure 3.2 for both strip- and slot-type transmission lines. The longitudinal dimension of the delta-gap is defined as $\Delta = 0.7 \cdot w_s$. Starting from the magnetic- (electric-) current expressed as the inverse Fourier transform in Eq. (3.8), the input impedance (admittance) of this delta-gap for slot- (strip-) type transmission lines can be expressed as (3.44) [24].

$$Z_{in}^{Slot}/Y_{in}^{Strip} = \frac{1}{2\pi}\int_{-\infty}^{\infty} \frac{\mathrm{sinc}^2(\frac{k_x\Delta}{2})}{D(k_x)} dk_x \tag{3.44}$$

The integration path $-\infty < k_x < \infty$ requires to be deformed according to C_x shown in Figure 3.5, so that critical points in the spectrum such as branch-points and poles of propagation modes will be avoided. In order to calculate the input impedance (admittance) of a specific mode, the residue of this integral can be calculated in $k_x = k_{mode}$.

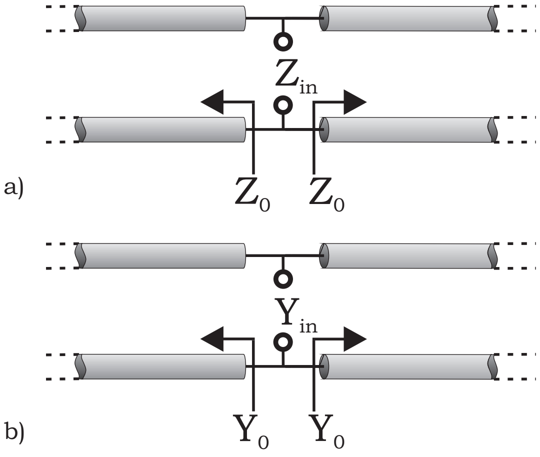

Figure 3.15: Definition for characteristic- and input-impedance for a) slot-type and b) strip-type transmission lines.

3.4.2 Characteristic impedance

The relation between the input impedance and characteristic impedance for slot-type and strip-type transmission lines is shown in Figure 3.15 and can be described as Eq. (3.45).

$$Z_0^{Slot} = 2 \cdot Z_{in}^{Slot} \quad \text{(3.45)a}$$

$$Y_0^{Strip} = 2 \cdot Y_{in}^{Strip} \quad \text{(3.45)b}$$

In [25] and [26] it is shown that the current parallel to the slot and voltage over the slot can be expressed as (3.46):

$$v_l(x) = -\frac{1}{2\pi} 2\pi j \frac{1}{D'(k_{mode})} e^{-jk_{mode}x} \quad \text{(3.46)a}$$

$$i_l(x) \approx \frac{1}{2} e^{-jk_{mode}x} \quad \text{(3.46)b}$$

And for strip-type transmission lines:

$$v_l(x) \approx \frac{1}{2} e^{-jk_{mode}x} \quad \text{(3.47)a}$$

$$i_l(x) = -\frac{1}{2\pi} 2\pi j \frac{1}{D'(k_{mode})} e^{-jk_{mode}x} \quad \text{(3.47)b}$$

By calculating the impedance as $Z_0 = \frac{v_l(x_0)}{i_l(x_0)}$, where x_0 is an arbitrary finite distance away from the near-field of the source, we obtain:

$$Z_0^{Slot} / Y_0^{Strip} = \frac{-2j}{D'(k_{mode})} \quad \text{(3.48)}$$

Note that these characteristic impedances are actually the residues of (3.44) without taking account of averaging the fields over the Δ-gap, which is leading to the $sinc^2$-term. (3.48) is therefore the characteristic impedance for one specific mode which is propagating along the transmission line. A more rigorous derivation of this definition of the characteristic impedance (3.48) can be found in [27]. The characteristic impedance implemented in the software-tool calculates the characteristic impedance in this manner and will in some cases differ from the input impedance seen from the delta-gap excitation as will be seen in the example in Section 4.2.

3.5 Ohmic losses

Ohmic losses in a printed transmission line not only comprises conductor losses but also dielectric losses. This section will cover the implementation of both of them.

Firstly the implementation of dielectric losses will be discussed. This will be a brief discussion as it turns out that a loss tangent can easily be converted to a complex relative permittivity.

Subsequently, we will discuss conductor losses. Conventionally, conductor losses are calculated in various ways [28–32]. Quasi-analytical techniques can be used such as Wheeler's incremental inductance rule, but also full-wave analysis based on spectral domain approaches. In this proposed quasi-analytical model, it turns out that the ground-planes of strip-type transmission lines and the ground-plane of a grounded CPW can be characterized by the square-root of frequency surface-impedance connected to the transmission lines representing the dielectric slab. For conductor losses in the strip itself, a new dispersion equation can be constructed taking account of the non-zero tangential total electric field component, $\underline{e}_{tot}(x,y)$ in (3.1), which can also characterized as a function of the surface impedance. A more rigorous derivation of the new dispersion equation can be found in Appendix B. For slot-type transmission lines, the losses will be implemented in the Green's functions.

3.5.1 Dielectric losses

Printed transmission lines can suffer from dielectric losses. These losses can be defined in the tool by means of a dielectric loss tangent $\tan(\delta)$. This loss tangent is implemented in the Green's functions with a complex dielectric permittivity (3.49).

$$\varepsilon_{lossy} = \varepsilon_0 \varepsilon_r (1 - j \tan(\delta)) \tag{3.49}$$

Using ε_{lossy}, instead of $\varepsilon_0\varepsilon_r$, directly in the Green's function when defining your stratifications (2.9) will characterize dielectric losses accurately as will be shown in Section 4.5.

Referring back to the discussion of the branch-cuts associated to the branch-points of the infinite media k_i in subsection 3.2.2, please note that the square-root type branch-cut coming from $k_{z,i} = \sqrt{k_i^2 - k_\rho^2}$ now becomes complex since k_i will become complex. For example, when the infinite media k_1 and k_2 in Figure 3.5 have the same non-zero loss tangent, the spectrum

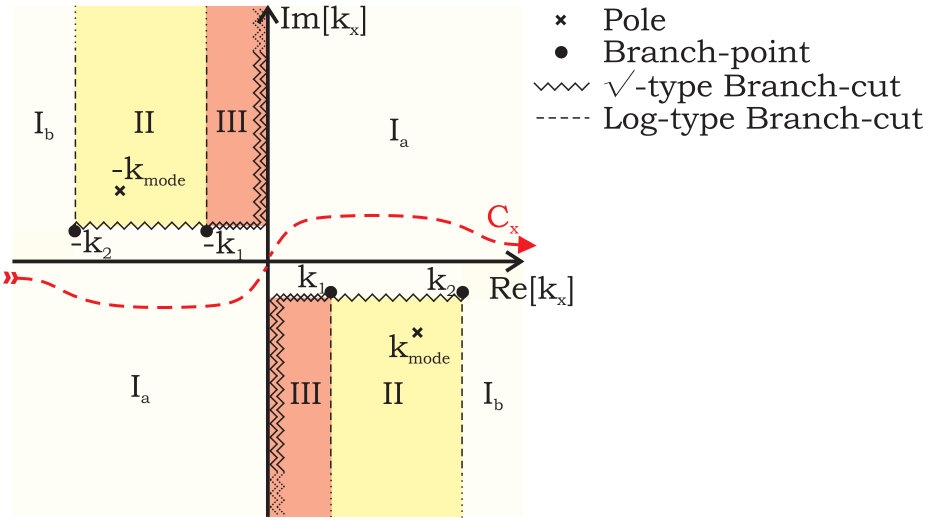

Figure 3.16: Longitudinal spectral plane (k_x) for a CPW printed between two lossy infinite dielectrics.

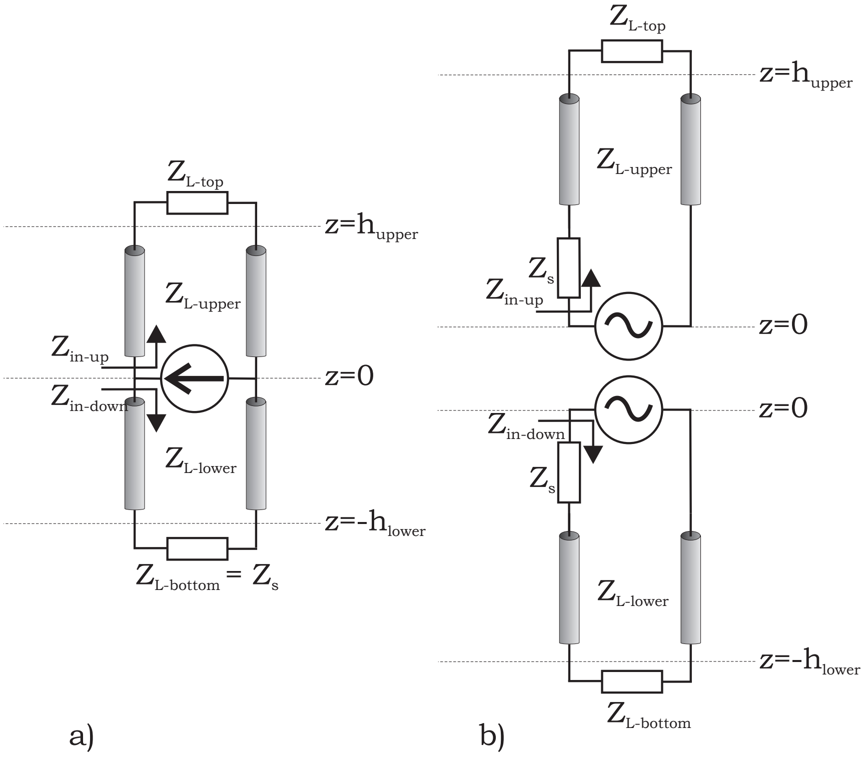

Figure 3.17: Equivalent transmission line models for a) a lossy microstrip and b) a lossy slotline.

will look like Figure 3.16. Additionally, any intrinsic surface-wave poles supported by the stratification (k_{SFW} in Figure 3.6) will now become complex.

3.5.2 Conductor losses

Besides dielectric losses, we need to take account of the conductor losses of a printed transmission lines. Conductor losses in ground-planes for both slot-type (e.g. grounded-CPW) and strip-type (e.g. microstrip, stripline) transmission lines can easily be implemented in the Green's functions; rather than applying a short-circuit to the transmission line representing the grounded slab, one can connect a load to the transmission line. This load can be characterized by the high-frequency surface impedance Eq. (3.50):

$$Z_s = (1+j)\sqrt{\frac{k_0\zeta_0}{2\sigma}} \tag{3.50}$$

where k_0 and ζ_0 are the free-space wavenumber and impedance respectively and σ is the conductivity of the conductor. An example is given in Figure 3.17a) where the ground-plane of a lossy microstrip is represented by the bottom load $Z_{L-bottom}$. $Z_{L-bottom}$ is now equal to the surface impedance Z_s rather than a short-circuit used for PEC.

The conductor losses for the main conductor of a strip-type transmission line are accounted for by means of a surface impedance boundary condition. Imposing the EFIE on a lossy conductor gives rise to a non-zero tangential total electric field ($\underline{e}_{tot}$) contribution; $\underline{e}_{scatt} = -\underline{\boldsymbol{m}}_{\Delta} + \underline{e}_{tot}$ (3.1). The total electric field $\underline{e}_{tot}$ can be related to the strip's surface impedance and current along the line as is described in Eq. (3.51).

$$\underline{e}_{tot}(x,y) = Z_{strip}(y)\underline{\boldsymbol{j}}_{eq}(x,y) \tag{3.51}$$

It makes sense to define Z_{strip} with the square-root of frequency surface impedance Z_s (3.50). However, this constant surface impedance does not really make sense when looking at the shape of the transverse fields in (3.1). The scattered electric field ($\underline{\boldsymbol{e}}_{scatt}$) and the Δ-gap excitation ($\underline{\boldsymbol{m}}_{\Delta}$) will have a rectangular shape. The total electric field is given by (3.51). When Z_{strip} is assumed to be constant, the multiplication with the equivalent electric current $\underline{\boldsymbol{j}}_{eq}$ will result in an electric field in the form of the quasi-static edge singularity function $j_t(y)$ (3.7). Therefore, it makes more sense to define Z_{strip} proportional to the inverse of the quasi-static edge singularity function as is shown in (3.52) and demonstrated in [18].

$$Z_{strip} = Z_s\sqrt{1-\left(\frac{2y}{w_s}\right)^2} \tag{3.52}$$

Accounting for the ohmic losses in the metal leads to a new denominator for the strip (3.53), where $\underline{\underline{I}}$ is the identity matrix. A more rigorous derivation of this result can be found in Appendix B.

$$\underline{\underline{D}}_{loss}(\underline{k}_x) = \underline{\underline{D}}(\underline{k}_x) + \frac{2}{w_s\pi}Z_s\underline{\underline{I}} \tag{3.53}$$

For slot-type transmission lines, since the IE is different, the conductor losses can be calculated by following the approach proposed in [33]. The approach is based on applying the equivalence principle on the slot region by replacing the region with the same lossy conductor as the ground planes. The lossy conductor can then be implemented in the transmission-line Green's functions by means of an impedance, characterized by Z_s in series with the stratifications as is shown in Figure 3.17b. However, applying the equivalence principle with a lossy metal, results in a small, but non-zero, equivalent electric current, j_{eq}. The quasi-analytical model implemented in the MATLAB-tool is neglecting this contribution, as is shown in Figure 3.18a, by only solving the dispersion equation for m_{eq}. An alternative method is described in [33, 34] which is, although not implemented, based on defining an effective magnetic current, m_e, taking into account the equivalent electric current as is shown in Figure 3.18b, and described by Eq. (3.54).

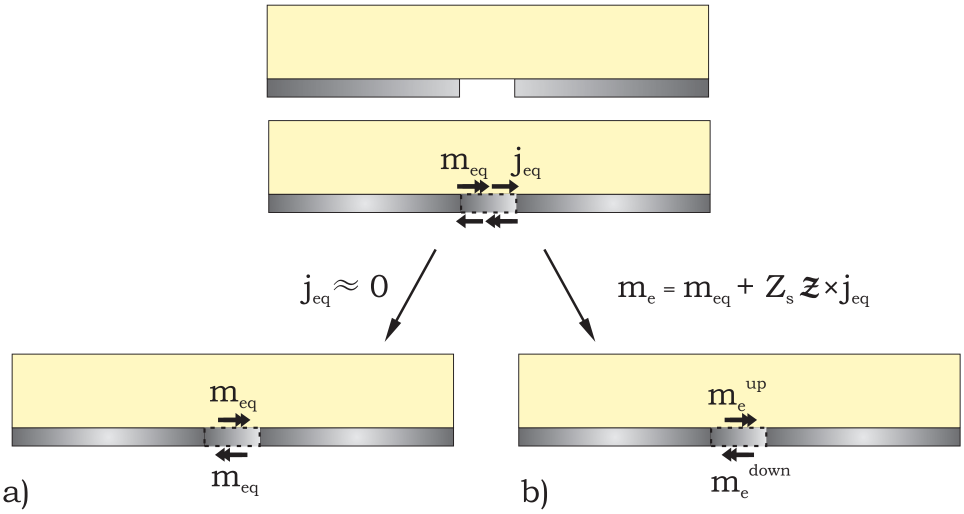

Figure 3.18: Equivalence principle on the slot region. a) Tangential equivalent electric current is neglected $j_{eq} = 0$ b) An effective equivalent magnetic current is defined the identity $m_e = m_{eq} + Z_s\hat{z} \times j_{eq}$

$$m_e = m_{eq} + Z_s \hat{z} \times j_{eq} \tag{3.54}$$

Using Eq. (3.54), will allow for solving the dispersion equation for one unknown, but with taking account of the electric current. It will result in an extra coupling term in the integral equation. However, as will not be explained in this thesis, other problems will come along when applying this approach.

3.6 Superconductivity

Besides the ohmic losses of a conductor, also the superconductive phenomenon is implemented, making the tool suitable for characterizing more complex structures such as the transmission lines (resonators) in Kinetic Inductance Detectors (KIDs) which are widely used in the THz-domain for space-applications. The total current flowing on the superconductor is the superposition of a current exhibiting normal losses and a loss-less superconductive current. This assumption is referred to as the two fluid model [35]. The superconductors can be characterized via a complex conductivity (3.55) [36].

$$\sigma = \sigma_1 + j\sigma_2 \tag{3.55}$$

The real part of the complex conductivity σ_1 represents the normal fluid conductivity while the imaginary part σ_2 represents the super fluid conductivity. The complex conductivity is introduced in Z_s as is studied in [37]. The surface impedance Z_s used for the impedance boundary condition for a superconductor at low temperature ($\sigma_1 \ll \sigma_2$) can be characterized by Eq. (3.56):

$$Z_s = R_s + jX_s \tag{3.56}$$

In (3.56), the surface resistance, R_s, and the surface reactance, X_s, can be calculated by Eq. (3.57):

$$\begin{aligned} R_s &= \frac{1}{\lambda_L}\frac{\sigma_1}{2\sigma_2^2} && \text{(3.57)a} \\ X_s &= \omega\mu_0\lambda_L = \omega L_s && \text{(3.57)b} \end{aligned}$$

In Eq. (3.57), λ_L is the London penetration depth which is related to σ_2 by Eq. (3.58).

$$\lambda_L = \frac{1}{\sqrt{\mu_0 \sigma_2 \omega}} \tag{3.58}$$

In the software tool, the surface impedance can be given by providing a value for the sheet inductance L_s and the real part of the conductivity. Z_s in (3.56) can then be used in exact the same way as is discussed in Section 3.5. In Section 4.6 we will see that superconductive materials can have a significant effect on the propagation constant and characteristic impedance of a transmission line. A change in propagation constant also will have its effect on the amount of possible radiative losses. As said before, there are no equivalent formulas to estimate these effect; one has to resort to full-wave simulations.

Chapter 4

Transmission line examples and validation

Using the quasi-analytical model described in chapter 3, numerous interesting characteristics of printed transmission lines can be analyzed. The model is used to generate a software tool which is made freely accessible and capable of analyzing the most widely used transmission lines. The user can select the materials and loss tangents of four possible stratifications; two finite dielectric slabs and two infinite media. The stratifications are assumed to be homogeneous in the transverse plane. A conductivity and loss tangent will account for the ohmic and dielectric losses in the structure. The graphical user interface can be downloaded at http://terahertz.tudelft.nl/. The output of the tool is composed out of four figures:

- The complex normalized wavenumber
- The effective dielectric constant
- The characteristic impedance
- Losses

This section will show examples, validation and a discussion of these transmission line characteristics calculated by the discussed quasi-analytical model. The structures mainly used for this validation are shown in Figure 4.1. The transverse dimensions, w_s and d, are often chosen to be the minimum transverse dimension typically possible for printed circuit board technology; i.e. 100 μm. The minimum height of the dielectric slabs will be considered as 127 μm. The conductor thickness is infinitesimal and the CPW is excited with a delta-gap excitation in differential (propagating) mode as is described in Section 3.1.

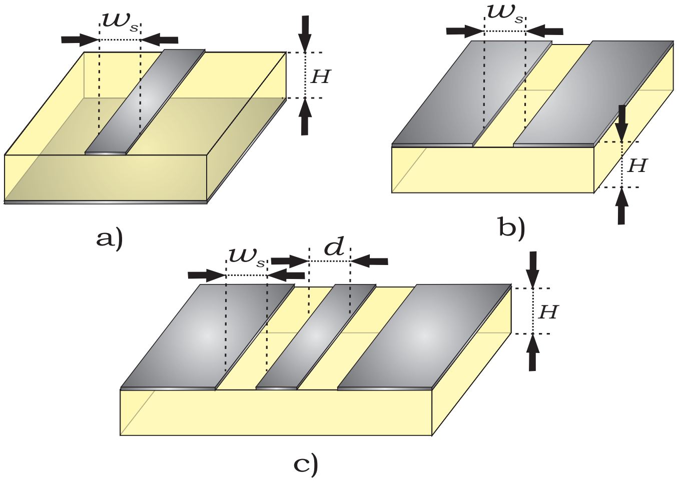

Figure 4.1: Transmission lines used for validation. a) Microstrip, b) Slotline, c) Coplanar Waveguide (CPW); w_s is the width of the strip/slot, d is the width of the main conductor for a CPW and H is the height of the substrate.

4.1 Complex normalized wavenumber

The complex normalized wavenumber k/k_0, with $k = \beta - j\alpha$ and k_0 the free-space wavenumber, gives information regarding the dispersion of the transmission line and the losses associated to it. The real part of the wavenumber, β, allows for calculating the effective dielectric constant of the transmission line (4.1).

$$\varepsilon_{r,eff} = \left(\frac{\beta}{\beta_0}\right)^2 \tag{4.1}$$

The imaginary part of the wavenumber, α is the superposition of all attenuative contributions. These contributions can be conductor-, dielectric- and radiation losses. The attenuation constant α, in Nepers, can then be converted to a loss figure; e.g. in dB/λ_{eff}, where λ_{eff} is the effective wavelength of the propagating mode (4.2). Losses, in terms of radiation and ohmic-losses will be validated later on in this chapter.

$$\lambda_{eff} = \frac{c}{f\sqrt{\varepsilon_{r,eff}}} = \frac{\lambda_0}{\sqrt{\varepsilon_{r,eff}}} \tag{4.2}$$

Complex normalized wavenumber for a microstrip and CPW

In Figure 4.2, the real part of the complex normalized wavenumber, (β/β_0), for a microstrip (Figure 4.1a) with $w_s = 100\mu$m, $H = 127\mu$m, $\varepsilon_r = 11.9$ and a CPW (Figure 4.1c) with $w_s = 100\mu$m, $d = 100\mu$m, $H = \infty$ and $\varepsilon_r = 11.9$ is shown. The presented results are validated with full-wave simulations done in CST where the main line parameters are extracted from the field distribution along the strip and slots. It is clear that the quasi-analytical model implemented in the software-tool can easily analyze transmission lines over a wide frequency range (a decade in this case) to show the dispersive behavior of such line.

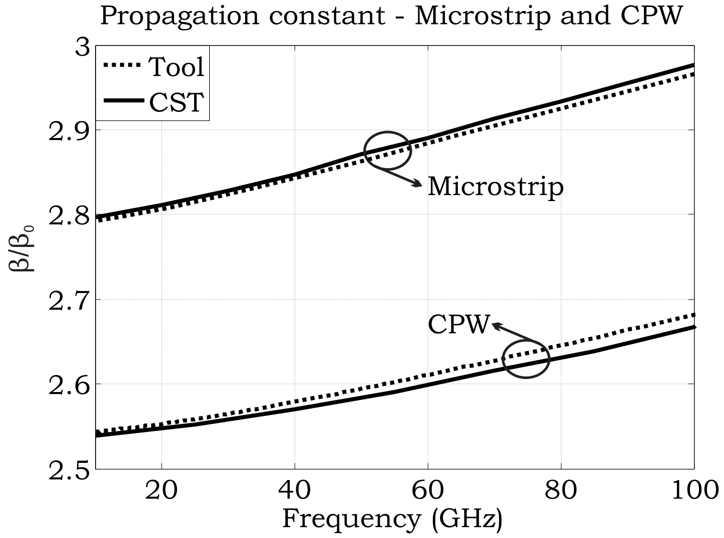

Figure 4.2: Real part (β/β_0) of the complex normalized wavenumber for a microstrip (Figure 4.1a) with $w_s = 100\mu$m, $H = 127\mu$m, $\varepsilon_r = 11.9$ and a CPW (Figure 4.1c) with $w_s = 100\mu$m, $d = 100\mu$m, $H = \infty$ and $\varepsilon_r = 11.9$. The result is validated with full-wave CST simulations.

4.2 Characteristic impedance

In this section we will validate the characteristic impedance calculated by the quasi-analytic model. The procedure was explained in Section 3.4 and resulted in:

$$Z_0^{Slot}/Y_0^{Strip} = \frac{-2j}{D'(k_{mode})}$$

This characteristic impedance (admittance) is derived from the current en voltage distributions along the slot (strip) and is only representing the contribution due to this one specific mode k_{mode}. It was explained that this impedance can change from calculating the impedance from the input-impedance seen from the Δ-gap excitation. This will be shown in this section. Also we will show that calculating the characteristic impedance with (3.48) close by singularities in the spectral plane (i.e. branch-points and -cuts) can give rise to (big) differences with the input-impedance. The reason for this difference is due to the fact that the Δ-gap excitation leaks a significant amount of power in these singularities simultaneously.

4.2.1 Impedance for a slotline and microstrip

The characteristic impedance calculated from (3.48) is compared with the impedance seen from the Δ-gap excitation; the input impedance (3.44). This is done for the microstrip (Figure 4.1a, with $w_s = 100\mu$m, $H = 127\mu$m and $\varepsilon_r = 11.9$) and a slotline printed in between two infinite media (Figure 4.1b, with $w_s = 100\mu$m, $H = \infty$ and $\varepsilon_r = 11.9$). In this comparison, (3.45) is used to convert the input-impedance found from (3.44) to a characteristic impedance (see also Figure 3.15). This comparison is shown in in Figure 4.3 and Figure 4.4 for the slotline and microstrip respectively.

For as well the microstrip as the slotline, both procedures give approximately the same real part of the characteristic impedance. However, for the imaginary part of the microstrip a difference can be seen between the two procedures; as the main propagating mode of a microstrip is purely real, the characteristic impedance obtained by (3.48) is also purely real. Remember that the characteristic impedance calculated is the impedance associated to the dominant propagating mode along the transmission line. In contrast, (3.44) calculates the total input-impedance of the delta-gap including the reactance of the port, resulting in an imaginary part of the impedance.

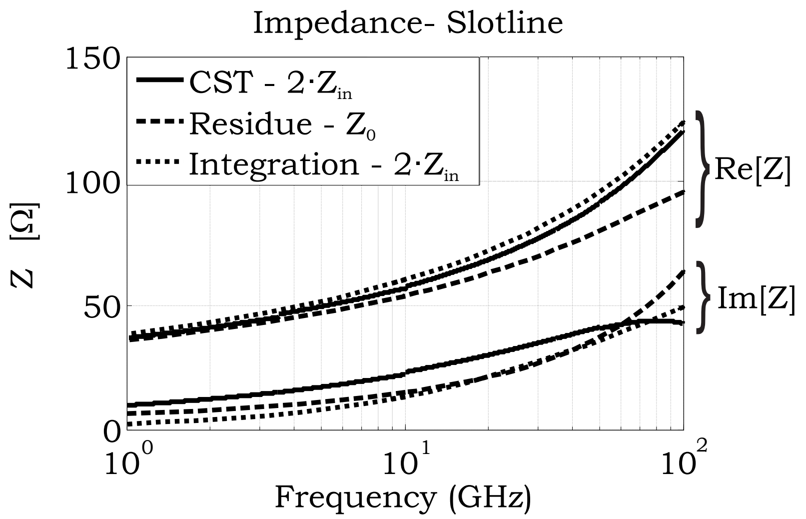

Figure 4.3: Characteristic impedance for the slotline (Figure 4.1b) with $w_s = 100\mu$m, $d = 100\mu$m, $H = \infty$ and $\varepsilon_r = 11.9$. *Residue* is calculated from (3.48) and *Integration* from (3.44) and (3.45)

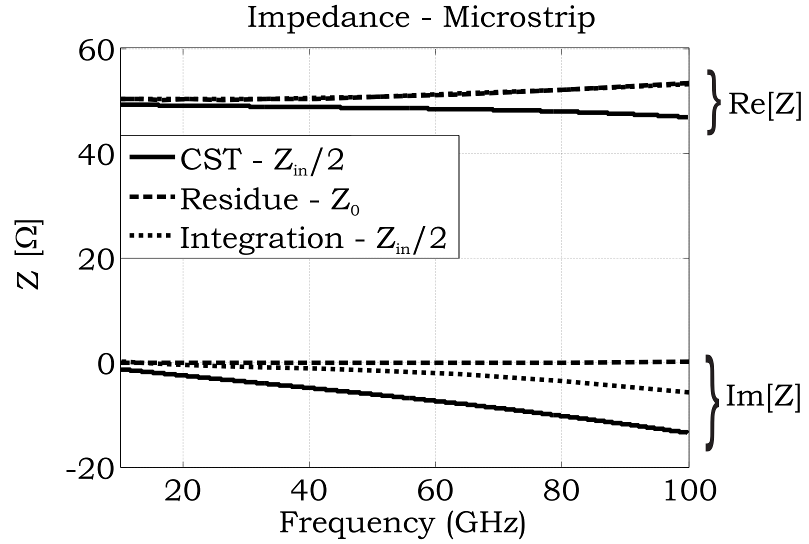

Figure 4.4: Characteristic impedance for a microstrip (Figure 4.1a) with $w_s = 100\mu$m, $H = 127\mu$m and $\varepsilon_r = 11.9$. *Residue* is calculated from (3.48) and *Integration* from (3.44) and (3.45)

This total input-impedance therefore can also cover space-wave excitation by the Δ-gap. The impedances are validated with a full-wave CST simulation where Z_{in} was extracted from the Z_{11}-parameter of the Δ-gap excitation port.

In the following section, we will see that when the dominant propagating mode is close-by a branch-point or -cut, the characteristic impedance calculated by (3.48) can differ significantly from the input impedance.

4.2.2 Impedance nearby spectrum singularities

A slotline is in fact not actually a transmission line; it can be highly radiative in the presence of infinite media. The impedance comparison for the slotline in Figure 4.3 was still fairly good until higher frequencies ($f < 100$ GHz). However, when this highly radiative mode is close to other singularities in the spectrum, such as branch-points and -cuts associated to leaky-waves or space-waves, we will see that also these singularities are excited by the Δ-gap excitation.

In Section 4.3 we will discuss a slotline in the presence of an infinite dielectric. This dielectric medium however, is separated by an air-gap of 100μm, decreasing the propagation constant to (and even below) k_0. The propagation constant of such slotline is given in Figure 4.10. It can be seen that k_{mode} is now close by a branch-point and -cut associated to the k_{TM0} leaky-wave. Since $k_{mode} \approx k_0$, it is also close by the branch-point of the infinite medium k_0. Comparing in this case the characteristic impedance with the input impedance seen from the Δ-gap excitation results in Figure 4.5. Although the real part of the characteristic impedance of the main propagating mode, k_{mode}, in Figure 4.5 compares fairly good with the input impedance calculated from (3.44) and (3.45), we can see big differences in the imaginary part of the impedance. The reason for this is that not only the highly radiative slotline mode is excited by the Δ-gap excitation, but there is also power excited in the space-wave (k_0 branch-point) and the leaky-wave (k_{TM0} branch-point).

When, instead of a slotline, a CPW (with $w_s = 100\mu$m and $d = 100\mu$m) is excited in the same stratification, we know that the fields of the dominant propagating mode is now more confined to the transmission line itself; it is less radiative. This can also be seen in the impedance comparison as is shown in Figure 4.6. Since the main propagating mode is now less radiative

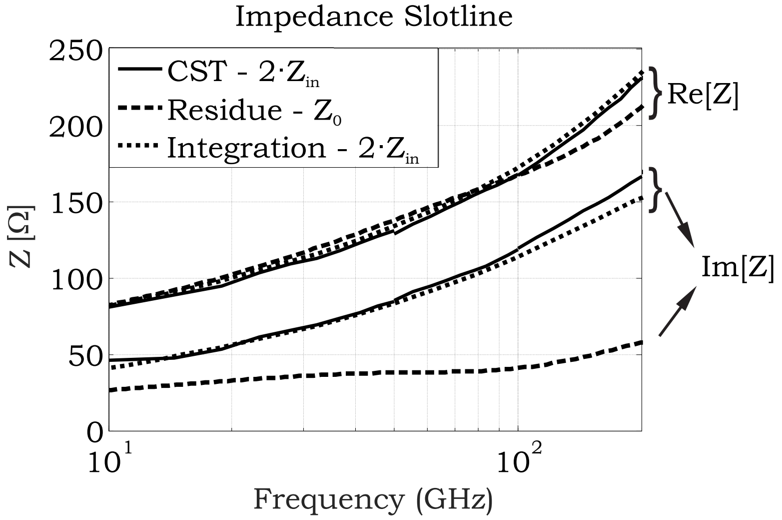

Figure 4.5: Characteristic impedance for a slotline with $w_s = 100\mu$m, beneath an infinite dielectric with $\varepsilon_r = 11.9$, separated by an air-gap of $H = 100\mu$m. *Residue* is calculated from (3.48) and *Integration* from (3.44) and (3.45)

it can be seen that the parallel excitation of the leaky- and space-wave is less significant. k_{mode} will still be close by the branch-points so differences in the characteristic- and input-impedance, especially at higher frequencies ($f > 100$ GHz), can still be seen.

Concluding we can say that care have to be taken in analyzing the characteristic impedance calculated by the quasi-analytical model (3.48). As said, this impedance is purely the contribution of the main propagating mode. As we have seen now, in the case when this main-propagating mode is highly radiative and close-by any other singularities in the spectral plane, the Δ-gap excitation also leaks power into these singularities (e.g. space- or leaky-waves), resulting in a significant difference between input impedance and characteristic impedance of the dominant mode.

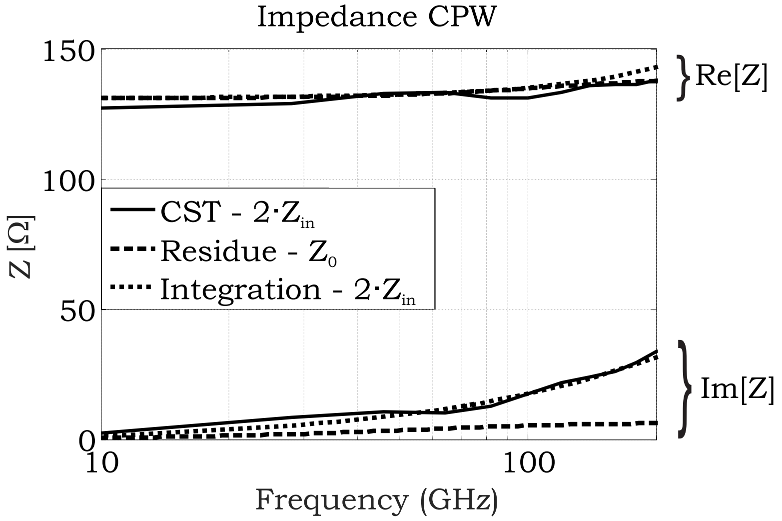

Figure 4.6: Characteristic impedance for a CPW with $w_s = 100\mu$m, $d = 100\mu$m beneath an infinite dielectric with $\varepsilon_r = 11.9$, separated by an air-gap of $H = 100\mu$m. *Residue* is calculated from (3.48) and *Integration* from (3.44) and (3.45)

4.3 Radiation into leaky- and surface-waves

In this section some examples are given of the characterization of printed transmission lines at high frequencies in terms of surface- and leaky-wave excitation. We will investigate the excitation of leaky- and surface-waves in two situations:

- A microstrip at high frequencies
- A slotline in the presence of an infinite dielectric, separated by an air-gap

It is known that the dominant mode of a microstrip does not become leaky unless anisotropic substrates are used. However, as we will see, this bounded mode of a microstrip actually disappears when the branch-point of the TM_0-surface-wave is converging to k_d. In this case, only higher-order leaky modes will be present in the structure.

A slotline (and CPW) in the presence of an infinite dielectric, separated by an air-gap, is a structure that can be used as an antenna (or transmission line) part of a leaky lens structure as is shown in [38, 39]. In this structure we will not see multiple modes propagating. However, as will be seen, the leaky-wave mode (subsection 2.3.2) is present in the spectrum. Although the leaky-wave mode is not excited, we will see that the normalized propagation constant of the propagating mode along the line can become lower than 1; $\beta_{mode} < \beta_0$. In this section we also discuss a problem of the quasi-analytical model used. The problem lies in the transitions between the Riemann-sheets for $\beta_{mode} > \beta_0$ and $\beta_{mode} < \beta_0$ which is giving discontinuities in the propagating modes. This transition is then more carefully studied by means of a CST validation. It turns out that indeed a transition will be made from one Riemann-sheet to another. However, from the CST simulation we see that this transition happens smoothly. We conclude that there is a need for a transition function in the quasi-analytical model.

4.3.1 Microstrip at high frequencies

For microstrip transmission lines printed on a isotropic substrate it is known that the conventional bounded propagation mode will never evolve into a leaky surface-wave mode [12] as we will show for a CPW and slotline in Section 4.4. However, higher order modes can occur when the frequency increases. Also, these higher modes can become significant in terms of excitation comparing to the bounded mode. In order to investigate these modes, consider the microstrip shown in Figure 4.1a with $w_s = 50\mu$m, $H = 500\mu$m and $\varepsilon_r = 10.2$ over a frequency range of

$$20\text{GHz} < f < 130\text{GHz}$$

resulting in an electrical height of the dielectric slab of

$$0.11\lambda_d < H < 0.69\lambda_d$$

The surface-waves and propagating modes for the specified frequency range are shown in Figure 4.7. Mode A is obtained by integrating only over the real axis (Figure 3.11a); it shows the conventional bounded microstrip mode. Mode B is extracted from the dispersion equation by including the TM_0-surface-wave in the transverse integration path (Figure 3.11b); it is therefore only valid when $k_{TE_1} < k_B < k_{TM_0}$, i.e. when the surface-wave condition (3.26) [11] is verified with respect to the k_{TM_0}-surface-wave. When the transverse integration path also encloses the TE_1-surface-wave, the third mode, C, is obtained. As both surface-wave poles are enclosed, this pole is only valid when $k_C < k_{TE_1} < k_{TM_0}$.

In Figure 4.8, the current spectra are shown at the frequencies of 20 GHz, 50 GHz, 90 GHz and 130 GHz. For an explanation about the different regions, branch-points and -cuts please

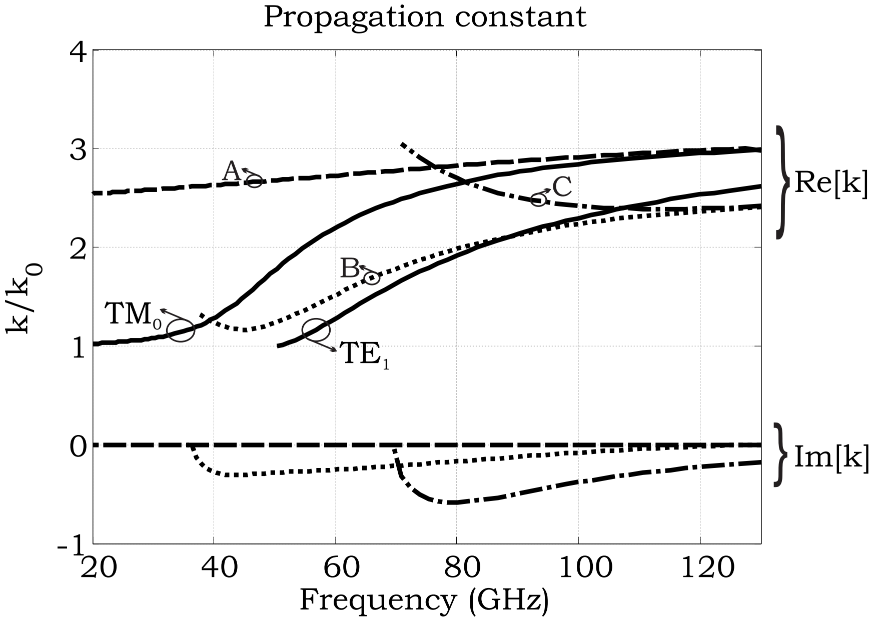

Figure 4.7: TM_0- and TE_1-surface-waves and propagating modes for the microstrip shown in Figure 4.1a with $w_s = 50\mu\text{m}$, $H = 500\mu\text{m}$, $\varepsilon_r = 10.2$.

refer to Figure 3.6 and its associated explanation. The spectra in Figure 4.8 will be used to explain four important regions which can be extracted from Figure 4.7:

1. $f \leq 40$ GHz; one mode (A) is propagating. This is the conventional microstrip-mode and will be strictly real; no surface-wave will be excited (see Figure 4.8 at 20 GHz).
2. 40 GHz $< f <$ 90 GHz; the first mode (A) is still completely real. However, as can been seen in Figure 4.8) at 50 GHz, a second mode, B, will excite the TM_0-surface-wave since $k_B < k_{TM_0}$.
3. 90 GHz $< f <$ 110 GHz; this region is interesting since mode B is not physically valid anymore (i.e. when $k_{TE_1} < k_B < k_{TM_0}$). As can be seen in the spectrum at 90 GHz, the second mode, B, will cross the k_{TE_1} boundary and disappears in the spectrum. Only the first mode, A, is propagating in this frequency range and is purely real. This may also be related to the transitions in the spectral plane as will be explained in subsection 4.3.2.
4. 110 GHz $< f <$ 130 GHz; from $f =$ 110 GHz, a third mode, C, will excite the TE_1-surface-wave. In the current spectrum at 130 GHz, it can also be seen that the first mode A is merging with the k_{TM_0}-surface-wave-pole as the frequency is increasing; mode C will be the main propagating mode in the microstrip.

This example shows the extreme dynamic behavior of a microstrip at high frequencies when the dimensions of the slab become significant in terms of wavelength. The analysis of multiple modes, other than just the dominant propagating mode, is not implemented in the MATLAB-tool because of the complexity of finding and tracking these modes. However, in Section 4.4 we will investigate the significance of the higher-order modes and we will come to a conclusion that dielectric slabs with $H > 0.5\lambda_d$ should be modeled as an infinite dielectric.

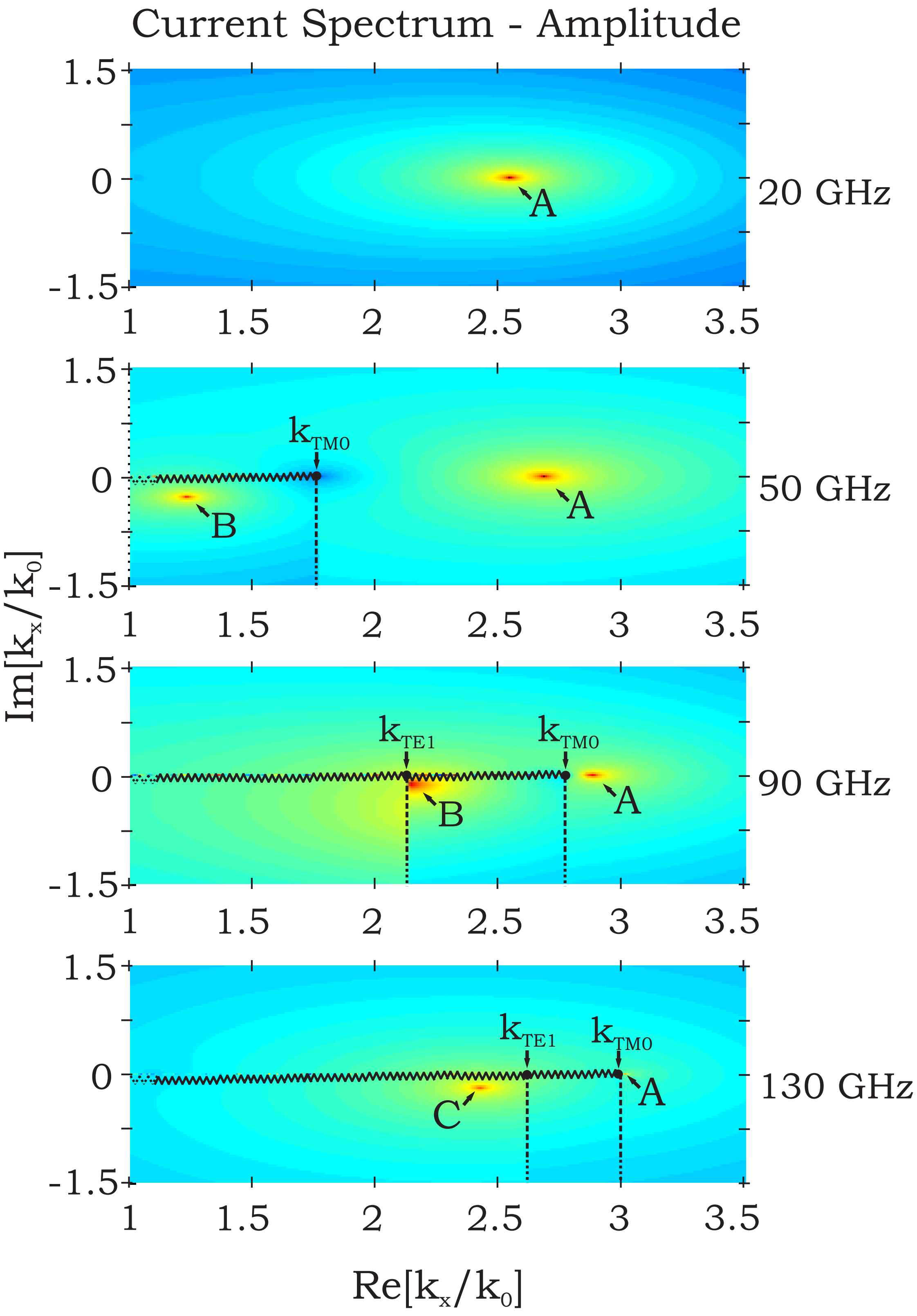

Figure 4.8: Current spectra for the microstrip in Figure 4.1a with $w_s = 50\mu$m, $H = 500\mu$m, $\varepsilon_r = 10.2$ at 20 GHz, 50 GHz, 90 GHz and 130 GHz. The branch-cuts due to the TM_0- and TE_1-surface wave are shown and the different propagating modes from Figure 4.7 are highlighted.

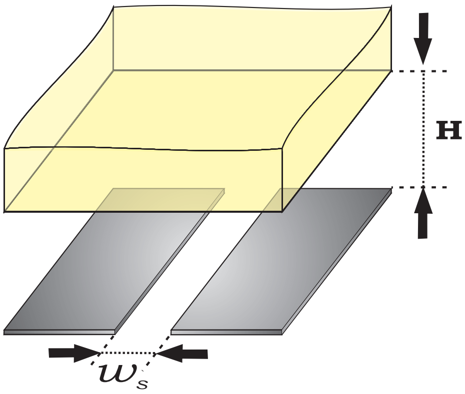

Figure 4.9: Slot $w_s = 100\mu$m in the presence an infinite dielectric with $\varepsilon_r = 11.9$ with an air-gap of $H = 100\mu$m.

4.3.2 Slotline in the presence of an infinite medium

In this subsection, a slotline in the presence of an infinite dielectric will be investigated. The structure is shown in Figure 4.9, with a grounded air-gap of 100 μm below an infinite silicon medium, simulating a dielectric lens with $\varepsilon_r = 11.9$. The first leaky-wave appearing in this structure is the TM_0-leaky-wave with a cutoff frequency of $k_c = 0$. This first leaky-wave and the main propagating mode are shown in Figure 4.10. Remember that the leaky-wave is intrinsic to the stratification and does not depend on the slotline. We can see that the propagating mode is always very close to the leaky-wave mode. Despite of the fact the surface-wave condition ($\beta_{mode} < \beta_{LW}$) is verified, the propagating mode is still on the top-Riemann sheet with respect to the leaky-wave mode ($Im[k_{mode}] > Im[k_{LW}]$); referring to Figure 3.7, the propagating mode is located in region II$_a$. This means that the leaky-wave is not excited. In other words, k_{mode} is directly radiating into the infinite medium. This can also be seen when looking at the current spectra as is shown in Figure 4.11 for 30 GHz, 100 GHz and 300 GHz. When the propagating mode is obtained by following the integration path associated to spectral region II$_a$ we obtain Figure 4.10 and the subfigures a) to c) in Figure 4.11. We know that when $\beta_{mode} < \beta_0$, the integration path associated to spectral region III$_a$ should be used, however in that case we have the spectral plane in d) instead of c) at 300 GHz. It is clear that not a single mode is mathematically valid between 155 GHz and 300 GHz. A transition is observed from Riemann-sheet to Riemann-sheet resulting in a discontinuity of modes. This will be explained in the following subsection.

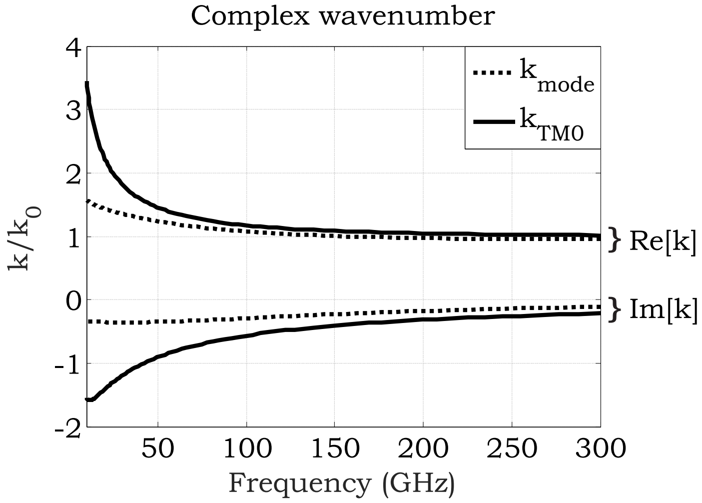

Figure 4.10: TM_0- leaky-wave and propagating mode k_{mode} for the structure in Figure 4.9

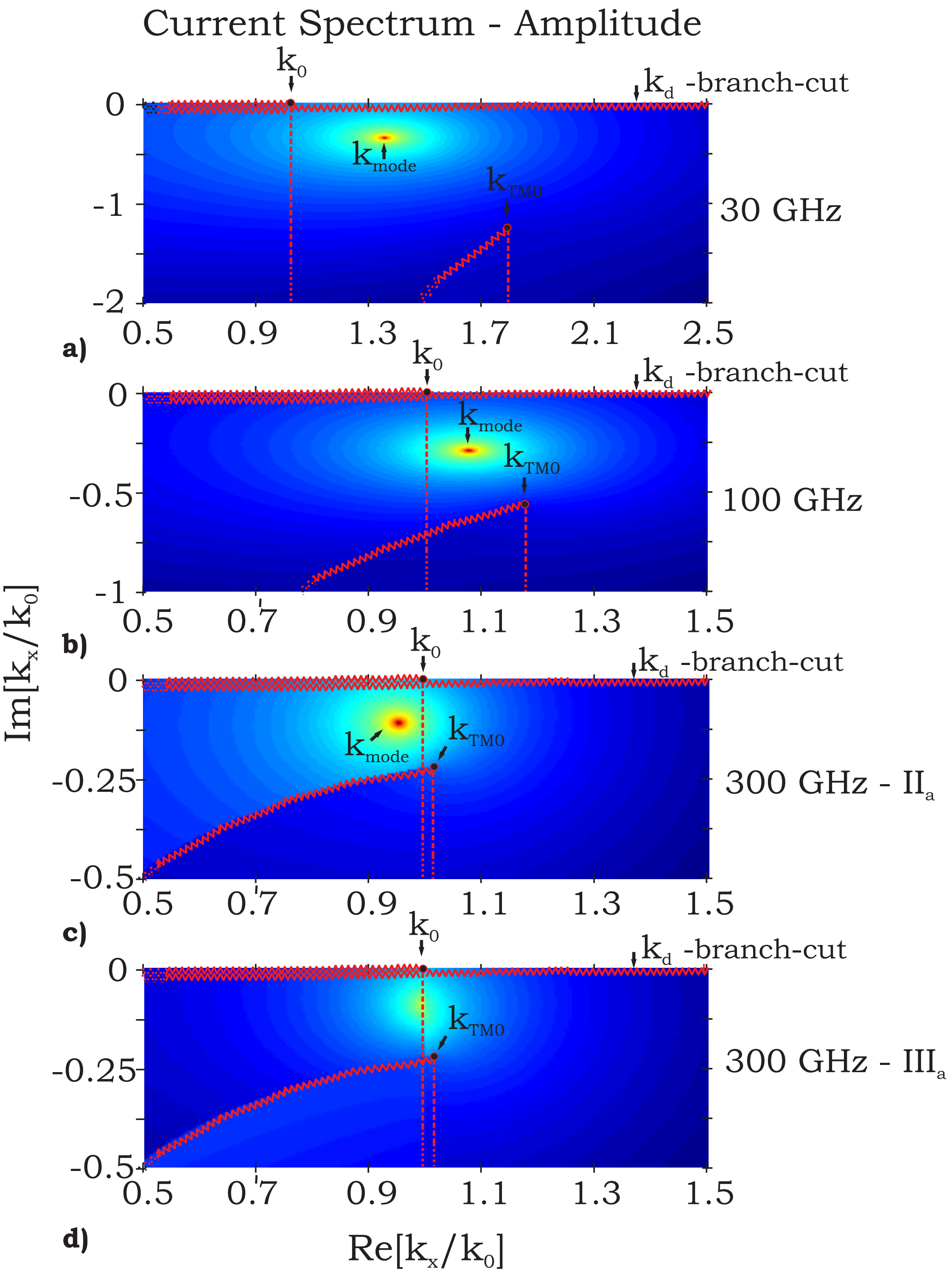

Figure 4.11: Current spectra for the slotline in Figure 4.9 with $w_s = 100\mu$m, $H = 100\mu$m, $\varepsilon_r = 11.9$ at 30 GHz, 100 GHz, 300 GHz. The branch-points and -cuts associated to the TM_0-leaky-wave and infinite medium of air are shown and the main propagating mode k_{mode} from Figure 4.10. The propagating mode in the third subfigure (300 GHz - II$_a$) is obtained by integrating according to Figure 3.11c; therefore the pole is actually not mathematically valid in this region ($\beta_{mode} < \beta_0$). Performing the correct transverse integration in the region $\beta_x < \beta_0$ (Figure 3.11e) results in the fourth subfigure (300 GHz - III$_a$); no mode is valid in the spectrum. A transition function is necessary in suchlike situations.

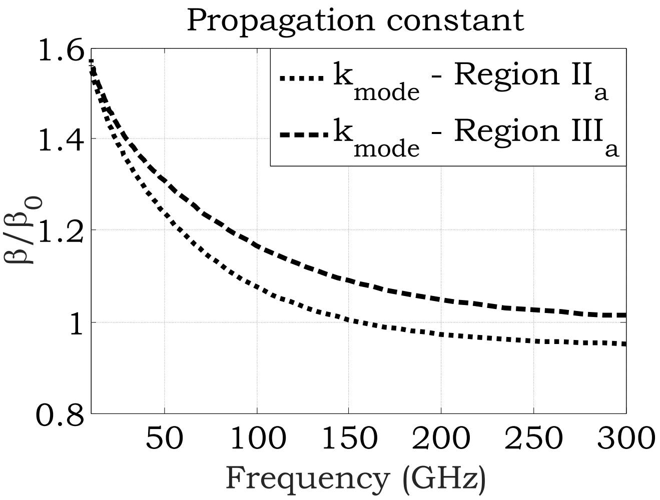

Figure 4.12: Propagating mode k_{mode} for the structure in Figure 4.9. $(\cdots)$ is obtained with a transverse integration path as in Figure 3.11c and therefore only mathematically valid in Region II, i.e. $k_0 < k_{mode} < k_d$. (- - -) is obtained with a transverse integration path as in Figure 3.11e and therefore only mathematically valid in Region III, i.e. $k_{mode} < k_0$. In 155 GHz $< f <$ 300 GHz no pole is mathematically valid.

Transition in Riemann-sheets

When we zoom in on the propagation constant ($Re[k]$) in Figure 4.10 as is shown in Figure 4.12, we can see that at 155 GHz, $Re[k_{mode}]$, now indicated with k_{mode}-Region II$_a$, will become lower than k_0. Referring to the discussion on the different regions in the current spectrum in Section 3.2 and Figure 3.7, we know that at this point the propagating mode crosses the log-type branch-cut from Region II$_a$ to Region III. Accordingly, the integration path in the transverse domain should be changed from Figure 3.11c to Figure 3.11e. However, when the integration path is changed correctly, the mode k_{mode}-Region III$_a$ in Figure 4.12 is found which is larger than β_0 and is therefore also not mathematically valid in this region. Of course physically, there should be a mode propagating along the line.

In order to prove that it is just the transition from sheet to sheet that gives the problem in the quasi-analytical model, consider the same structure (Figure 4.9), but now with an air-gap of

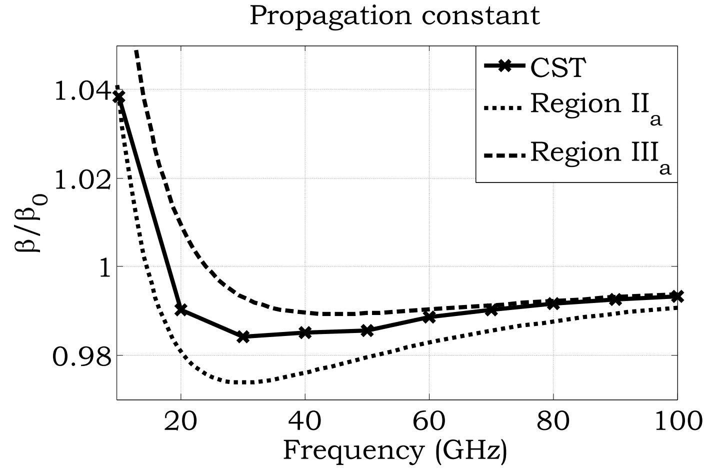

Figure 4.13: Propagating mode k_{mode} for the structure in Figure 4.9 but with $H = 1$ mm. $(\cdots)$ is obtained with a transverse integration path as inFigure 3.11c and therefore only mathematically valid in Region II, i.e. $k_0 < k_{mode} < k_d$. (- - -) is obtained with a transverse integration path as in Figure 3.11e and therefore only mathematically valid in Region III, i.e. $k_{mode} < k_0$. In 15 GHz $< f <$ 24 GHz no pole is mathematically valid.

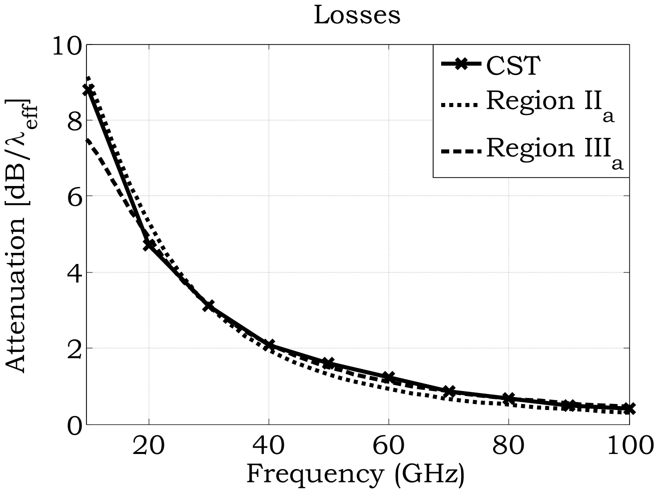

Figure 4.14: Attenuation in [dB/λ_{eff}] for the structure in Figure 4.9 but with $H = 1$ mm. ($\cdots$) is obtained with a transverse integration path as inFigure 3.11c and therefore only mathematically valid in Region II, i.e. $k_0 < k_{mode} < k_d$. (- - -) is obtained with a transverse integration path as in Figure 3.11e and therefore only mathematically valid in Region III, i.e. $k_{mode} < k_0$. In 15 GHz $< f <$ 24 GHz no pole is mathematically valid.

$H = 1$ mm. The electrical height of the air-gap is increased to show what happens after such transition. The propagating modes are shown in Figure 4.13. The transition is in this case from 15 GHz $< f <$ 24 GHz; no pole is mathematically valid in this region. We can see that, as expected, the propagation constant obtained by integrating as in Figure 3.11c, equals the CST simulation before the transition. After the transition ($f >$ 25 GHz) we can see that the propagation constant obtained by integrating as in Figure 3.11e, is converging towards the CST simulation, also as expected. The same can be said, although it is less clear, for the imaginary part of the wavenumber, which is expressed in dB/λ_{eff} in Figure 4.14.

Concluding from this analysis we can say that, in this quasi-analytical model, the transition of propagating modes to other Riemann-sheets can cause discontinuities in the wavenumber. This happens because of a change in integration path in the transverse domain, making the solution to the dispersion equation discontinuous. Physically, this transition happens smoothly. A transition function in the quasi-analytical model is required.

4.4 Surface-wave loss approximation

This section will conclude with the statement that when a dielectric slab with an electrical height $H > 0.5\lambda_d$ is present, the slab should be modeled as an infinite dielectric since the surface-wave losses in such dielectric slab will compare with the radiation losses of an infinite medium. We will start with analyzing a slotline printed on a 500μm slab, explaining the difficulties that arise as multiple modes will propagate. The significance in the excitation of these multiple modes is strongly varying. Subsequently, a CPW printed onto a large, but finite substrate is analyzed where it can be seen that now one mode is propagating. The losses associated with this mode can then be compared with radiation losses of a CPW in an infinite medium.

4.4.1 Slotline on a 500um substrate

In this example, the excitation of surface waves by a slotline is investigated (Figure 4.1b with $w_s = 100\mu$m, $H = 500\mu$m and $\varepsilon_r = 11.9$). The frequency range is

$$25 \text{ GHz } < f < 140 \text{ GHz}$$

equivalent to an electrical height of

$$0.14\lambda_d < H < 0.80\lambda_d$$

The surface-waves and propagating modes for this structure are shown in Figure 4.15. In this frequency range, two surface-waves are of importance; the TM_0- and TE_1-surface-waves. It can also be seen that two propagating modes are present in this frequency range [40]. The second mode, B, is obtained by enclosing both surface-wave poles in the transverse integration path. It is therefore that this mode is only mathematically valid when $k_B < k_{TE_1} < k_{TM_0}$, i.e. $f > 55$ GHz. Figure 4.15 can be divided into three regions:

1. $f \leq 5$ GHz; one mode (A) is propagating and will be strictly real; no surface-wave will be excited.
2. 55 GHz $< f <$ 72.5 GHz; the first mode (A) is still completely real, however a second-mode will excite both the TM_0- and TE_1-surface-waves. This second mode has a large imaginary part and is therefore highly attenuative.
3. 72.5 GHz $< f <$ 140 GHz; the first-mode is verifying the surface-wave condition ($k_A < k_{TM_0}$) and will leak into the TM_0-surface-wave. As the frequency approaches 140 GHz, the first propagating mode (A) is converging to and eventually merging with k_{TM_0}. The second propagating mode (B) will then be the most significant mode.

It is desired to see the change in significance of the two propagating modes as a function of the frequency. In order to calculate this, the power launched into each propagating mode can be calculated. The magnetic current spectrum is plotted in Figure 4.16 at 120 GHz. The points A and B are the poles related to the two propagating modes from Figure 4.15. The discontinuities in the spectrum at $Re[k_x]/k_0 = 2.8$ and 3.2, are originating from the surface-waves: when $k_x < k_{TM_0}$ (and $k_x < k_{TE_1}$), the residue of k_{TM_0} (and k_{TE_1}) is enclosed in the transverse integration as in Figure 3.6b). However, it can already be seen that magnitude of the first propagating mode (A) is less than the magnitude of the second propagating mode (B) at $f = 120$ GHz. From (3.46) and (3.47), it is clear that the amount of power going into the propagating mode is proportional to the residue of the propagating mode in the current spectrum (4.3). This is also described in [27].

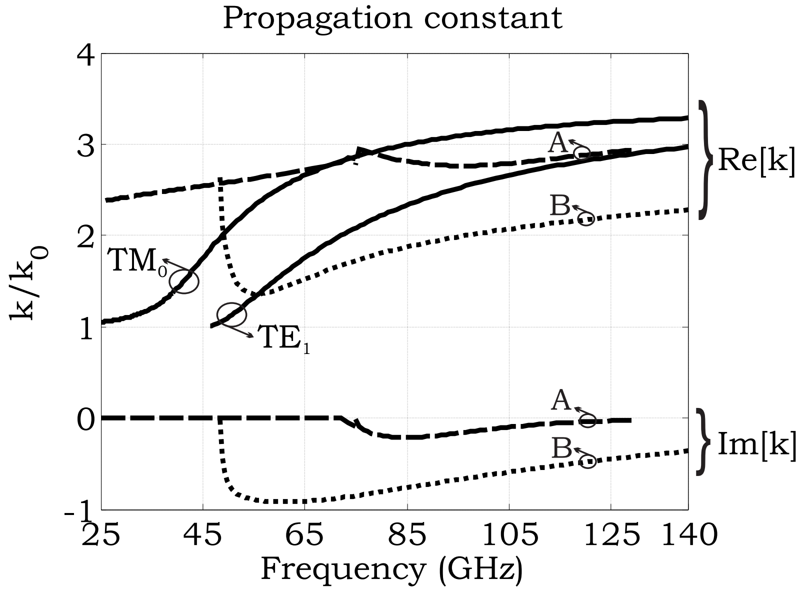

Figure 4.15: TM_0- and TE_1-surface-waves and propagating modes for a slotline (Figure 4.1b) with $w_s = 100\mu$m, $H = 500\mu$m and $\varepsilon_r = 11.9$.

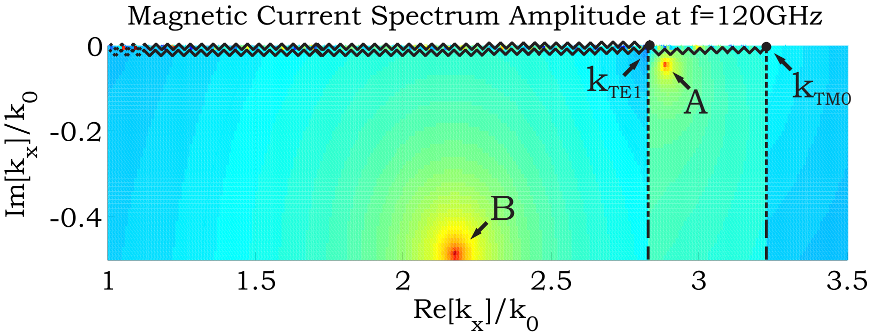

Figure 4.16: Magnetic current spectrum for a slotline (Figure 4.1b) with $w_s = 100\mu$m, $H = 500\mu$m and $\varepsilon_r = 11.9$ at $f = 120$ GHz. Points A and B are representing the two propagating modes from Figure 4.15. The branch-points and -cuts for the surface-waves are shown together with the surface-wave condition.

$$P \propto \frac{1}{D'(k_{pole})} \tag{4.3}$$

We can now define a so-called *launching efficiency*, $\eta_{k_{x,A}/k_{x,B}}$, which represents the amount of power going into the first propagating mode, $k_{x,A}$, versus the amount of power going into the second propagating mode, $k_{x,B}$, in percent (4.4).

$$\eta_{k_{x,A}/k_{x,B}} = \frac{|\mathrm{Res}(k_{x,A})|}{|\mathrm{Res}(k_{x,A})| + |\mathrm{Res}(k_{x,B})|} \cdot 100\%. \tag{4.4}$$

When $\eta_{k_{x,A}/k_{x,B}}$ is calculated in the range 85 GHz $< f <$ 130 GHz, we obtain Figure 4.17. From this figure, it is clear that the significance of the first mode A, decreases rapidly when the frequency increase. Mode A converges to and merges with the surface-wave pole k_{TE_1}, leaving mode B to be the most significant mode.

Having multiple modes propagating in a structure makes it extremely difficult to determine the amount of losses and significance of these losses in a transmission line. Also, predicting the existence and initial k_{init} (see (3.21)) of multiple modes becomes a difficult procedure. We will

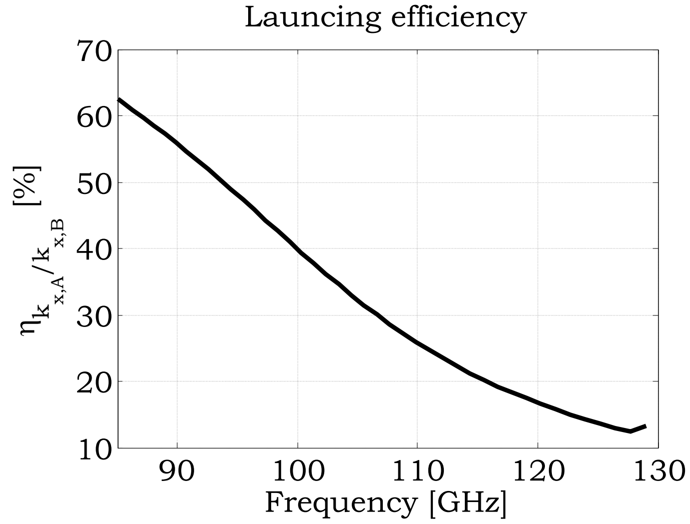

Figure 4.17: Launching efficiency as is defined in (4.4) for the two propagating modes in Figure 4.15. It describes the ratio of the power launched into modes A and B.

therefore analyze a CPW on a 500μm substrate were it can be seen that only one (leaky) mode will propagate so that a fair comparison can be made between these surface-wave excitation losses and the radiation of a CPW printed in between two infinite dielectrics.

4.4.2 CPW on a 500um substrate

The TM_0- and TE_1-surface-waves and propagating modes for a CPW (Figure 4.1c) with $w_s = 100\mu\text{m}$, $d = 100\mu\text{m}$, $H = 500\mu\text{m}$ and $\varepsilon_r = 11.9$ are shown in Figure 4.18. When the frequency increases, the propagation constant of the TM_0-surface wave mode will become larger than the propagation constant of the transmission line. At this point the surface wave will be excited and the surface wave poles have to be enclosed by the integration in the transverse domain (see Figure 3.11b). It can be seen that at approximately 63 GHz, the surface-wave condition $\beta_{mode} > \beta_{TM0}$ is verified. From this point on, the main propagating mode in the line becomes associated to surface-wave losses. As opposed to the previously discussed slotline, only one mode is physically valid as can be seen in the current spectrum at 140 GHz in Figure 4.19. Three frequency ranges can be seen:

1. $f \leq 63$ GHz; one mode (A) is propagating and will be strictly real; no surface-wave will be excited. Mode A is obtained by integrating only over the real axis in the transverse domain (Figure 3.11a).
2. 63 GHz $< f <$ 110 GHz; the second mode (B), obtained by enclosing the TM_0-surface-wave in the transverse domain (Figure 3.11b), is propagating and exciting the first surface-wave.
3. 110 GHz $< f <$ 150 GHz; the third mode (C), obtained by enclosing both the TM_0- and TE_1surface-waves in the transverse domain is verifying the surface-wave condition ($k_A < k_{TE_1} < k_{TM_0}$) and will leak into both surface-wave. Mode B loses its physical validity.

In contract to the multiple propagating modes of the slotline (Figure 4.15), there is no need to analyze the launching efficiency (4.4) of multiple modes in a CPW since only one mode is valid at every frequency. Therefore, in the next example, we can study the amount of losses associated to the crossing of these surface-wave boundaries ($\beta_{mode} < \beta_{SFW}$), with the amount of power radiated by a CPW printed in between two infinite dielectrics.

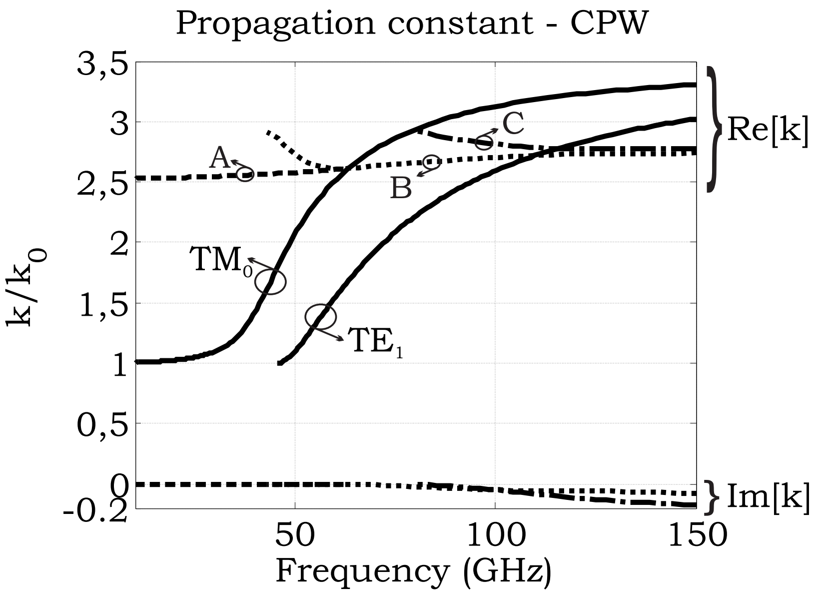

Figure 4.18: TM_0- and TE_1-surface-waves and propagating modes for a CPW (Figure 4.1c) with $w_s = 100\mu$m, $d = 100\mu$m, $H = 500\mu$m and $\varepsilon_r = 11.9$.

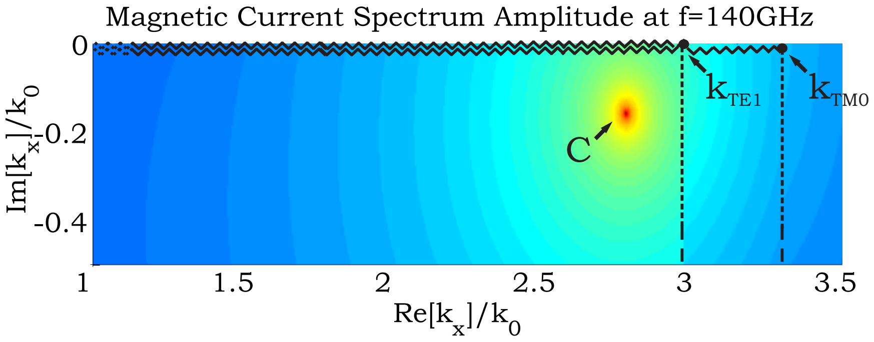

Figure 4.19: Magnetic current spectrum for a CPW (Figure 4.1c) with $w_s = 100\mu$m, $d = 100\mu$m, $H = 500\mu$m and $\varepsilon_r = 11.9$ at $f = 140$ GHz. Point C is representing the propagating mode C from Figure 4.18. The branch-points and -cuts for the surface-waves are shown.

4.4.3 CPW printed in between two infinite dielectrics

A CPW in the presence of an infinite dielectric half space simulating a silicon lens antenna is investigated; (Figure 4.1c) with $w_s = 100\mu$m, $d = 100\mu$m, $H = \infty$ and $\varepsilon_r = 11.9$. The high density infinite dielectric results in significant radiation of power in the lens which can be characterized by the software tool. The propagation constant of the dominant mode is already validated in Figure 4.2. As can be seen in the magnetic current spectrum at 140 GHz (Figure 4.21), the leaky-wave pole will be located in Region II of the longitudinal spectrum in Figure 3.5. Therefore, in the transverse domain, the integration path is required to travel through the bottom Riemann-sheet with respect to k_2 in order for the pole to be mathematically valid (see Figure 3.11c). The radiation loss of the transmission line can be extracted from the imaginary part of this leaky-wave pole and is shown in Figure 4.20. It can be seen that at 200 GHz, approximately 3 dB/λ_{eff}, where λ_{eff} is the effective guided wavelength, is radiated inside the silicon.

With this information provided, a conclusion can be made concerning the loss comparison between radiation into surface-waves and infinite media. This will be done in the following subsection.

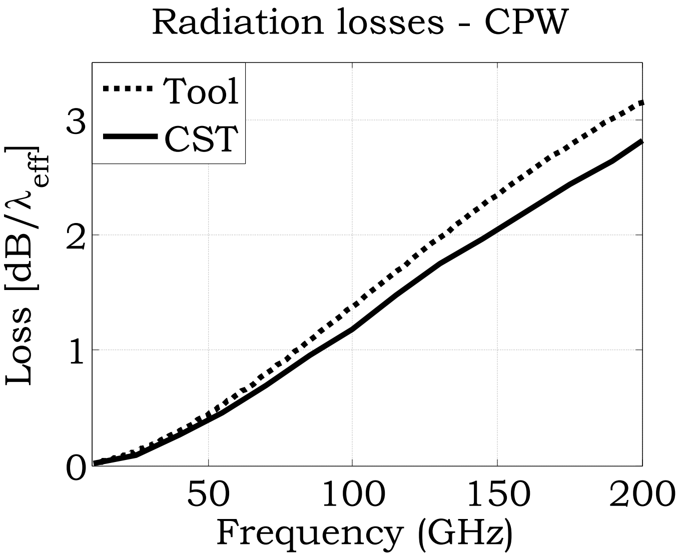

Figure 4.20: Radiation loss for a CPW (Figure 4.1c) with $w_s = 100\mu$m, $d = 100\mu$m, $H = \infty$ and $\varepsilon_r = 11.9$. The result is validated with a full-wave CST simulation.

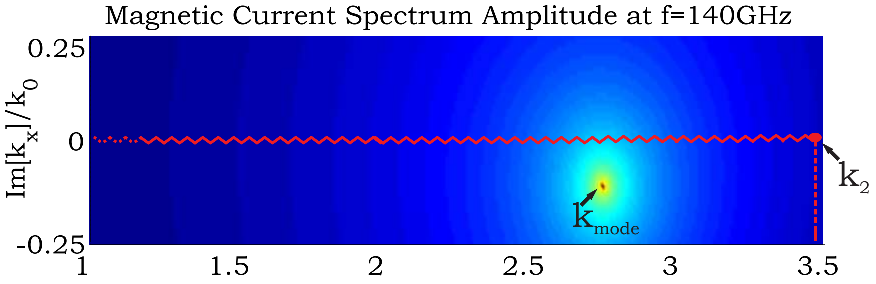

Figure 4.21: Magnetic current spectrum for a CPW (Figure 4.1c) with $w_s = 100\mu$m, $d = 100\mu$m, $H = \infty$ and $\varepsilon_r = 11.9$ at $f = 140$ GHz. Point k_{mode} is representing the main propagating mode in the structure. The branch-point (k_2) and -cuts from the infinite silicon medium is shown. The pole is located in Region II of Figure 3.5.

4.4.4 Surface-wave loss approximation

Analyzing the surface-waves and associated propagation modes of the slotline (Figure 4.15) it could be seen that the amount of losses in a transmission line are difficult to analyze. Multiple propagating modes are excited at a single frequency. The significance of each of these modes, in terms of launching efficiency, requires to be studied before a conclusion about the losses can be made. However, the surface-wave losses in a CPW, since only one mode is excited and propagating, can be compared with radiation of a CPW into an infinite medium. This comparison is shown in Figure 4.22). As reference, the conductor losses are also calculated where the conductors have a finite conductivity of $\sigma = 4.1 \cdot 10^7$ S/m. Curve B and C are associated to the surface-wave losses of propagating modes B and C from Figure 4.18. Analyzing Figure 4.22, it is clear that when the surface-wave is excited, the losses are soon comparable to the losses due to direct radiation in the infinite dielectric. This is also verified using full-wave CST-simulations.

Taking into account the difficulties that arise with the possible existence of multiple modes and the loss comparison in Figure 4.22, the proposed tool is only able to account for the first surface-wave. In the case when a dielectric slab is larger than $\lambda_d/2$ in height, the medium should therefore be modeled as an infinite dielectric.

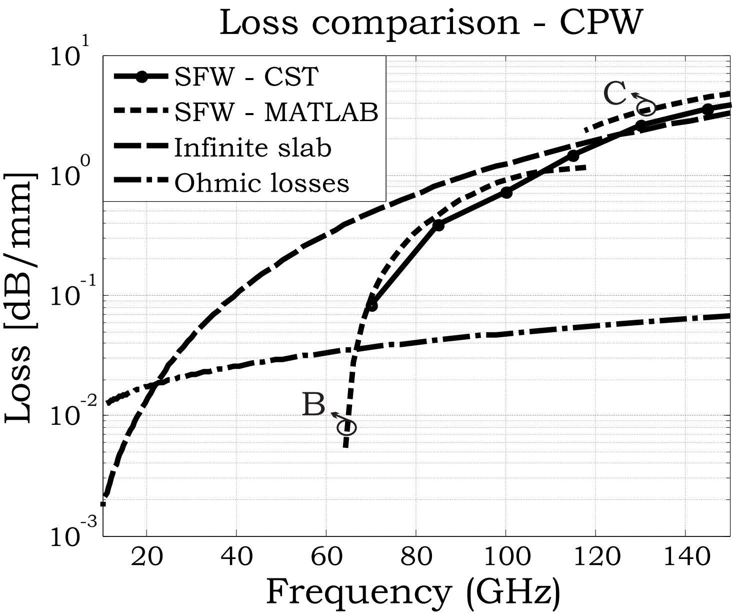

Figure 4.22: Loss comparison between a CPW (Figure 4.1c) printed onto a finite ($H = 500\mu$m) and infinite ($H = \infty$) dielectric slab with $w_s = 100\mu$m, $d = 100\mu$m and $\varepsilon_r = 11.9$. Also the ohmic losses are calculated where the conductors have a finite conductivity of $\sigma = 4.1 \cdot 10^7$ S/m. Curve B and C are associated to the surface-wave losses of propagating modes B and C from Figure 4.18.

4.5 Ohmic losses

In chapter 3 we discussed the implementation of ohmic losses in the proposed quasi-analytic model. Ohmic losses in a printed transmission line not only constitute conductor losses but also dielectric losses. This section will validate both of them. We will see that the dielectric losses, implemented by a complex relative permittivity, is accurately described by the model. Also ohmic losses for strip-type structures can be analyzed accurately. However, as will be explained in this section, the model is having troubles with accurately analyzing ohmic losses for slot-type structures.

4.5.1 Dielectric losses

In subsection 3.5.1 we have shown that dielectric losses are characterized by a loss tangent $\tan(\delta)$. This loss tangent can be used to calculate a complex relative permittivity for the dielectrics which can be implemented in the Green's functions (2.9). The complex permittivity was characterized by:

$$\varepsilon_{lossy} = \varepsilon_0 \varepsilon_r (1 - j\tan(\delta))$$

The dielectric losses for a microstrip and CPW (Figure 4.1a and c) is validated with $w_s = 100\mu$m, $d = 100\mu$m, $H = 127\mu$m and $\varepsilon_r = 11.9$. The dielectric slabs are characterized with a loss tangent of $\tan(\delta) = 0.005$. The results are shown in Figure 4.23 and are validated with CST. It can be seen that the quasi-analytical model is accurately describing dielectric losses.

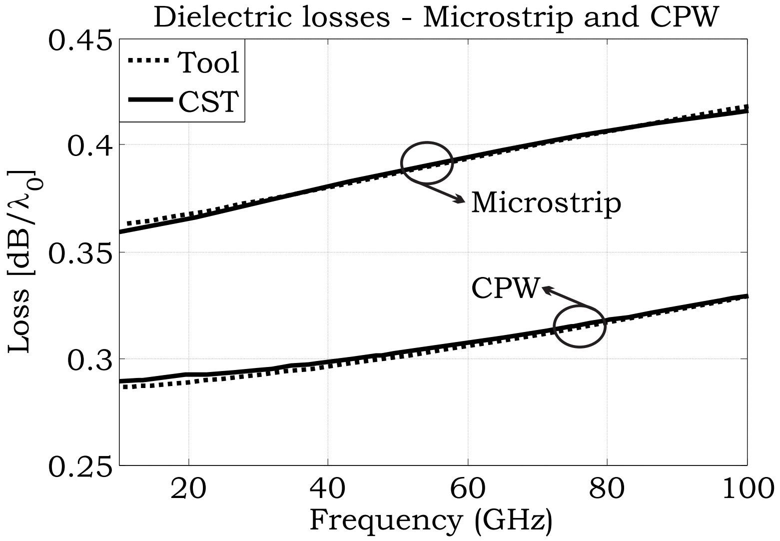

Figure 4.23: Dielectric losses for a microstrip and a CPW (Figure 4.1a and c) with $w_s = 100\mu$m, $d = 100\mu$m, $H = 127\mu$m and $\varepsilon_r = 11.9$. The dielectrics are characterized with a loss tangent of $\tan((\delta)) = 0.005$. The result is validated with CST.

4.5.2 Conductor losses

In this subsection we will validate the conductor losses for a microstrip and CPW. As was explained in subsection 3.5.2, the losses for the ground-plane in a microstrip can be implemented in the Green's functions, while the losses for the strip itself results in a non-zero tangential total electric field in (3.1) leading to a new denominator $\underline{\underline{D}}_{loss}(\underline{k}_{mode})$. The losses for slot-type structures were implemented in the Green's functions by means of an impedance in series with the stratification.

In Figure 4.24a the conductor losses of a microstrip (Figure 4.1a) is validated with $w_s = 100\mu$m, $H = 127\mu$m, $\varepsilon_r = 11.9$ and $\sigma = 4.1 \cdot 10^7$ S/m. For the microstrip, both main conductor and ground-plane are non-perfect. The results are validated with Sonnet. The calculated ohmic

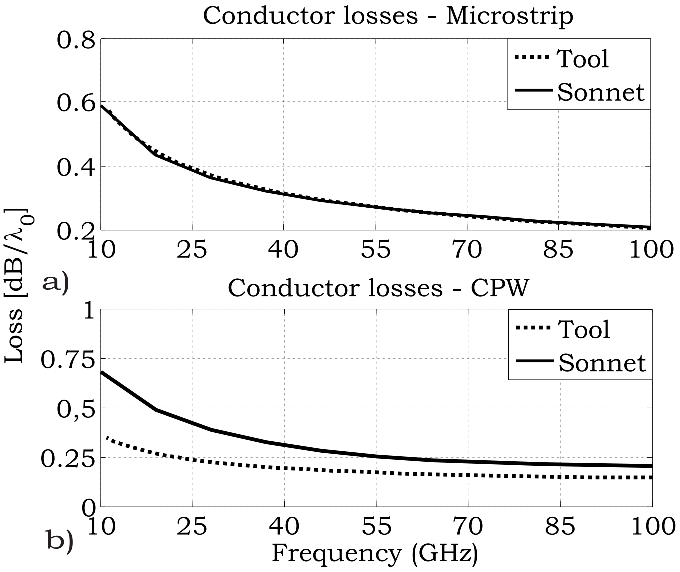

Figure 4.24: Conductor losses for a) a microstrip and b) a CPW (Figure 4.1a) with $w_s = 100\mu$m, $d = 100\mu$m $H = 127\mu$m, $\varepsilon_r = 11.9$ and $\sigma = 4.1 \cdot 10^7$ S/m. For the microstrip, both main conductor and ground-plane have a finite conductivity. The results are validated with Sonnet.

losses for the microstrip correlates nicely with the sonnet simulation. However in the last paragraph of this section we will explain that this comparison has a catch, concerning a current distribution assumption which is made.

In Figure 4.24b the conductor losses of a CPW (Figure 4.1c) is validated with $w_s = 100\mu$m, $d = 100\mu$m, $H = 127\mu$m, $\varepsilon_r = 11.9$ and $\sigma = 4.1 \cdot 10^7$ S/m. In contrast to the microstrip validation, it can be seen that the conductor losses for the CPW differ significantly from the simulation. The reason for this can be found in two assumptions. First, after applying the equivalence principle on the slot region, a small equivalent electric current will be flowing in the slot area giving rise to a coupling term as is explained in [33] and subsection 3.5.2. This coupling term is neglected in the software-tool. Secondly, the use of one basis-function for the transverse current distribution, $c_t(y)$, is not sufficient as can be seen in Figure 4.25; with small spacing d, the field distribution $E_y(y)$ is asymmetric.

Another cause for inaccuracy, for both slot- and strip-type structures, is the modeling of the conductor to be infinitesimal. This assumption results in two consequences. First, no change in field distribution is considered due to the presence of a finite thickness conductor. Secondly, the current flowing on the top of the conductor is considered to be equal to the current flowing on the bottom of the conductor. However, for a microstrip on top of a dense dielectric, the current will mainly flow on the bottom of the conductor. This will have its influence on the effective surface impedance of the conductor as is described in [41,42]. However, these effects are not considered in the proposed software tool. In fact, the Sonnet simulation in Figure 4.24a also assumes that the current flowing on the top and bottom of the conductor are equal; this is actually, as we explained, not the case.

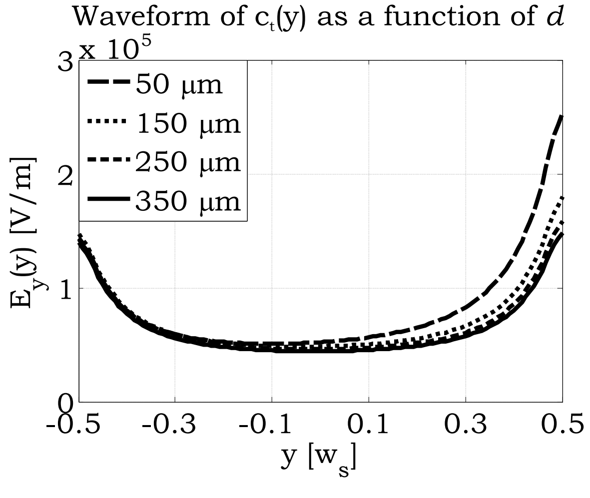

Figure 4.25: $E_y(y)$-field component of a CPW (Figure 4.1a) with $w_s = 100\mu$m, $H = 127\mu$m, $\varepsilon_r = 11.9$ and $\sigma = 4.1 \cdot 10^7$ S/m at $f = 100$ GHz. $d = 50 - 350\mu$m. This electric-field component, obtained from a CST-simulation, represents the transverse current distribution $c_t(y)$.

4.6 Superconductivity

The superconductive phenomenon is implemented by means of a surface-impedance as defined in Section 3.6. We will study the effect of utilizing superconductive materials on the complex wavenumber and characteristic impedance. For this we will give two examples.

Effect of superconductive materials on attenuation constant

We will study the effect of superconductivity on the radiation from a printed line. The structure used is a CPW with $w_s = 0.5 - 2.0$ μm, $d = 0.5 - 2.0$ μm, $f = 350$ GHz, beneath an infinite medium with $\varepsilon_r = 10.33$. Such transmission lines is widely used in the resonators of Kinetic Inductance Detectors (KIDs). KIDs are commonly used in the THz-domain for space-applications. The results are shown in Figure 4.26 where the radiative losses are compared when PEC is used for the main conductors and when superconductors are used. The superconductors are characterized by a sheet inductance of $L_s = 0.45$ pH/sq. It can be seen that using superconductive materials can have a significant impact on the complex wavenumber, in this case the attenuation constant due to radiation.

Effect of superconductive materials on propagation constant and characteristic impedance

As a second example, we will study the effect of superconductivity on the characteristic impedance and propagation constant of a CPW (Figure 4.1c) with $w_s = 1.5\mu$m, $d = 1.5\mu$m, $H = 10\mu$m and $\varepsilon_r = 11.9$. We have chosen a CPW printed onto a finite slab, because the Sonnet simulation on an infinite dielectric from Figure 4.26 took hours. Again, in this comparison the superconductor is characterized by a sheet inductance of $L_s = 0.45$ pH/sq. The comparison is shown in Figure 4.27. It is clear that using a superconductive material can have a significant influence on as well the propagation constant as the characteristic impedance of a CPW. No analytical or equivalent formulas can estimate these effects on the propagation constant and characteristic impedance of a transmission line; one has to resort to the use of full-wave simulators.

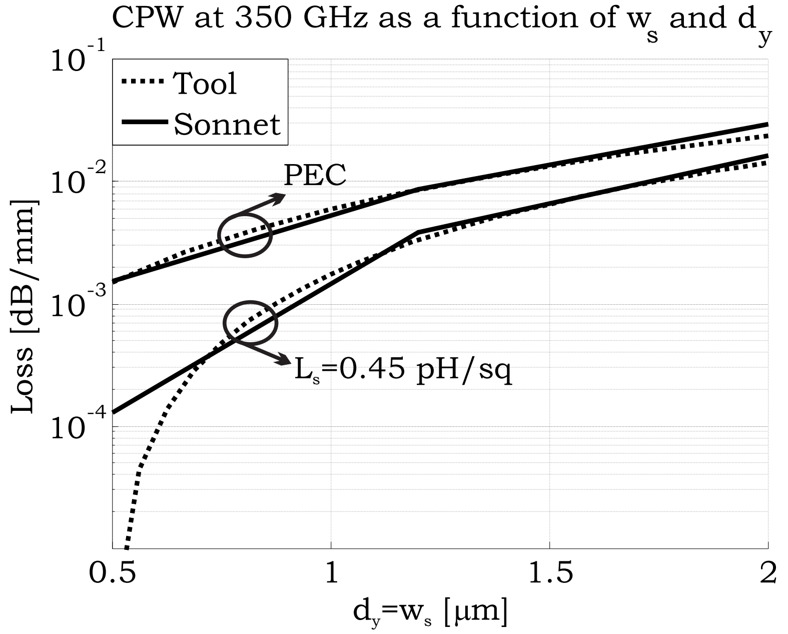

Figure 4.26: Effect of using a superconductor with $L_s = 0.45$ pH/sq is investigated on the amount of radiative losses of a CPW (Figure 4.1c) with $w_s = 0.5 - 2.0$ μm, $d = 0.5 - 2.0$ μm, $f = 350$ GHz, beneath an infinite medium with $\varepsilon_r = 10.33$. The results are validated with Sonnet.

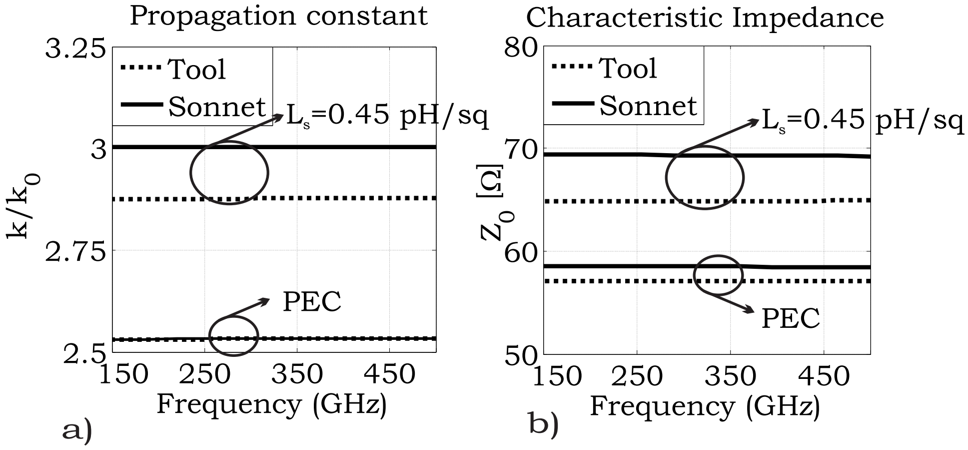

Figure 4.27: Effect of using a superconductor with $L_s = 0.45$ pH/sq is investigated in a) the propagation constant and b) characteristic impedance of a CPW (Figure 4.1c) with $w_s = 1.5\mu$m, $d = 1.5\mu$m, $H = 10\mu$m and $\varepsilon_r = 11.9$. The results are validated with Sonnet.

Chapter 5

Conclusions and Future work

5.1 Summary and conclusions

In this thesis we discussed a quasi-analytical model allowing for fast characterization of printed transmission lines. The characterization of a transmission line is done in terms of wavenumber, characteristic impedance and losses due to both ohmic- and radiative losses. The need for this quasi-analytical model comes from the fact that no analytical tools exist for the characterization of printed transmission lines in terms of radiative losses; A few equivalent formulas exist for approximating these phenomena that only cover a small subset of printed transmission lines. A front-end designer has to resort to full-wave simulators which are time-consuming and also require expensive licenses. The proposed quasi-analytical model allows for the characterization of several interesting phenomena such as surface-wave excitation, radiation and superconductivity. The model is referred to as *quasi*-analytical as it depends on numerical integrations and derivations.

The model is based on solving the dispersion equation, resulting from a spectral representation of the integral equations. This representation is formulated according to the transmission line formalism. The Green's functions used, can characterize printed transmission lines with multiple and arbitrary stratifications, as long as they are homogeneous in the transverse plane. Subsequently, this quasi-analytical model is tested by validating and discussing the transmission line characteristics with full-wave simulations. The quasi-analytical model is also implemented in a software-tool which allows for a quick evaluation of the losses and impedance matching. This software-tool is made freely available for download at our group's website (http://terahertz.tudelft.nl).

In chapter 2 we covered some basic theory needed for characterizing printed transmission lines. We explained the need for using spectral Green's functions after which the equivalent transmission line spectral Green's function model was discussed. It turned out that this formalism is extremely useful for characterizing transmission lines with arbitrary stratifications, as long as they are homogeneous in the transverse plane. Subsequently we discussed the singularities that can be found in these Green's functions. These singularities are associated to space-waves, leaky-waves and surfaces-waves which are intrinsic to the stratification. The basic propagation mechanisms of leaky- and surface-waves were investigated where-after the field distributions due to the singularities in the Green's functions associated to these leaky- and surface-waves were analyzed.

In chapter 3 the quasi-analytical model used for transmission line characterization was discussed. We started with imposing the Electric Field Integral Equation (EFIE) and Continuity of Magnetic Field Integral Equation (CMFIE) on the strip and slot. After translating these integral equations to the spectral domain we ended up with an expression for the longitudinal electric or magnetic current along the transmission line in terms of an inverse-Fourier transform. We explained that the singularities in the integrand of this inverse-Fourier transform, the current spectrum, are associated to the propagating modes along the transmission lines which can be extracted by solving the dispersion equation.

We showed that solving this dispersion is non-trivial as it depends on the transverse integration path. With this in mind, a rigorous analysis of the longitudinal- and transverse spectral plane was conducted. In this analysis we analyzed the present branch-points and -cuts whereafter we were able to define different regions in the spectral plane where we can find different propagating modes with different characteristics. While making sure that the propagating modes are physically valid, we explained the transverse integration path required to find these different propagating modes. Finally, we investigated when the leaky- and surface-waves, explained in chapter 2, are actually excited on the transmission line. This condition is referred to as the surface-wave condition and stated that when the propagation constant of the propagating mode is lower than the propagation constant of the intrinsic surface-wave mode, this surface-wave was excited.

Subsequently we described the procedure for calculating the characteristic impedance of the transmission line. It was explained that this impedance was defined as the characteristic impedance of the dominant propagating mode. Also the relation between the characteristic impedance of the dominant propagating mode and the input-impedance seen from the delta-gap excitation of the line was shown.

The next section discussed the implementation of ohmic losses in the quasi-analytical model. Ohmic losses constitutes conductor losses and dielectric losses. The latter could be easily implemented by defining a complex relative permittivity of the dielectrics using a loss tangent. Conductor losses of any ground-planes were integrated in the Green's function using the high-frequency surface-impedance as a boundary condition. Conductor losses of a strip were implemented by reformulating the EFIE where we had to take account of a non-zero total tangential electric field. This field component led to a new dispersion equation to solve. Lastly, the conductor losses of a slot were integrated in the Green's function. However, we explained that neglecting the, now non-zero, equivalent electric currents is giving rise to inaccuracy.

Finally, the implementation of the superconductive phenomenon was explained. It turned out that superconductivity can be described by means of a complex surface-impedance where the reactance was a function of the London penetration depth which is key parameter of superconductive material.

In chapter 4 we validated the quasi-analytical model from chapter 3. Dispersion behavior of printed transmission lines over a wide frequency range could easily be analyzed. Subsequently it was shown that the characteristic impedance of a highly attenuative propagating mode nearby any spectrum singularities could differ significantly from the input-impedance seen from the delta-gap excitation of the line.

The next section covered some examples regarding radiation into leaky- and surface-waves. We started with the analysis of surface-wave excitation in a microstrip. It turned out that multiple (leaky) modes can be excited and propagate parallel to each other. The first example showed the dynamic behavior of a microstrip at high frequencies when the dimensions of the slab become significant in terms of wavelength. Subsequently a slotline in the presence of an infinite dielectric, separated by an air-gap, was investigated. We saw that the main-propagating mode becomes faster than the free-space wavenumber, making a transition in Riemann-sheets. Concluding from this analysis we said that, in this quasi-analytical model, the transition of propagating modes between different Riemann-sheets causes discontinuities in the wavenumber. The reason for this discontinuity is a change in integration path in the transverse domain, making the solution to the dispersion equation discontinuous. We showed that, physically, this transition happens smoothly. A transition function in the quasi-analytical model is required.

Subsequently we studied the amount of losses associated to surface-wave excitation. A conclusion was made after comparing the losses due to surface-wave excitation and direct radiation of a CPW. After observing that these losses were soon in the same order of magnitude, we concluded that dielectric slabs with an electrical height larger than half a wavelength should be modeled as an infinite dielectric.

Finally in this chapter we validated the model for ohmic losses and superconductive materials. We saw that dielectric losses are accurately analyzed as well as the conductor losses for strip-type structures. However, conductor losses for slot-type structures were observed to be less accurate. We concluded that using one basis-function may not be sufficient together with the fact that the equivalent electric currents were neglected.

The tool is made freely accessible from our group's website at http://terahertz.tudelft.nl/.

5.2 Future work

The proposed quasi-analytical model proved to be working very accurately in characterizing printed transmission lines. However, we have shown that a transition to a different Riemann-sheet in the spectral plane can cause a discontinuity in the wavenumber. Some kind of transition function between the different sheets is desired in these situations. Furthermore we have seen an inaccuracy in characterizing the conductor losses in slot-type structures. Extended research is necessary for constructing an integral equation capable of including the electric currents running on the slot region, after applying the equivalence theorem.

The developed software-tool, based on the proposed quasi-analytical model, will be updated according to any recommendations from users. Especially because the model is quasi-analytical, the implementation of other features can easily be done. For example, losses in a dielectric can also be described by means of a finite conductivity rather than a loss tangent. Also, other definitions of the conductors surface-impedance can be implemented, taking into account surface-roughness or features associated to a finite thickness of the conductors.

5.3 Publications

1. S.L. van Berkel, A. Garufo, A. Endo, N. LLombart and A. Neto, “Characterization of Printed Transmission Lines at High Frequencies," *The 9th European Conference on Antennas and Propagation (EuCAP 2015)*, Lisbon, Portugal Apr. 12-17, 2015.

2. *To be submitted:* A magazine article will be extracted from this thesis to be submitted to the IEEE Antennas and Propagation Magazine.

Bibliography

[1] K. Gupta, R. Garg, I. Bahl, and P. Bhartia, *Microstrip lines and slotlines, Second Edition*. Artech house, 2013.

[2] E. Denlinger, “A frequency dependent solution for microstrip transmission lines,” *Microwave Theory and Techniques, IEEE Transactions on*, vol. 19, no. 1, pp. 30–39, Jan 1971.

[3] T. Itoh and R. Mittra, “Spectral-domain approach for calculating the dispersion characteristics of microstrip lines (short papers),” *Microwave Theory and Techniques, IEEE Transactions on*, vol. 21, no. 7, pp. 496–499, Jul 1973.

[4] J. Knorr and A. Tufekcioglu, “Spectral-domain calculation of microstrip characteristic impedance,” *Microwave Theory and Techniques, IEEE Transactions on*, vol. 23, no. 9, pp. 725–728, Sep 1975.

[5] N. K. Das and D. M. Pozar, “A generalized spectral-domain green’s function for multilayer dielectric substrates with application to multilayer transmission lines,” *Microwave Theory and Techniques, IEEE Transactions on*, vol. 35, no. 3, pp. 326–335, 1987.

[6] N. Das and D. M. Pozar, “Full-wave spectral-domain computation of material, radiation, and guided wave losses in infinite multilayered printed transmission lines,” *Microwave Theory and Techniques, IEEE Transactions on*, vol. 39, no. 1, pp. 54–63, Jan 1991.

[7] J. Hornsby and A. Gopinath, “Numerical analysis of a dielectric-loaded waveguide with a microstrip line-finite-difference methods,” *Microwave Theory and Techniques, IEEE Transactions on*, vol. 17, no. 9, pp. 684–690, Sep 1969.

[8] H. Green, “The numerical solution of some important transmission-line problems,” *Microwave Theory and Techniques, IEEE Transactions on*, vol. 13, no. 5, pp. 676–692, Sep 1965.

[9] J. Svacina, “Analysis of multilayer microstrip lines by a conformal mapping method,” *Microwave Theory and Techniques, IEEE Transactions on*, vol. 40, no. 4, pp. 769–772, Apr 1992.

[10] J. Knorr and K. Kuchler, “Analysis of coupled slots and coplanar strips on dielectric substrate,” *Microwave Theory and Techniques, IEEE Transactions on*, vol. 23, no. 7, pp. 541–548, Jul 1975.

[11] D. Kasilingam and D. Rutledge, “Surface-wave losses of coplanar transmission lines,” in *Microwave Symposium Digest, 1983 IEEE MTT-S International*, May 1983, pp. 113–116.

[12] F. Mesa, D. Jackson, and M. J. Freire, “Evolution of leaky modes on printed-circuit lines,” *Microwave Theory and Techniques, IEEE Transactions on*, vol. 50, no. 1, pp. 94–104, Jan 2002.

[13] H. Shigesawa, M. Tsuji, and A. Oliner, “Simultaneous propagation of bound and leaky dominant modes on printed-circuit lines: a new general effect,” *Microwave Theory and Techniques, IEEE Transactions on*, vol. 43, no. 12, pp. 3007–3019, Dec 1995.

[14] M. Riaziat, R. Majidi-Ahy, and I.-J. Feng, “Propagation modes and dispersion characteristics of coplanar waveguides,” *Microwave Theory and Techniques, IEEE Transactions on*, vol. 38, no. 3, pp. 245–251, Mar 1990.

[15] F. Mesa, C. Di Nallo, and D. Jackson, "The theory of surface-wave and space-wave leaky-mode excitation on microstrip lines," *Microwave Theory and Techniques, IEEE Transactions on*, vol. 47, no. 2, pp. 207–215, Feb 1999.

[16] A. Neto and S. Maci, "Green's function for an infinite slot printed between two homogeneous dielectrics. i. magnetic currents," *Antennas and Propagation, IEEE Transactions on*, vol. 51, no. 7, pp. 1572–1581, July 2003.

[17] L. B. Felsen and N. Marcuvitz, *Radiation and scattering of waves.* John Wiley & Sons, 1994, vol. 31.

[18] D. Cavallo, "Connected array antennas: Analysis and design," Ph.D. dissertation, University of Eindhoven, 2011.

[19] N. LLombart, "Development of integrated printed array antennas using EBG substrates," Ph.D. dissertation, Polytechnic University of Valencia, 2006.

[20] D. Pozar, *Microwave Engineering, 4th Edition.* Wiley Global Education, 2011.

[21] F. Mesa and D. Jackson, "Investigation of integration paths in the spectral-domain analysis of leaky modes on printed circuit lines," *Microwave Theory and Techniques, IEEE Transactions on*, vol. 50, no. 10, pp. 2267–2275, Oct 2002.

[22] S. Bruni, N. Llombart, A. Neto, G. Gerini, and S. Maci, "Problem-matched basis functions for microstrip coupled slot arrays based on transmission line green's functions (TLGF)," *Antennas and Propagation, IEEE Transactions on*, vol. 53, no. 11, pp. 3556–3567, Nov 2005.

[23] F. Mesa, D. Jackson, and M. J. Freire, "High-frequency leaky-mode excitation on a microstrip line," *Microwave Theory and Techniques, IEEE Transactions on*, vol. 49, no. 12, pp. 2206–2215, Dec 2001.

[24] A. Neto and S. Maci, "Input impedance of slots printed between two dielectric media and fed by a small delta-gap," *Antennas and Wireless Propagation Letters, IEEE*, vol. 3, no. 1, pp. 113–116, Dec 2004.

[25] N. Das, "A new theory of the characteristic impedance of general printed transmission lines applicable when power leakage exists," *Microwave Theory and Techniques, IEEE Transactions on*, vol. 48, no. 7, pp. 1108–1117, Jul 2000.

[26] S. Bruni, "Wide band leaky wave radiation for integrated antennas and arrays," Ph.D. dissertation, University of Siena, 2006.

[27] F. Mesa and D. Jackson, "A novel approach for calculating the characteristic impedance of printed-circuit lines," *Microwave and Wireless Components Letters, IEEE*, vol. 15, no. 4, pp. 283–285, April 2005.

[28] C. Holloway and E. F. Kuester, "A quasi-closed form expression for the conductor loss of cpw lines, with an investigation of edge shape effects," *Microwave Theory and Techniques, IEEE Transactions on*, vol. 43, no. 12, pp. 2695–2701, Dec 1995.

[29] F. Bouzidi, H. Aubert, D. Bajon, and H. Baudrand, "Equivalent network representation of boundary conditions involving generalized trial quantities-application to lossy transmission lines with finite metallization thickness," *Microwave Theory and Techniques, IEEE Transactions on*, vol. 45, no. 6, pp. 869–876, Jun 1997.

[30] T. van Deventer, P. Katehi, and A. Cangellaris, "An integral equation method for the evaluation of conductor and dielectric losses in high-frequency interconnects," *Microwave Theory and Techniques, IEEE Transactions on*, vol. 37, no. 12, pp. 1964–1972, Dec 1989.

[31] J.-Y. Ke and C. H. Chen, "Dispersion and attenuation characteristics of coplanar waveguides with finite metallization thickness and conductivity," *Microwave Theory and Techniques, IEEE Transactions on*, vol. 43, no. 5, pp. 1128–1135, May 1995.

[32] E. Hamham, F. Mesa, F. Medina, and M. Khalladi, "Surface-impedance quasi-transverse electromagnetic approach for the efficient calculation of conductor losses in multilayer single and coupled microstrip lines," *Microwaves, Antennas Propagation, IET*, vol. 6, no. 5,

pp. 519–526, April 2012.

[33] M. Albani, A. Mazzinghi, and A. Freni, "Rigorous MoM analysis of finite conductivity effects in rlsa antennas," *Antennas and Propagation, IEEE Transactions on*, vol. 59, no. 11, pp. 4023–4032, Nov 2011.

[34] M. Mattes and J. Mosig, "Integral equation formulation for the impedance representation of aperture-coupled devices with finite wall conductivity," in *Wireless Communications and Applied Computational Electromagnetics, 2005. IEEE/ACES International Conference on*, April 2005, pp. 865–868.

[35] S. Doyle, P. Mauskopf, J. Naylon, A. Porch, and C. Duncombe, "Lumped element kinetic inductance detectors," *Journal of Low Temperature Physics*, vol. 151, no. 1-2, pp. 530–536, 2008.

[36] V. V. Schmidt, P. Müller, and A. V. Ustinov, *The physics of superconductors: introduction to fundamentals and applications*. Springer Science & Business Media, 1997.

[37] A. Iacono, "Large focal plane arrays for thz imaging," Ph.D. dissertation, University of Eindhoven, 2012.

[38] A. Neto, S. Monni, and F. Nennie, "UWB, non dispersive radiation from the planarly fed leaky lens antenna. Part II: demonstrators and measurements," *Antennas and Propagation, IEEE Transactions on*, vol. 58, no. 7, pp. 2248–2258, July 2010.

[39] A. Neto, N. Llombart, J. Baselmans, A. Baryshev, and S. Yates, "Demonstration of the leaky lens antenna at submillimeter wavelengths," *Terahertz Science and Technology, IEEE Transactions on*, vol. 4, no. 1, pp. 26–32, Jan 2014.

[40] J. Zehentner, J. Machac, and M. Migliozzi, "Upper cutoff frequency of the bound wave and new leaky wave on the slotline," *Microwave Theory and Techniques, IEEE Transactions on*, vol. 46, no. 4, pp. 378–386, Apr 1998.

[41] J. C. Rautio, "An investigation of microstrip conductor loss," *Microwave Magazine, IEEE*, vol. 1, no. 4, pp. 60–67, Dec 2000.

[42] J. C. Rautio and V. Demir, "Microstrip conductor loss models for electromagnetic analysis," *Microwave Theory and Techniques, IEEE Transactions on*, vol. 51, no. 3, pp. 915–921, Mar 2003.

Appendix A

Construction of the Integral Equations

In this appendix, a more extensive derivation of the spectral integral equations is discussed. We will start with the boundary conditions of the tangential electric (magnetic) field components along the strip (slot). From there, a spatial representation of the integral equations will be derived including multiple conductors. After expressing the integral equations in the spectral domain and averaging the fields over the width of strip or the slot we will arrive at the final expression used for this thesis; an inverse Fourier transform in the longitudinal domain of the lines representing the longitudinal electric- or magnetic currents.

A.1 Formulation

We are considering two categories of integrated transmission lines based on the kind of current running along the transmission line:

1. Strip-type structures (electric current $j(x)$)
   - Strip
   - Microstrip
   - Stripline
   - Coupled stripes
   - Coupled microstrip
2. Slot-type structures (magnetic current $m(x)$)
   - Slot
   - Coplanar waveguide
   - Grounded coplanar waveguide

We are assuming the transmission lines to be infinitely long along $\hat{\boldsymbol{x}}$, the conductors infinitesimal and a homogeneity in the ($\hat{\boldsymbol{x}}$,$\hat{\boldsymbol{y}}$)-plane. The width of the metal strips and slot is w_s and the spacing between the centers of two parallel lines is d_y. For now, the conductors are assumed to be lossless, later on they will be characterized by a boundary condition using the high-frequency surface impedance Z_s. The problem will be formulated according to two types of integral equations; the Electric Field Integral Equation (EFIE) for strip-type structures [15], [21] and the Continuity of Magnetic Field Integral Equation (CMFIE) for slot-type structures [16].

A.2 Excitation and boundary conditions

The excitation of the transmission lines are modeled by a Δ-gap excitation, $s_\Delta(x,y)$, as is shown in Figure A.1. For strip-type lines as in Figure A.1a, the excitation $s_\Delta(x,y)$ will be a magnetic current $m_\Delta(x,y)$ while for slot-type lines as in Figure A.1b, the excitation $s_\Delta(x,y)$ will be an

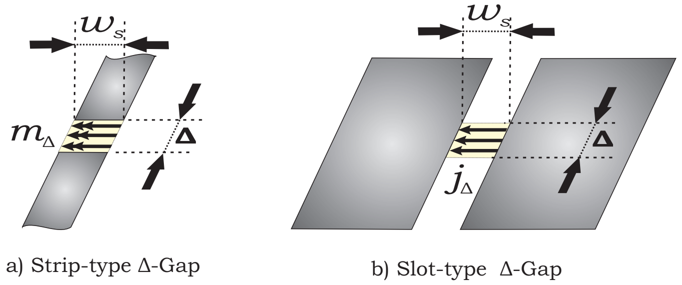

Figure A.1: Δ-Gap excitation, $s_\Delta(x,y)$, for strip-type: $m_\Delta(x,y)$ (a) and slot-type: $j_\Delta(x,y)$ (b) transmission lines

electric current $j_\Delta(x,y)$. The longitudinal dimension of the excitation, Δ, will be defined as $\Delta = 0.7 \cdot w_s$. For N coplanar lines, the excitation can be described as a vector $\underline{\boldsymbol{s}}_\Delta(x,y)$ (A.1)

$$\underline{\boldsymbol{s}}_\Delta(x,y) = \underline{s}_\Delta(x,y)\hat{\boldsymbol{y}} = \underline{n}_0(x)\underline{n}_t(y)\hat{\boldsymbol{y}} \tag{A.1}$$

with elements as in Eq. (A.2)

$$\begin{aligned} s_{\Delta,n}(x,y) &= n_{0,n}(x)n_{t,n}(y) \\ &= s_{0,n} \cdot \operatorname{rect}\left(\frac{x}{\Delta}\right)\operatorname{rect}\left(\frac{y-nd_y}{w_s}\right) \end{aligned} \tag{A.2}$$

for $n = 0 : N-1$. In (A.2), d_y is the spacing between the centers of the coplanar lines and $s_{0,n}$ are the excitation coefficients in order to select any propagation modes. For example, in the software-tool a maximum of two coplanar lines is possible. This leads to two possible propagating modes (A.3):

$$\underline{s}_0^{\text{common}} = \begin{bmatrix} 1 \\ 1 \end{bmatrix} \tag{A.3)a}$$

$$\underline{s}_0^{\text{differential}} = \begin{bmatrix} 1 \\ -1 \end{bmatrix} \tag{A.3)b}$$

Figure A.2 shows the electric field distribution for **a**) common mode excitation and **b**) differential mode excitation for a coupled microstrip resulting from the excitation as is described in Eq. (A.3).

With the defined excitation vector we will construct the EFIE and CMFIE form the boundary conditions of tangential components of the electric- and the magnetic fields. Since we want to analyze the magnetic- or electric currents flowing in the slot or on the strip, the equivalence theorem is applied where a closed surface, S, can be defined along the strip or slot. On this surface, the equivalent electric- ($\underline{j}_{eq}$) and magnetic- ($\underline{m}_{eq}$) currents are flowing according to the boundary conditions in Eq. (A.4).

$$\underline{\boldsymbol{j}}_{eq} = \hat{\boldsymbol{z}} \times (\underline{\boldsymbol{h}}^+ - \underline{\boldsymbol{h}}^-) \tag{A.4)a}$$

$$\underline{\boldsymbol{m}}_{eq} = -\hat{\boldsymbol{z}} \times (\underline{\boldsymbol{e}}^+ - \underline{\boldsymbol{e}}^-) \tag{A.4)b}$$

Outside the Δ-gap region for strip-type structures, the tangential electric field vanishes: $\hat{\boldsymbol{z}} \times \underline{\boldsymbol{e}}^+ = \hat{\boldsymbol{z}} \times \underline{\boldsymbol{e}}^- = 0$. Therefore $\underline{\boldsymbol{m}}_{eq} = 0$ and only $\underline{\boldsymbol{j}}_{eq}$ remains. For thin conductors, which is the

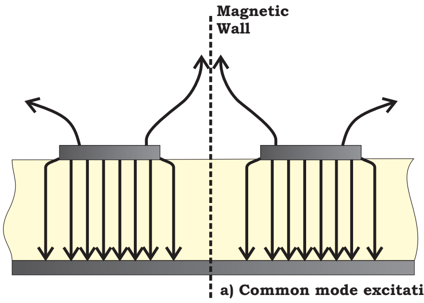

a) Common mode excitation

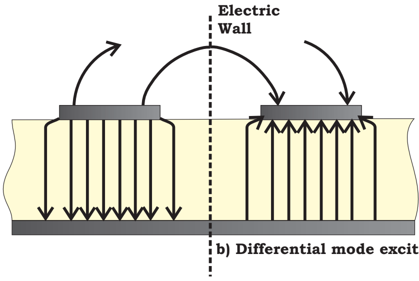

b) Differential mode excitation

Figure A.2: Electric field distribution for a) common mode excitation and b) differential mode excitation for a coupled microstrip.

case, we will have $\underline{j}'_{eq} = 2\underline{j}_{eq}$. For slots, the volume enclosed by the surface are conventionally filled with PEC short-circuiting the equivalent electric currents so that only equivalent magnetic currents are introduced. According to the image theorem we obtain $\underline{m}'_{eq} = 2\underline{m}_{eq}$. From this point, the equivalent current $\underline{c}_{eq}$ either denotes $\underline{j}'_{eq}$ or $\underline{m}'_{eq}$ for the equivalent electric or magnetic current respectively.

A.3 Spatial Integral Equations

After the equivalent currents are defined, we can combine both EFIE and CMFIE and enforce the continuity of the fields:

$$\hat{\boldsymbol{z}} \times \iint_S \underline{\underline{\tilde{\boldsymbol{g}}}}(x-x',y-y')\underline{\boldsymbol{c}}_{eq}(x',y')dx'dy' = \underline{\boldsymbol{s}}_{\Delta}(x,y) \tag{A.5}$$

where $\underline{s}_{\Delta}$ is the electric or magnetic excitation vector and $\underline{\boldsymbol{c}}_{eq}$ is the equivalent electric- ($\underline{\boldsymbol{j}}_{eq}$) or magnetic- ($\underline{\boldsymbol{m}}_{eq}$) currents for the EFIE or MFIE respectively. $\underline{\underline{\tilde{\boldsymbol{g}}}}(x-x',y-y')$ is the dyadic Green's function matrix in the spatial domain. The current distribution along the lines, $\underline{\boldsymbol{c}}_{eq}$, is considered to be separable in space-dependency (Eq. (A.6)),

$$\underline{\boldsymbol{c}}_{eq}(x,y) = \underline{c}_{eq}(x,y)\hat{\boldsymbol{x}} = \underline{c}_{x}(x,y)\underline{c}_{t}(y)\hat{\boldsymbol{x}} \tag{A.6}$$

with

$$c_{eq,i}(x,y) = c_{x,i}(x)c_t(y-id_y) \tag{A.7}$$

for $i = 0 : N-1$. The transverse current distribution $c_t(y)$ is assumed to be verifying the quasi-static edge singularities (Eq. (A.8)). This assumption is valid for $w_s << \lambda$.

$$c_t(y) = \frac{2}{w_s}\frac{1}{\sqrt{1-(\frac{2y}{w_s})^2}} \tag{A.8}$$

Using the identity $\underline{a}\times\underline{b}\times\underline{c}=\underline{b}(\underline{a}\cdot\underline{c})-\underline{c}(\underline{a}\cdot\underline{b})$ on Eq. (A.5), we have $\hat{\boldsymbol{z}}\times\hat{\boldsymbol{z}}\times\underline{a}=\hat{\boldsymbol{z}}(\hat{\boldsymbol{z}}\cdot\underline{a})-\underline{a}(\hat{\boldsymbol{z}}\cdot\hat{\boldsymbol{z}})$, where $\underline{a}=\iint_S\underline{\underline{\tilde{\boldsymbol{g}}}}(x-x',y-y')\underline{\boldsymbol{c}}_{eq}(x',y')dx'dy'$. Since $\underline{\boldsymbol{s}}_\Delta(x,y)=\underline{s}_\Delta(x,y)\hat{\boldsymbol{y}}$ is oriented along $\hat{\boldsymbol{y}}$, we can see that $\hat{\boldsymbol{z}}\cdot\underline{a}=0$. Also $\hat{\boldsymbol{z}}\cdot\hat{\boldsymbol{z}}=1$ so that we obtain Eq. (A.9).

$$\begin{aligned}\iint_S\underline{\underline{\tilde{\boldsymbol{g}}}}(x-x',y-y')\underline{\boldsymbol{c}}_{eq}(x',y')dx'dy'&=-\hat{\boldsymbol{z}}\times\underline{s}_\Delta(x,y)\hat{\boldsymbol{y}}\\&=\underline{s}_\Delta(x,y)\hat{\boldsymbol{x}}\end{aligned}\tag{A.9}$$

Observing that the right-hand side of Eq. (A.9) only has an $\hat{\boldsymbol{x}}$-component and the fact that the equivalent currents $\underline{\boldsymbol{c}}_{eq}(x,y)$ is also oriented along $\hat{\boldsymbol{x}}$ (A.6), only the $g_{xx}\hat{\boldsymbol{x}}$-component will be required of the dyadic Green's function matrix $\underline{\underline{\tilde{\boldsymbol{g}}}}$. This will make the integral equation a scalar problem and can therefore be rewritten into Eq. (A.10):

$$\iint_S\tilde{g}_{xx}(x-x',y-y')\underline{c}_{eq}(x',y')dx'dy'=\underline{s}_\Delta(x,y)\tag{A.10}$$

Eq. (A.10) comprises N equivalent currents, $\underline{c}_{eq}$, which are unknown and are equivalent to the fields radiated by the N different Δ-gap excitations, $\underline{s}_\Delta$. One Δ-gap excitation, $s_{\Delta,n}$, can therefore be expressed as a summation of reaction integrals of all equivalent currents due to this Δ-gap excitation and can be described as in Eq. (A.11):

$$\sum_{i=0}^{N-1}\iint_{S_i}\tilde{g}_{xx}(x-x',y-y')c_{eq,i}(x',y')dx'dy'=s_{\Delta,n}(x,y)\tag{A.11}$$

for $n=0:N-1$ and S_i, is the region of the ith strip or slot. Averaging the integral equations over the width of the strips or the slots brings us to our final expression for the Integral Equations for N coplanar lines in the spatial domain Eq. (A.12):

$$\boxed{\sum_{i=0}^{N-1}\frac{1}{w_s}\int_{w_{s,n}}\iint_{S_i}\tilde{g}_{xx}(x-x',y-y')c_{eq,i}(x',y')dx'dy'dy=\frac{1}{w_s}\int_{w_{s,n}}s_{\Delta,n}(x,y)dy}\tag{A.12}$$

for $n=0:N-1$.

A.4 Spectral Integral Equations

Substituting $s_{\Delta,n}(x,y)$ (A.2) and $c_{eq,i}$ (A.7) into our expression for the Integral Equations in the spatial domain (A.12) we obtain Eq. (A.13):

$$\begin{aligned}&\sum_{i=0}^{N-1}\frac{1}{w_s}\int_{w_{s,n}}\iint_{S_i}\tilde{g}_{xx}(x-x',y-y')c_{x,i}(x')c_t(y'-id_y)dx'dy'dy\\&\qquad=\frac{1}{w_s}\int_{w_{s,n}}s_{0,n}\cdot\mathrm{rect}\left(\frac{x}{\Delta}\right)\mathrm{rect}\left(\frac{y-nd_y}{w_s}\right)dy\\&\qquad=s_{0,n}\cdot\mathrm{rect}\left(\frac{x}{\Delta}\right)\end{aligned}\tag{A.13}$$

for $n=0:N-1$. A convolution in the spatial domain, which the IE of Eq. (A.13) is in fact representing, is equal to a multiplication in the spectral domain. We can therefore express Eq. (A.13) in terms of inverse Fourier transforms. Using the Fourier transforms in Eq. (A.14), and the shifts property of the Fourier Transform (A.15) we obtain the IE in terms of anti-Fourier transforms Eq. (A.16).

$$\tilde{g}_{xx}(x,y) \xrightarrow{\mathcal{F}} \tilde{G}_{xx}(k_x,k_y) \tag{A.14)a}$$

$$c_{x,i}(x) \xrightarrow{\mathcal{F}} C_{x,i}(k_x) \tag{A.14)b}$$

$$c_t(y) = -\frac{2}{w_s\pi}\frac{1}{\sqrt{1-\left(\frac{2y}{w_s}\right)^2}} \xrightarrow{\mathcal{F}} C_t(k_y) = -J_0\left(\frac{k_x w_s}{2}\right) \tag{A.14)c}$$

$$n_{0,n}(x) = s_{0,n}\cdot \mathrm{rect}\left(\frac{x}{\Delta}\right) \xrightarrow{\mathcal{F}} N_{0,n}(k_x) = s_{0,n}\cdot \mathrm{sinc}\left(\frac{k_x\Delta}{2}\right) \tag{A.14)d}$$

$$c_t(y-id_y) \xrightarrow{\mathcal{F}} C_t(k_y)e^{-jk_y id_y} \tag{A.15}$$

$$\begin{aligned}\left(\frac{1}{2\pi}\right)^2\sum_{i=0}^{N-1}\frac{1}{w_s}\int_{w_s,n}\int_{-\infty}^{\infty}\int_{-\infty}^{\infty}\tilde{G}_{xx}(k_x,k_y)C_{x,i}(k_x)C_t(k_y)e^{-jk_xx}e^{-jk_yy}e^{-jk_yid_y}dk_xdk_ydy\\ =\frac{1}{2\pi}\int_{-\infty}^{\infty}N_{0,n}(k_x)e^{-jk_xx}dk_x\end{aligned} \tag{A.16}$$

for $n = 0 : N-1$, The integral $\int_{w_{s,n}}\cdots dy$, responsible for the averaging of the fields over the width of the strip or slot, on the left-hand side of the integral equation (A.13) is equivalent to the integration $\int_{-\infty}^{\infty}\cdots\mathrm{rect}(\frac{y+nd_y}{w_s})dy$ so that Eq. (A.16) becomes:

$$\begin{aligned}\left(\frac{1}{2\pi}\right)^2\sum_{i=0}^{N-1}\frac{1}{w_s}\int_{-\infty}^{\infty}\int_{-\infty}^{\infty}\int_{-\infty}^{\infty}\tilde{G}_{xx}(k_x,k_y)C_{x,i}(k_x)C_t(k_y)\mathrm{rect}\left(\frac{y+nd_y}{w_s}\right)e^{-jk_xx}e^{-jk_yy}\dots\\ \cdots e^{-jk_yid_y}dk_xdk_ydy=\frac{1}{2\pi}\int_{-\infty}^{\infty}N_{0,n}(k_x)e^{-jk_xx}dk_x\end{aligned} \tag{A.17}$$

for $n = 0 : N-1$. The integral in y can be solved using (A.18), where the time shift property of a Fourier transform, as in (A.15), is also used and will result in (A.19).

$$\frac{1}{w_s}\int_{-\infty}^{\infty}\mathrm{rect}\left(\frac{y+nd_y}{w_s}\right)e^{-jk_yy}dy = \mathrm{sinc}\left(\frac{k_yw_s}{2}\right)e^{jk_ynd_y} \tag{A.18}$$

$$\begin{aligned}\left(\frac{1}{2\pi}\right)^2\sum_{i=0}^{N-1}\int_{-\infty}^{\infty}\int_{-\infty}^{\infty}\tilde{G}_{xx}(k_x,k_y)C_{x,i}(k_x)C_t(k_y)\mathrm{sinc}\left(\frac{k_yw_s}{2}\right)e^{-jk_xx}\dots\\ \cdots e^{-jk_y(i-n)d_y}dk_xdk_y=\frac{1}{2\pi}\int_{-\infty}^{\infty}N_{0,n}(k_x)e^{-jk_xx}dk_x\end{aligned} \tag{A.19}$$

for $n = 0 : N-1$. Rearranging the terms in order to define the space-convolution integral $D(k_x)$:

$$\frac{1}{2\pi}\sum_{i=0}^{N-1}\int_{-\infty}^{\infty}\left(\frac{1}{2\pi}\int_{-\infty}^{\infty}\tilde{G}_{xx}(k_x,k_y)C_t(k_y)\mathrm{sinc}\left(\frac{k_y w_s}{2}\right)e^{-jk_y(i-n)d_y}dk_y\right)C_{x,i}(k_x)e^{-jk_x x}dk_x$$
$$=\frac{1}{2\pi}\int_{-\infty}^{\infty}N_{0,n}(k_x)e^{-jk_x x}dk_x \tag{A.20}$$

for $n=0:N-1$. In Eq. (A.20), the integral inside the parenthesis will be defined as $D_{n,i}(k_x)$:

$$D_{n,i}(k_x)=\frac{1}{2\pi}\int_{-\infty}^{\infty}\tilde{G}_{xx}(k_x,k_y)C_t(k_y)\mathrm{sinc}\left(\frac{k_y w_s}{2}\right)e^{-jk_y(i-n)d_y}dk_y \tag{A.21}$$

Our final expression for the Integral Equations in the spectral domain is now (A.22):

$$\boxed{\frac{1}{2\pi}\sum_{i=0}^{N-1}\int_{-\infty}^{\infty}D_{n,i}(k_x)C_{x,i}(k_x)e^{-jk_x x}dk_x=\frac{1}{2\pi}\int_{-\infty}^{\infty}N_{0,n}(k_x)e^{-jk_x x}dk_x} \tag{A.22}$$

for $n=0:N-1$.

A.5 Longitudinal electric- and magnetic currents

Equating the integrands brings us the following relationship:

$$\sum_{i=0}^{N-1}D_{n,i}(k_x)C_{x,i}(k_x)=N_{0,n}(k_x) \tag{A.23}$$

And in matrix form:

$$\begin{aligned}\underline{\underline{D}}(k_x)\cdot\underline{C}_x(k_x) &= \underline{N}_0(k_x) && \text{(A.24)a}\\ \underline{C}_x(k_x) &= \underline{\underline{D}}^{-1}(k_x)\cdot\underline{N}_0(k_x) && \text{(A.24)b}\end{aligned}$$

Conclusively, the electric or magnetic currents can be expressed as an inverse Fourier transform of its current spectrum in Eq. (A.24)b:

$$\boxed{\underline{c}_x(x)=\frac{1}{2\pi}\int\underline{\underline{D}}^{-1}(k_x)\cdot\underline{N}_0(k_x)e^{-jk_x x}dk_x} \tag{A.25}$$

with:

$$\begin{aligned}N_{0,n}(k_x) &= s_{0,n}\mathrm{sinc}\left(\frac{k_x\Delta}{2}\right) && \text{(A.26)}\\ D_{n,i}(k_x) &= \frac{1}{2\pi}\int\tilde{G}_{xx}(k_x,k_y)C_t(k_y)\mathrm{sinc}\left(\frac{k_y w_s}{2}\right)e^{-jk_y(i-n)d_y}dk_y && \text{(A.27)}\\ C_t(k_y) &= -J_0\left(\frac{k_x w_s}{2}\right) && \text{(A.28)}\end{aligned}$$

This formulation is also known as the transmission lie formalism. Extracting the singularity from the current spectrum associated to the main propagating mode along the transmission line (i.e. solving the dispersion equation) from the basis of this quasi-analytical model.

Appendix B

Integral Equation with conductor losses for strip-type structures

In this appendix, the integral equations constructed in Appendix A will be expanded in order to include conductor losses for strip-type structures. The conductor losses for the main conductor of a strip-type transmission line are accounted for by means of a surface impedance boundary condition. We will start by imposing the EFIE on a lossy conductor which will give rise to a non-zero tangential total electric field. The total electric field can then be related to the strip's surface impedance and current along the line. Accounting for the ohmic losses in the metal leads finally to a new denominator for the strip $\underline{\underline{\tilde{D}}}(k_x)$.

We will start from the initial expression for the EFIE as in Eq. (B.1)

$$\underline{\boldsymbol{e}}_{scatt}(x,y) = -\underline{\boldsymbol{m}}_{\Delta}(x,y) + \underline{\boldsymbol{e}}_{tot}(x,y) \tag{B.1}$$

In (B.1), $\underline{\boldsymbol{e}}_{scatt}$ and $\underline{\boldsymbol{m}}_{\Delta}$ are the tangential components of the scattered electric field and incident field respectively. The incident field is characterized by a Δ-gap excitation. In Eq. (B.5), the tangential total electric field $\underline{\boldsymbol{e}}_{tot}$ is equal to zero, which is only the case for perfect electric conductors. However, in the case of conductor losses, the total electric field will be related to the strip's surface impedance and current along the line as is described in Eq. (B.2)

$$\underline{\boldsymbol{e}}_{tot}(x,y) = Z_{strip}(y)\underline{\boldsymbol{j}}_{eq}(x,y) \tag{B.2}$$

In this appendix we will start by investigating this surface impedance $Z_{strip}(y)$ and reformulate the transmission line formalism as in Eq. (A.25).

B.1 Surface impedance

It makes sense to define $Z_{strip}(y)$ with the high-frequency surface impedance Z_s (B.3).

$$Z_s = (1+j)\sqrt{\frac{k_0\zeta_0}{2\sigma}} \tag{B.3}$$

However, this constant surface impedance does not really make sense when looking at the shape of the transverse fields in (B.1) as is shown in Figure B.1. The scattered electric field ($\underline{\boldsymbol{e}}_{scatt}$) and the incident electric field ($\underline{\boldsymbol{m}}_{\Delta}$) will have a rectangular shape. The total electric field is given by (B.2). When Z_{strip} is assumed to be the high-frequency surface impedance Z_s, the multiplication with the equivalent electric current $\underline{\boldsymbol{j}}_{eq}$ will result in an electric field in the form of the quasi-static edge singularity function $j_t(y)$. It makes sense to define Z_{strip} proportional to

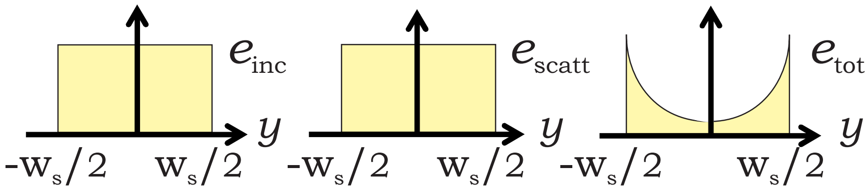

Figure B.1: Tangential electric field components from the Electric Field Integral Equations; $e_{inc} = m_\Delta$, e_{scatt} and $e_{tot} = Z_s j_{eq}$

the inverse of the quasi-static edge singularity function as is shown in (B.4) and demonstrated in [18].

$$Z_{strip} = Z_s\sqrt{1-\left(\frac{2y}{w_s}\right)^2} \tag{B.4}$$

B.2 Integral Equation

Substituting the non-zero tangential component of the electric field (B.2) in our final expression of the EFIE for N coplanar lines in the spatial domain from Eq. (A.12) we obtain Eq. (B.5).

$$\begin{aligned}\sum_{i=0}^{N-1}\frac{1}{w_s}\int_{w_{s,n}}\iint_{S_i}\tilde{g}_{xx}(x-x',y-y')j_{eq,i}(x',y')dx'dy'dy\\ =\frac{1}{w_s}\int_{w_{s,n}}\left[m_{\Delta,n}(x,y)+Z_{strip}(y)j_{eq,n}(x,y)\right]dy\end{aligned} \tag{B.5}$$

for $n = 0 : N-1$. The excitation and equivalent currents in the spatial integral equation in Eq. (B.5) can be expanded resulting in Eq. (B.6).

$$\begin{aligned}&\sum_{i=0}^{N-1}\frac{1}{w_s}\int_{w_{s,n}}\iint_{S_i}\tilde{g}_{xx}(x-x',y-y')j_{x,i}(x')j_t(y'-id_y)dx'dy'dy\\ &=\frac{1}{w_s}\int_{w_{s,n}}\left[s_{0,n}\cdot\mathrm{rect}\left(\frac{x}{\Delta}\right)\mathrm{rect}\left(\frac{y-nd_y}{w_s}\right)+Z_{strip}(y-nd_y)j_{x,n}(x)j_t(y-nd_y)\right]dy\\ &=\frac{1}{w_s}\int_{w_{s,n}}\left[s_{0,n}\cdot\mathrm{rect}\left(\frac{x}{\Delta}\right)-Z_s\frac{2}{w_s\pi}j_{x,n}(x)\right]dy\end{aligned} \tag{B.6}$$

for $n = 0 : N-1$. In the last step, we made use of the fact that

$$\begin{aligned}Z_{strip}(y)j_t(y) &= Z_s\sqrt{1-\left(\frac{2y}{w_s}\right)^2}\cdot-\frac{2}{w_s\pi}\frac{1}{\sqrt{1-\left(\frac{2y}{w_s}\right)^2}}\\ &=-Z_s\frac{2}{w_s\pi}\end{aligned}$$

Making the same steps as in Appendix A, Eq. (B.6) can be expressed in terms of inverse Fourier transforms after which we obtain Eq. (B.7)

$$\begin{aligned}\left(\frac{1}{2\pi}\right)^2 \sum_{i=0}^{N-1} \frac{1}{w_s}\int_{w_s}\int_{-\infty}^{\infty}\int_{-\infty}^{\infty} \tilde{G}_{xx}(k_x,k_y)J_{x,i}(k_x)J_t(k_y)e^{-jk_xx}e^{-jk_yy}e^{-jk_yid_y}dk_xdk_ydy \\ = \frac{1}{w_s}\int_{w_{s,n}}\frac{1}{2\pi}\int_{-\infty}^{\infty}\left[N_{0,n}(k_x) - Z_s\frac{2}{w_s\pi}J_{x,n}(k_x)\right]e^{-jk_xx}dk_xdy\end{aligned} \tag{B.7}$$

for $n = 0 : N-1$. As in Appendix A, closing the integral in y and defining the transverse integral $D_{n,i}(k_x)$, Eq. (B.7) can be simplified to our final expression for the Integral Equation for N coplanar conductors in the spectral domain. This final spectral Integral Equation is shown in Eq. (B.8) for $n = 0 : N-1$.

$$\boxed{\frac{1}{2\pi}\sum_{i=0}^{N-1}\int_{-\infty}^{\infty} D_{n,i}(k_x)C_{x,i}(k_x)e^{-jk_xx}dk_x = \frac{1}{2\pi}\int_{-\infty}^{\infty}\left[N_{0,n}(k_x) - Z_s\frac{2}{w_s\pi}J_{x,n}(k_x)\right]e^{-jk_xx}dk_x} \tag{B.8}$$

for $n = 0 : N-1$.

B.3 Longitudinal electric current

Proceeding by equating the integrands of Eq. (B.8) and bringing the loss component $Z_s\frac{2}{w_s\pi}J_{x,n}(k_x)$ to the left-hand side of the equation results in::

$$\sum_{i=0}^{N-1} D_{n,i}(k_x)J_{x,i}(k_x) = N_{0,n}(k_x) - Z_s\frac{2}{w_s\pi}J_{x,n}(k_x) \tag{B.9}$$

$$\sum_{i=0}^{N-1} D_{n,i}(k_x)J_{x,i}(k_x) + Z_s\frac{2}{w_s\pi}J_{x,n}(k_x) = N_{0,n}(k_x) \tag{B.10}$$

for $n = 0 : N-1$. And in matrix form, these former expressions will be equivalent to:

$$\underline{\underline{D}}(k_x)\cdot\underline{J}_x(k_x) + Z_s\frac{2}{w_s\pi}\underline{\underline{I}}_N\underline{J}_x(k_x) = \underline{N}_0(k_x) \tag{B.11)a}$$

$$\left(\underline{\underline{D}}(k_x) + Z_s\frac{2}{w_s\pi}\underline{\underline{I}}_N\right)\cdot\underline{J}_x(k_x) = \underline{N}_0(k_x) \tag{B.11)b}$$

$$\underline{J}_x(k_x) = \left(\underline{\underline{D}}(k_x) + Z_s\frac{2}{w_s\pi}\underline{\underline{I}}_N\right)^{-1}\cdot\underline{N}_0(k_x) \tag{B.11)c}$$

As we can see, accounting for the ohmic losses in the conductors leads to a new denominator for the strip (B.12), where $\underline{\underline{I}}_N$ is a $N \times N$ identity matrix.

$$\underline{\underline{D}}_{loss}(\underline{k}_x) = \underline{\underline{D}}(\underline{k}_x) + Z_s\frac{2}{w_s\pi}\underline{\underline{I}}_N \tag{B.12}$$

Substituting Eq. (B.12) into Eq. (B.11)c leads to Eq. (B.13):

$$\underline{J}_x(k_x) = \underline{\underline{D}}_{loss}(k_x)^{-1}\cdot\underline{N}_0(k_x) \tag{B.13}$$

Conclusively, the electric currents, expressed as an inverse Fourier transform are:

$$\boxed{\underline{j}_x(x) = \frac{1}{2\pi}\int\underline{\underline{D}}_{loss}^{-1}(k_x)\cdot\underline{N}_0(k_x)e^{-jk_xx}dk_x} \tag{B.14}$$

with:

$$N_{0,n}(k_x) = s_{0,n}\text{sinc}\left(\frac{k_x\Delta}{2}\right) \tag{B.15}$$

$$C_t(k_y) = -J_0\left(\frac{k_x w_s}{2}\right) \tag{B.16}$$

$$D^{loss}_{n,i}(k_x) = \frac{1}{2\pi}\int \tilde{G}_{xx}(k_x,k_y)J_t(k_y)\text{sinc}\left(\frac{k_y w_s}{2}\right)e^{-jk_y(i-n)d_y}dk_y \qquad \text{for } n \neq i \tag{B.17}$$

$$D^{loss}_{n,i}(k_x) = \frac{1}{2\pi}\int \tilde{G}_{xx}(k_x,k_y)J_t(k_y)\text{sinc}\left(\frac{k_y w_s}{2}\right)e^{-jk_y(i-n)d_y}dk_y + Z_s\frac{2}{w_s\pi} \qquad \text{for } n = i \tag{B.18}$$

Appendix C

Green's functions for various printed transmission lines

In this chapter we will show the derivation of the Green's functions of several printed transmission lines of interest. We will start from the Green's function components used in the integral equation constructed in chapter 3.

C.1 Green's Functions

In chapter 3 it became clear that the integral equation can be expressed in its scalar form; only the *xx*-components of the Green's functions are needed. We ended with the spectral Green's functions of an electric or magnetic source oriented along $\underline{\hat{x}}$ [18]:

$$G_{xx}^{EJ} = -\frac{v_{TM}^{J}k_x^2 + v_{TE}^{J}k_y^2}{k_\rho^2} \tag{C.1)a}$$

$$G_{xx}^{HM} = -\frac{i_{TE}^{M}k_x^2 + i_{TM}^{M}k_y^2}{k_\rho^2} \tag{C.1)b}$$

In these expressions, $v_{TE/TM}$ and $i_{TE/TM}$ are the voltages and currents along the equivalent transmission line structures representing the TE or TM modes. These equivalent transmission lines will be evaluated in the next two sections.

C.2 Single transmission lines

In this section we will derive the expressions for the spectral Green's functions for single transmission lines in a plane-stratified media problem. In these problems four possible stratifications are considered:

1. An infinite <u>top medium</u>
2. A finite <u>upper slab</u>
3. A finite <u>lower slab</u>
4. An infinite <u>bottom medium</u>

These stratifications all have their specific relative permittivity ε_r and can also be specified by a specific loss tangent δ representing the dielectric losses. As we have four stratifications, the

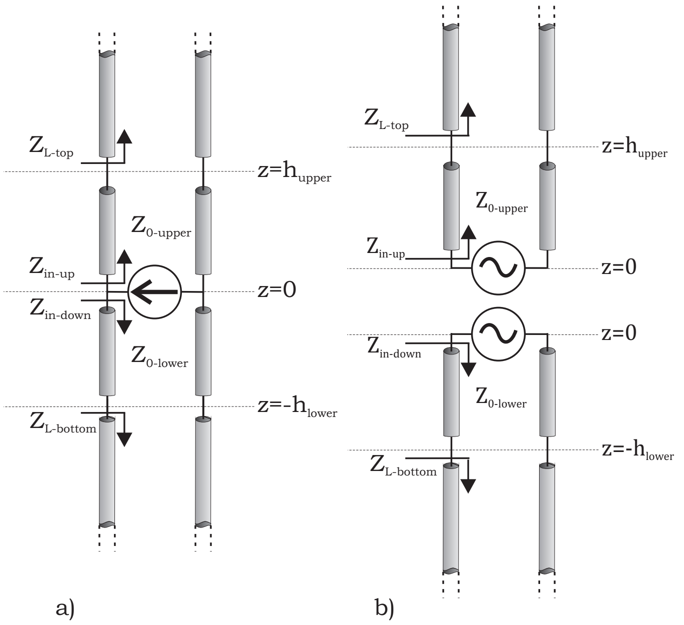

Figure C.1: General equivalent transmission line models for a) an electric source and b) a magnetic source.

equivalent transmission line model contains four transmission lines. The equivalent transmission line circuits for an electric and magnetic source are depicted in Figure C.1a) and Figure C.1b) respectively.

C.2.1 Strip

Both top and bottom media are infinite, these transmission lines can therefore be characterized as loads connected to the finite transmission lines representing the upper and the bottom slabs. The equivalent transmission line circuit for a strip is shown in Figure C.2.

$$Z_{L_{bottom}}^{TE} = \frac{\zeta_0}{\sqrt{\varepsilon_{r_{bottom}}}}\frac{k_{bottom}}{k_{z_{bottom}}} \qquad Z_{L_{bottom}}^{TM} = \frac{\zeta_0}{\sqrt{\varepsilon_{r_{bottom}}}}\frac{k_{z_{bottom}}}{k_{bottom}} \qquad \text{(C.2)a}$$

$$Z_{L_{top}}^{TE} = \frac{\zeta_0}{\sqrt{\varepsilon_{r_{top}}}}\frac{k_{top}}{k_{z_{top}}} \qquad Z_{L_{top}}^{TM} = \frac{\zeta_0}{\sqrt{\varepsilon_{r_{top}}}}\frac{k_{z_{top}}}{k_{top}} \qquad \text{(C.2)b}$$

The upper and lower slabs can be characterized as transmission lines. Characteristic impedances of these transmission lines, depending on the type of dielectric can be calculated as:

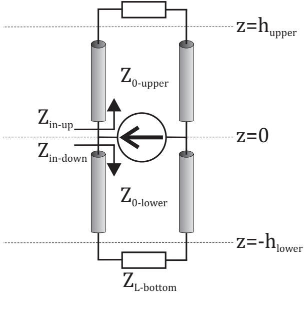

Figure C.2: Equivalent transmission line model for a strip

$$Z^{TE}_{0_{upper}} = \frac{\zeta_0}{\sqrt{\varepsilon_{r_{upper}}}} \frac{k_{upper}}{k_{z_{upper}}} \qquad Z^{TM}_{0_{upper}} = \frac{\zeta_0}{\sqrt{\varepsilon_{r_{upper}}}} \frac{k_{z_{upper}}}{k_{upper}} \tag*{(C.2)c}$$

$$Z^{TE}_{0_{lower}} = \frac{\zeta_0}{\sqrt{\varepsilon_{r_{lower}}}} \frac{k_{lower}}{k_{z_{lower}}} \qquad Z^{TM}_{0_{lower}} = \frac{\zeta_0}{\sqrt{\varepsilon_{r_{lower}}}} \frac{k_{z_{lower}}}{k_{lower}} \tag*{(C.2)d}$$

from these characteristic impedances, we can calculate the input impedances looking from the source to the upper and lower half of the structure:

$$Z^{TE/TM}_{in_{up}} = Z^{TE/TM}_{0_{upper}} \frac{Z^{TE/TM}_{L_{top}} + Z^{TE/TM}_{0_{upper}} \tanh\left(jk^{TE/TM}_{z_{top}} h_{upper}\right)}{Z^{TE/TM}_{0_{upper}} + Z^{TE/TM}_{L_{top}} \tanh\left(jk^{TE/TM}_{z_{top}} h_{upper}\right)} \tag*{(C.2)e}$$

$$Z^{TE/TM}_{in_{down}} = Z^{TE/TM}_{0_{lower}} \frac{Z^{TE/TM}_{L_{bottom}} + Z^{TE/TM}_{0_{lower}} \tanh\left(jk^{TE/TM}_{z_{bottom}} h_{lower}\right)}{Z^{TE/TM}_{0_{lower}} + Z^{TE/TM}_{L_{bottom}} \tanh\left(jk^{TE/TM}_{z_{bottom}} h_{lower}\right)} \tag*{(C.2)f}$$

Note that inside the tanh, a j is implemented. This is due to our definition of the propagation constant, which is $k = \beta + j\alpha'$. Multiply k with j to obtain the conventional propagation constant: $\gamma = jk = -\alpha' + j\beta = \alpha + j\beta$ as is being used in Pozar [20].

Using these input impedances for the upper and lower half of the structure we can calculate v^J_{TE} and v^J_{TM}:

$$v^J_{TE} = \frac{Z^{TE}_{in_{up}} Z^{TE}_{in_{down}}}{Z^{TE}_{in_{up}} + Z^{TE}_{in_{down}}} \tag*{(C.3)}$$

$$v^J_{TM} = \frac{Z^{TM}_{in_{up}} Z^{TM}_{in_{down}}}{Z^{TM}_{in_{up}} + Z^{TM}_{in_{down}}} \tag*{(C.4)}$$

which can be substituted in Eq. (C.1)a.

C.2.2 Microstrip

The microstrip is one of the most commonly used transmission lines. The main difference between a microstrip and the strip in the previous subsection is the ground plane beneath the dielectric. This results in the fact that the transmission line, which is representing the lower slab, can be short circuited rather than connected to the characteristic impedance of the infinite bottom medium. This short-circuit is only valid when the ground plane is lossless, in the case of a ground plane with finite conductivity the short-circuit can be replaced by a load characterized by the high-frequency surface impedance. The equivalent transmission line circuit is shown in Figure C.3.

The top medium is infinite, this transmission line can therefore be characterized as a load connected to the finite transmission line representing the upper slab. As explained, the ground plane simulates a short-circuit:

$$Z^{TE}_{L_{bottom}} = 0 \qquad Z^{TM}_{L_{bottom}} = 0 \tag*{(C.5)a}$$

$$Z^{TE}_{L_{top}} = \frac{\zeta_0}{\sqrt{\varepsilon_{r_{top}}}} \frac{k_{top}}{k_{z_{top}}} \qquad Z^{TM}_{L_{top}} = \frac{\zeta_0}{\sqrt{\varepsilon_{r_{top}}}} \frac{k_{z_{top}}}{k_{top}} \tag*{(C.5)b}$$

The slabs can be characterized as transmission lines with a specific characteristic impedance in the same way as with the strip. From these characteristic impedances, together with Eq. (C.2)e

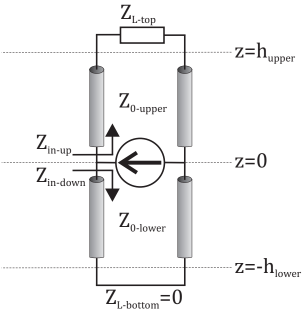

Figure C.3: Equivalent transmission line model for a microstrip

and Eq. (C.2)f, we can calculate the input impedances looking from the source to the upper and lower half of the structure:

$$Z_{in_{up}}^{TE/TM} = Z_{0_{upper}}^{TE/TM} \frac{Z_{L_{top}}^{TE/TM} + Z_{0_{upper}}^{TE/TM} \tanh\left(jk_{z_{top}}^{TE/TM} h_{upper}\right)}{Z_{0_{upper}}^{TE/TM} + Z_{L_{top}}^{TE/TM} \tanh\left(jk_{z_{top}}^{TE/TM} h_{upper}\right)} \qquad \text{(C.5)c}$$

$$Z_{in_{down}}^{TE/TM} = Z_{0_{lower}}^{TE/TM} \tanh\left(jk_{z0_{lower}} h_{lower}\right) \qquad \text{(C.5)d}$$

Using these input impedances for the upper and lower half of the structure we can calculate v_{TE}^{J} and v_{TM}^{J} by substituting them into Eq. (C.3) and Eq. (C.4). From v_{TE}^{J} and v_{TM}^{J} the Green's function in Eq. (C.1)a can be calculated.

C.2.3 Stripline

The stripline is less popular than the microstrip as a printed transmission line but can be used when shielding from external EM-sources is of importance. This is because the strip has both below and above ground planes. Now not only the transmission line representing the lower slab is short circuited but also the transmission line representing the upper slab is short-circuited. Again, we assume the ground plane to be a perfect electric conductor. The equivalent transmission line circuit for a stripline is shown in Figure C.4.

In this case both the transmission lines representing the upper and lower slabs are short circuited because of the two ground planes.

$$Z_{L_{bottom}}^{TE} = 0 \qquad Z_{L_{bottom}}^{TM} = 0 \qquad \text{(C.6)a}$$

$$Z_{L_{top}}^{TE} = 0 \qquad Z_{L_{top}}^{TM} = 0 \qquad \text{(C.6)b}$$

The input impedances looking from the source to the upper and lower half of the structure are now:

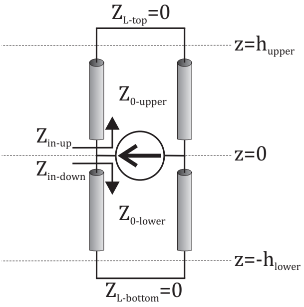

Figure C.4: Equivalent transmission line model for a stripline

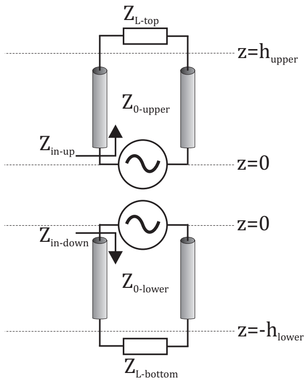

Figure C.5: Equivalent transmission line model for a slotline

$$Z_{in_{up}}^{TE/TM} = Z_{0_{upper}}^{TE/TM} \tanh\left(jk_{z_{upper}} h_{upper}\right) \tag{C.6)c}$$

$$Z_{in_{down}}^{TE/TM} = Z_{0_{lower}}^{TE/TM} \tanh\left(jk_{z_{lower}} h_{lower}\right) \tag{C.6)d}$$

Again, we use Eq. (C.3), Eq. (C.4) and Eq. (C.1)a to calculate the Green's function.

C.2.4 Slotline

The slotline can be considered as the reciprocal of the strip. The slotline itself is not considered to be a good transmission line as it could be highly radiative. It will behave as an antenna and is therefore also useful to include in this quasi-analytical model. However, two slotlines next two each other will be a CPW and that is a transmission line widely used.

As with the strip, both top and bottom media are infinite. The input impedances looking from the source to the upper and lower half of the structure are exactly the same as with the strip (See Eq. (C.2)). However, the two half planes are completely separated resulting in a summation of the Green's function in the upper half plane and the Green's function in the lower half plane. The equivalent transmission line circuit of a slotline is shown in Figure C.5. Using these input impedances for the upper and lower half of the structure we can calculate i_{TE}^{M} and i_{TM}^{M}:

$$i_{TE}^{M_{down}} = \frac{1}{Z_{in_{down}}^{TE}} \qquad i_{TM}^{M_{down}} = \frac{1}{Z_{in_{down}}^{TM}} \tag{C.7)a}$$

$$i_{TE}^{M_{up}} = \frac{1}{Z_{in_{up}}^{TE}} \qquad i_{TM}^{M_{up}} = \frac{1}{Z_{in_{up}}^{TM}} \tag{C.7)b}$$

Substituting Eq. (C.7) in Eq. (C.1)b gives us the Green's function of the slotline:

$$G_{xx}^{HM} = -\frac{i_{TE}^{M_{down}} k_x^2 + i_{TM}^{M_{down}} k_y^2}{k_\rho^2} - \frac{i_{TE}^{M_{up}} k_x^2 + i_{TM}^{M_{up}} k_y^2}{k_\rho^2} \tag{C.8}$$

C.3 Multiple transmission lines in parallel

The power of using the Green's function is that we can use exact the same dyadic as for the single transmission lines. In fact, the Green's functions are a description of the stratifications in absence of the strip or slot. All the changes in relation to the single transmission line can be defined in the denominator $D(k_x)$ and the excitation coefficients in $N_0(k_x)$.

C.4 Ohmic losses in the stratification

Ohmic losses in the stratification of printed transmission lines can directly be integrated in the transmission line Green's functions. Dielectric losses are modeled with a complex relative permittivity, defined from a loss tangent as is described in subsection 3.5.1.

Furthermore conductor losses in any ground-planes can be present. Previously, the ground-planes were modeled as a short-circuit, representing a PEC. In the case that these ground-planes are not perfectly electrically conducting, they can be modeled with a load characterized by the high-frequency surface-impedance. An example is given in Figure C.6a where the transmission line representing the lower dielectric slab is now closed with the load Z_s; the high-frequency surface-impedance.

In subsection 3.5.2 it is explained that the losses in the main ground-planes of slot-type transmission lines can be characterized by means of the high-frequency surface-impedance in series with the stratification. An example is shown in Figure C.6b.

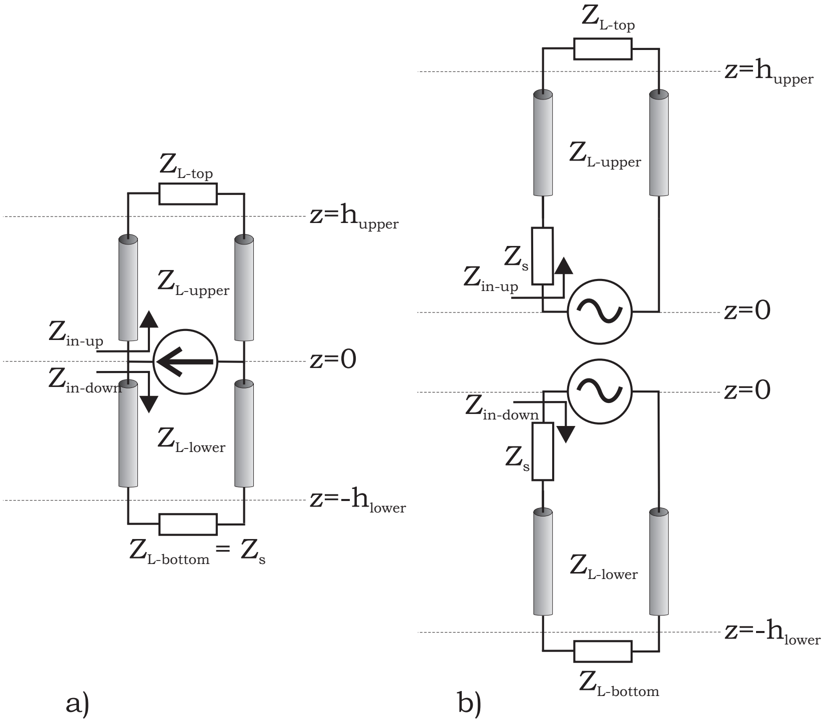

Figure C.6: Equivalent transmission line models for a) a lossy microstrip and b) a lossy slotline.

Appendix D

Calculating residues

As is explained in Section 3.2, some integrations paths require to add the residue of a certain pole in the current spectrum. More specifically, as is discussed, when $k_x < k_{SFW}$ a surface-wave or leaky-wave will be excited and the associate pole of the surface-wave mode in the transverse spectral plane should be included in the integration path. The inclusion of the pole is accounted for by, instead of only integrating over the real axis $-\infty < k_y < \infty$, also adding the residues of the poles $\pm k_{y,SFW}$ in the k_y domain. As these poles are located in the transverse spectral plane, the residues should be calculated in the k_y-domain. Another situation where the residue should be calculated is when the current contribution of a specific propagation mode is investigated. The total current calculated by following the integration path C_x in Figure 3.5 encloses all the contributions of all propagating modes in the transmission line while calculating the residue in k_x only accounts for the specific contribution of this mode. This propagating mode is located in the longitudinal spectral plane and therefore the residue should be calculated in the k_x-domain. In this chapter the method of calculating the residues in k_x and k_y will be elaborated.

D.1 Residue in the longitudinal spectral plane

As explained, the electric or magnetic currents, $\underline{c}(x)$, can be expressed as an inverse Fourier transform in the longitudinal domain of the lines (D.1):

$$\underline{c}(x) = \frac{1}{2\pi}\int_{-\infty}^{\infty} \underline{\underline{D}}^{-1}(k_x) \cdot \underline{N}_0(k_x) e^{-jk_x x} dk_x \tag{D.1}$$

In this equation we have the denominator $\underline{\underline{D}}(k_x)$ representing the average transverse electric or magnetic field on the strip or slot, radiated by the equivalent currents. $\underline{N}_0(k_x)$ is the Fourier transform of the longitudinal excitation law which can be expressed as a multiplication of the excitation coefficients and longitudinal excitation field. The inverse matrix $\underline{\underline{D}}^{-1}(k_x)$ can be represented as

$$\underline{\underline{D}}^{-1}(k_x) = \frac{\underline{\underline{A}}(k_x)}{|\underline{\underline{D}}(k_x)|} \tag{D.2}$$

where

$$\begin{array}{lll} \underline{\underline{A}}(k_x) & \text{is the adjugate of } \underline{\underline{D}}(k_x) & \text{(D.3)a} \\ |\underline{\underline{D}}(k_x)| & \text{is the determinant of } \underline{\underline{D}}(k_x) & \text{(D.3)b} \end{array}$$

When this decomposition (D.2) is substituted in, (D.4) we obtain:

$$\underline{c}(x) = \frac{1}{2\pi}\int_{-\infty}^{\infty} \frac{\underline{\underline{A}}(k_x)}{|\underline{\underline{D}}(k_x)|} \cdot \underline{N}_0(k_x) e^{-jk_x x} dk_x \tag{D.4}$$

Evaluating the current for the propagating modes $\underline{k}_{mode}$ can therefore be performed by applying the residue theorem to (D.4):

$$\underline{c}_{mode}(x) = -\frac{1}{2\pi} 2\pi j \underline{\text{Res}}(\underline{k}_{mode}) e^{-j\underline{k}_{mode}x}\hat{\boldsymbol{x}} \tag{D.5}$$

where:

$$\underline{\text{Res}}(\underline{k}_{mode}) = \frac{\underline{\underline{A}}(\underline{k}_{mode})}{|\underline{\underline{D}}(\underline{k}_{mode})|'} \cdot \underline{N}_0(\underline{k}_{mode}) \tag{D.6}$$

In order to solve this residue, the inverse of the current spectrum (D.7) will be used (D.8):

$$\underline{C}(k_x) = \underline{\underline{D}}^{-1}(k_x) \cdot \underline{N}_0(k_x) = \frac{\underline{\underline{A}}(k_x)}{|\underline{\underline{D}}(k_x)|} \cdot \underline{N}_0(k_x) \tag{D.7}$$

$$\underline{F}(k_x) = \underline{C}^{-1}(k_x) \tag{D.8}$$

Taking the first derivative we arrive at (D.9):

$$\underline{F}'(k_x) = -\underline{C}^{-2}(k_x)\underline{C}'(k_x) \tag{D.9}$$

where

$$\underline{C}^{-2}(k_x) = \frac{(\underline{\underline{A}}(k_x) \cdot \underline{N}_0(k_x))^{-2}}{|\underline{\underline{D}}(k_x)|^{-2}} \tag{D.10)a}$$

$$\underline{C}'(k_x) = \frac{(\underline{\underline{A}}(k_x) \cdot \underline{N}_0(k_x))'|\underline{\underline{D}}(k_x)| - |\underline{\underline{D}}(k_x)|'(\underline{\underline{A}}(k_x) \cdot \underline{N}_0(k_x))}{|\underline{\underline{D}}(k_x)|^2} \tag{D.10)b}$$

Substituting (D.10) into (D.9) results in (D.11):

$$\underline{F}'(k_x) = -(\underline{\underline{A}}(k_x) \cdot \underline{N}_0(k_x))^{-2}\left((\underline{\underline{A}}(k_x) \cdot \underline{N}_0(k_x))'|\underline{\underline{D}}(k_x)| - |\underline{\underline{D}}(k_x)|'(\underline{\underline{A}}(k_x) \cdot \underline{N}_0(k_x))\right) \tag{D.11}$$

Because the modes ($\underline{k}_{mode}$) for which we want to evaluate the residues are the result from the dispersion equation, it is clear that $|\underline{\underline{D}}(\underline{k}_{mode})| = 0$. So when the residue is calculated at a pole of the current spectrum, (D.11) will simplify to (D.12):

$$\underline{F}'(k_x) = (\underline{\underline{A}}(k_x) \cdot \underline{N}_0(k_x))^{-1}|\underline{\underline{D}}(k_x)|' \qquad \text{if } |\underline{\underline{D}}(k_x)| = 0 \tag{D.12}$$

It is now clear that the reciprocal of $\underline{F}'(\underline{k}_{mode})$ is identical to the residue, $\text{Res}(\underline{k}_{mode})$, we want to evaluate (D.13):

$$\underline{F}'^{-1}(\underline{k}_{mode}) = \frac{\underline{\underline{A}}(\underline{k}_{mode})}{|\underline{\underline{D}}(\underline{k}_{mode})|'} \cdot \underline{N}_0(\underline{k}_{mode}) = \underline{\mathrm{Res}}(\underline{k}_{mode}) \tag{D.13}$$

We can conclude that the current contribution due to one propagating mode $\underline{k}_{mode}$ can be calculated by:

$$\underline{c}_{mode}(x) = -j\underline{F}'^{-1}(\underline{k}_{mode})e^{-j\underline{k}_{mode}x}\hat{\boldsymbol{x}} \tag{D.14}$$

Note: For a quick MATLAB implementation, $\underline{F}'(k_x)$ can be calculated numerically:

$$\underline{F}'(\underline{k}_{mode}) = [\underline{F}(\underline{k}_{mode} + \Delta k/2) - \underline{F}(\underline{k}_{mode} - \Delta k/2)] \cdot (\Delta \underline{k})^{-1} \tag{D.15}$$

where $\Delta \underline{k} < Re(\underline{k}_{mode})/1000$

D.2 Residue in the transverse spectral plane

The integration path in k_y determines the result of dispersion equation. From the surface- and leaky-wave condition (3.26) and the associated discussion regarding the spectral planes in chapter 3, it became clear that when such wave is excited, the surface- or the leaky-wave modes should be enclosed by the integration path. This is accounted for by adding the residues of these poles to the integration over the real axis in k_y. The location of these poles in k_y can be calculated by:

$$k_{y,SFW} = \sqrt{k_{SFW}^2 - k_{mode}^2} \tag{D.16}$$

Both $\pm k_{y,SFW}$ should be enclosed by the integration path. The elements of $\underline{\underline{D}}(k_x)$ are:

$$D_{n,i}(k_x) = D_{n,i}(k_x)|_{\mathbb{R}} + D_{n,i}(k_x)|_{+k_{y,SFW}} + D_{n,i}(k_x)|_{-k_{y,SFW}} \tag{D.17}$$

with

$$\begin{aligned} D_{n,i}(k_x)|_{\mathbb{R}} &= \frac{1}{2\pi}\int_{-\infty}^{\infty} G_{xx}(k_x,k_y)C_t(k_y)e^{-jk_y(n-i)d_y}dk_y && \text{(D.18)a} \\ D_{n,i}(k_x)|_{\pm k_{y,SFW}} &= \frac{1}{2\pi}\oint_{\gamma} G_{xx}(k_x,k_y)C_t(k_y)e^{-jk_y(n-i)d_y}dk_y && \text{(D.18)b} \end{aligned}$$

where γ is a circular integration path around $\pm k_{y,SFW}$ which is clockwise for $+k_{y,SFW}$ and counterclockwise for $-k_{y,SFW}$. $D_{n,i}(k_x)|_{\pm k_{y,SFW}}$ can be solved using the residue theorem:

$$\begin{aligned} D_{n,i}(k_x)|_{\pm k_{y,SFW}} &= \frac{1}{2\pi}\oint_{\gamma} F_{n,i}(k_y)dk_y \\ &= \frac{1}{2\pi}2\pi j \,\mathrm{Res}(F_{n,i}(k_y), \pm k_{y,SFW}) \end{aligned} \tag{D.19}$$

where

$$F_{n,i}(k_y) = G_{xx}(k_x,k_y)C_t(k_y)e^{-jk_y(n-i)d_y} \tag{D.20}$$

So that:

$$\mathrm{Res}(F_{n,i}(k_y), \pm k_{y,SFW}) = \left.\frac{1}{(F_{n,i}^{-1}(k_y))'}\right|_{k_y=\pm k_{y,SFW}} \tag{D.21}$$

Appendix E

Numerical implementation and convergence

The model proposed in this contribution is implemented in a MATLAB software-tool. The model is considered **quasi**-analytical as it relies on numerical integration and derivation in the transverse domain in order to calculate the denominator in Eq. (E.1).

$$D_{n,i}(k_x) = \frac{1}{2\pi}\int_{-\infty}^{\infty} G_{xx}(k_x,k_y)C_t(k_y)e^{-jk_y(n-i)d_y}dk_y \tag{E.1}$$

Also, since the printed transmission line is to be analyzed over a specified frequency range, a suitable discrete range of frequencies has to be chosen. Finally, the poles in the denominator $\underline{\underline{D}}(k_x)$ are obtained by solving the dispersion equation by using a Taylor series expansion around an initial guess point, k_{guess}, for the propagation constant along the line (E.2).

$$\underline{k}_{mode} \approx \underline{k}_{guess} - \underline{C}^{-1}(\underline{k}_{init})([\underline{C}^{-1}(\underline{k}_{init})]')^{-1} \tag{E.2}$$

This Taylor series expansion is an approximation. The MATLAB-tool need to have some convergence checks. In this appendix, the numerical implementation is described for determining a suitable discrete frequency range, a transverse integration range leading to a converged result, and an iterative procedure for tracking the propagating modes ensuring that the tracking has converged.

E.1 Discrete frequency range

The start (f_i) and stop (f_f) frequencies determine the frequency range over which the transmission line is analyzed. The number of discrete frequency points N_f taken is a function of these frequencies and the frequency step factor k_{step}. The MATLAB-tool starts at the highest frequency and determines the next frequency as $f_{i+1} = f_i - \Delta f$ where $\Delta f = k_{step} \cdot f_i$. The number of frequency points calculated will then be:

$$N_f = \left\lceil \frac{\ln(f_i/f_f)}{\ln(1-k_{step})} \right\rceil + 1 \tag{E.3}$$

In the software-tool, the standard setting for $f_{step} = 0.04$. Increasing this number will speed up the code, however enlarging this frequency-step too much can result in difficulties in tracking the propagation mode. Also, in the case of highly dispersive transmission lines, the linear interpolation in the wavenumber plot will be misleading.

E.2 Wavenumber accuracy

The wavenumber accuracy informs about the convergence in tracking the wavenumber. The program is based on providing an initial guess for the wavenumber and by using a first order Taylor series expansion around this initial guess point it will iterate towards the true value of the wavenumber:

$$\underline{k}_{init}^{new} = \underline{k}_{init} - \underline{C}^{-1}(\underline{k}_{init})([\underline{C}^{-1}(\underline{k}_{init})]')^{-1} \tag{E.4}$$

In Eq. (E.4), $\underline{k}_{init}^{new}$ will be a new starting point for another iteration. This iteration is repeated for a maximum of n_k (default $n_k = 10$) times or when a convergence Δk (default Δk= 5e-5) is achieved:

$$\Delta k = \left|\frac{\underline{k}_{correction}}{\underline{k}_{init}}\right| \tag{E.5}$$

When the convergence in tracking the wavenumber is consistently not reached a consideration needs to be made whether to change n_k and/or Δk. It can be that the convergence goal, Δk, is impossible to achieve with a first-order Taylor expansion or that the initial guess-point is too inaccurate such that n_k iterations will not suffice.

So for every frequency point we iterate towards the true value of the wavenumber of the main propagating mode. The initial guess point is taken to be the wavenumber of the previous frequency step; for the first frequency it is taken as the average of the propagation constants of the dielectrics adjacent to the transmission lines as is described in Eq. (E.6).

$$k_{init}^{(i)} = \sqrt{\frac{k_{up}^2 + k_{down}^2}{2}} \qquad \text{for } i = 1 \qquad \text{(E.6)a}$$

$$k_{init}^{(i)} = k_{mode}^{(i-1)} \qquad \text{for } i > 1 \qquad \text{(E.6)b}$$

E.3 Integration convergence

An integration convergence check is necessary in order to ensure whether a specified convergence goal is achieved of the value for the denominator $D_{n,i}(k_x)$ in Eq. (E.1). $D_{n,i}(k_x)$ is obtained by integrating in the transverse spectral domain of the transmission line (k_y). The integration domain, from $-\infty$ and ∞ can of course not be implemented numerically. Therefore, the integration domain in k_y will be increased as long as the increased part of the integration domain adds a significant value to the total. What is called a significant value is defined by ΔInt (default ΔInt= 5e-5). The integration is also stopped when a maximum number of integration intervals is used defined by n_{int} (default $n_{int} = 300$).

The size of the integration step is determined by the integrand of the space-convolution integral $D_{n,i}(k_x)$ as it contains a Bessel- and a sinc-function and therefore zeros. In the case that the integration is unfortunately done from a zero to a zero, the convergence constrain can be met incorrectly as the oscillations due to the Bessel- and sinc-function can give a (almost) zero integrated integrand. So first the location of the zeros of the integrand is checked

$$\begin{aligned} \text{sinc}\left(\frac{k_y w_s}{2}\right) &= 0 \\ \frac{k_{y,0} w_s}{2} &= n \cdot \pi \end{aligned}$$

$$k_{y,0} = n \cdot \frac{2\pi}{w_s}$$

for $n = 1, 2, ...$ The integration step-size is chosen to be between the 10^{th} and 11^{th} zero of this sinc-function:

$$k_{y,integration-step} = 10.5 \cdot \frac{2\pi}{w_s} \tag{E.7}$$

The procedure in MATLAB is as follows. First the integrand of $D_{n,i}(k_x)$ will be integrated from $-k_{y,\text{integration-step}}$ to $+k_{y,\text{integration-step}}$ which we denote as $D_1(k_x)$:

$$D_1(k_x) = \int_{-k_{y,int-step}}^{+k_{y,int-step}} \cdots dk_y \tag{E.8}$$

After that we will calculate the following contribution of the integral:

$$D_2(k_x) = \int_{-2\cdot k_{y,int-step}}^{-k_{y,int-step}} \cdots dk_y + \int_{+k_{y,int-step}}^{+2\cdot k_{y,int-step}} \cdots dk_y \tag{E.9}$$

From these two values, the convergence can be checked by comparing the contribution of the most actual integration with the contribution of the total integration calculated so far:

$$\Delta\text{Int} = \frac{D_2(k_x)}{D_1(k_x) + D_2(k_x)} \tag{E.10}$$

When the convergence in integration is consistently not reached, a consideration can be made whether to change n_{int} and/or ΔInt. However, keep in mind that changing these settings can influence the performance of the program significantly. It can be the case that the integrand is some structure is slowly decreasing requiring an increase of n_{int}. It can also be that the ΔInt is unachievable by the numerical integration method in MATLAB (*quadgk*).

As an example, consider an arbitrary microstrip. We can see the integrand for the first and second integration step in Figure E.1 and Figure E.2 (for only the positive part of the transverse integration domain). In the case that the integration of Figure E.2 adds less then a certain threshold to the total integration, we call the integral converged.

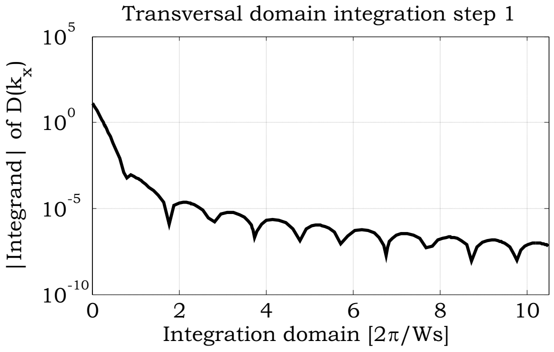

Figure E.1: First step of integration in the transverse domain

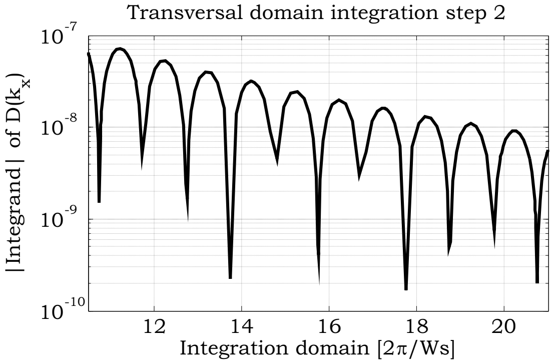

Figure E.2: Second step of integration in the transverse domain

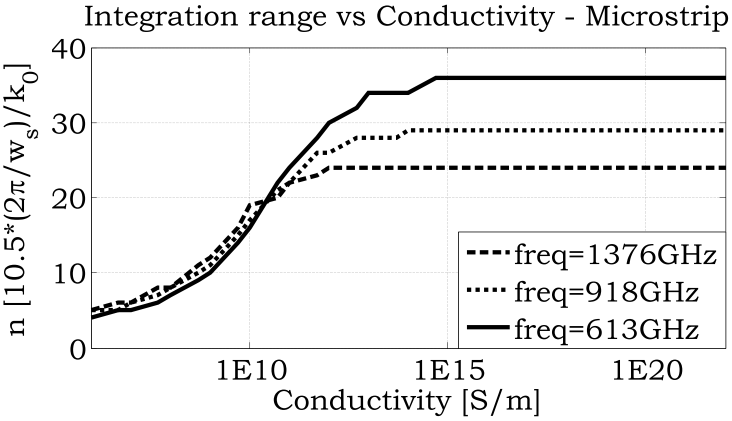

Figure E.3: Transverse integration range vs conductivity

The convergence in iteration depends not only on the dimensions of the structure, but can also significantly change when, for example, the conductors are not perfect or when the frequency changes. This example is shown in Figure E.3. The y-axis denotes the number of integration steps (Eq. (E.7)) which have to be taken before reaching the required convergence limit. An example is shown in Figure E.3. In this example we took the following convergence limits:

- $\Delta\mathrm{Int} = 1 \cdot 10^{-4}$
- $\Delta\mathrm{k} = 1 \cdot 10^{-3}$

It can be seen from Figure E.3 that, both in frequency as in conductivity, a significant change in the number of integration steps is needed before fulfilling the ΔInt integration requirement. Having an automated convergence check, as is explained in this appendix, ensures the MATLAB-tool that convergences are achieved in both wavenumber tracking as transverse integration.

Appendix F

List of abbreviations

List of abbreviations	
1D	One dimensional
2D	Two dimensional
3D	Three dimensional
CMFIE	Continuity of Magnetic Field Integral Equation
et al.	et alii (*lat.* and others)
etc.	et cetera (*lat.* and so forth)
i.e.	id est (*lat.* that is; in other words; that is to say)
EFIE	Electric Field Integral Equation
e.g.	exempli gratia (*lat.* for example; example given)
EM	Electromagnetic
FDTD	Finite-Difference Time-Domain
FEM	Finite Element Method
IE	Integral Equation(s)
PEC	Perfect Electric Conductor(s)
PPW	Parallel-Plate-Waveguide
RS	Riemann-sheet
TE	Transverse Electric
TEM	Transverse Electromagnetic
TM	Transverse Magnetic

Appendix G

Nomenclature

The Nomenclature used throughout the thesis is shown in table G.1.

Table G.1: Nomenclature used in this document.

Quantity	Notation
Scalar	a
Continuous Operator	$\mathcal{F}$
Vector in space domain	$\underline{a}$
Vector in spectral domain	$\underline{A}$
Unit vectors	$\hat{\boldsymbol{x}}, \hat{\boldsymbol{y}}, \hat{\boldsymbol{z}}$
Matrix in space domain	$\underline{\underline{a}}$
Matrix in spectral domain	$\underline{\underline{A}}$
Outer product	$\times$
Scalar or dot-product	$\cdot$
Continuous field quantities in space domain	$\underline{\boldsymbol{e}}, \underline{\boldsymbol{h}}$
Continuous field quantities in spectral domain	$\underline{\boldsymbol{E}}, \underline{\boldsymbol{H}}$
Δ-gap excitation vector	$\underline{s}_{\Delta}$
Width of a strip or slot	w_s
Physical spacing between multiple conductors	d
Phase spacing between multiple conductors	$d_y = d + w_s$
Finite conductivity of a conductor	σ
Height of a dielectric slab	H
Relative permittivity of a dielectric	ε_r
Loss tangent of a dielectric	$\tan(\delta)$
Speed of light	c
Frequency	f
Wavenumber	$k = \beta - j\alpha$
Propagation constant	β
Attenuation constant	α
Wavelength in free-space	λ_0
Wavenumber in free-space	k_0
Wavelength in a dielectric	λ_d
Wavenumber in a dielectric	k_d
Wavenumber of the main propagating mode	k_{mode}
Wavenumber of a surface-wave pole/branch-point	k_{SFW}
Wavenumber of a leaky-wave pole/branch-point	k_{LW}